

**EFFECTS OF TEMPERATURE AND DISPLACEMENT  
VELOCITY ON FRACTURE SHEAR STRENGTH  
IN TAK GRANITE**

**Pajeeraporn Weingchanda**



**A Thesis Submitted in Partial Fulfillment of the Requirements for the  
Doctor of Philosophy of Engineering in Geotechnology**

**Suranaree University of Technology**

**Academic Year 2018**

ผลกระทบของอุณหภูมิและความเร็วของการเคลื่อนตัวต่อกำลังแรงเฉือนของ  
รอยแตกในหินแกรนิตตาก



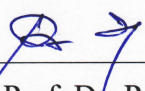
นางสาวพีรภรณ์ เวียงจันทา

วิทยานิพนธ์นี้เป็นส่วนหนึ่งของการศึกษาตามหลักสูตรปริญญาวิศวกรรมศาสตรดุษฎีบัณฑิต  
สาขาวิชาเทคโนโลยีธรณี  
มหาวิทยาลัยเทคโนโลยีสุรนารี  
ปีการศึกษา 2561

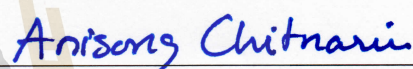
**EFFECTS OF TEMPERATURE AND DISPLACEMENT VELOCITY  
ON FRACTURE SHEAR STRENGTH IN TAK GRANITE**

Suranaree University of Technology has approved this thesis submitted in partial fulfillment of the requirements for the Degree of Doctor of Philosophy

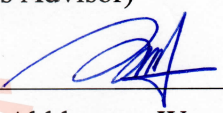
Thesis Examining Committee

  
\_\_\_\_\_  
(Assoc. Prof. Dr. Pornkasem Jongpradist)

Chairperson

  
\_\_\_\_\_  
(Asst. Prof. Dr. Anisong Chitnarin)

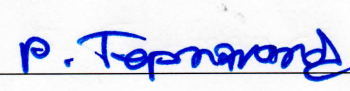
Member (Thesis Advisor)

  
\_\_\_\_\_  
(Asst. Prof. Dr. Akkhapun Wannakomol)

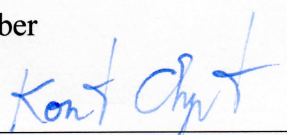
Member


  
\_\_\_\_\_  
(Asst. Prof. Dr. Decho Phueakphum)

Member

  
\_\_\_\_\_  
(Asst. Prof. Dr. Prachya Tepnarong)

Member

  
\_\_\_\_\_  
(Assoc. Prof. Ft. Lt. Dr. Kontorn Chamniprasart)

  
\_\_\_\_\_  
(Prof. Dr. Santi Maensiri)

Vice Rector for Academic Affairs  
and Internationalization

Dean of Institute of Engineering

พิธีราภรณ์ เวียงจันทน์ : ผลกระทบของอุณหภูมิและความเร็วของการเคลื่อนตัวต่อกำลัง  
แรงเฉือนของรอยแตกในหินแกรนิตดาก (EFFECTS OF TEMPERATURE AND  
DISPLACEMENT VELOCITY ON FRACTURE SHEAR STRENGTH IN TAK  
GRANITE) อาจารย์ที่ปรึกษา : ผู้ช่วยศาสตราจารย์ ดร.อานิสงส์ จิตนารินทร์, 110 หน้า.

วัตถุประสงค์ของการศึกษานี้คือเพื่อศึกษาผลกระทบของอัตราส่วนความเค้นด้านข้าง  
ความเร็วของการเคลื่อนตัวในแนวเฉือน และอุณหภูมิในหินแกรนิตดาก ความเร็วของการเคลื่อนตัว  
ในแนวเฉือนผันแปรจาก  $1.15 \times 10^{-5}$  ถึง  $1.15 \times 10^{-2}$  มิลลิเมตรต่อวินาที ที่อุณหภูมิ 303 เคลวิน และจาก  
 $1.15 \times 10^{-4}$  ถึง  $1.15 \times 10^{-2}$  มิลลิเมตรต่อวินาที ที่อุณหภูมิ 473 เคลวิน รอยแตกผิวเรียบและผิวขรุขระถูก  
ทดสอบ ผลการทดสอบแสดงว่า ความต้านทานแรงเฉือน การขยายตัว และพื้นที่การเฉือนของรอย  
แตกผิวขรุขระมีค่าลดลงเมื่ออัตราส่วนความเค้นด้านข้างเพิ่มขึ้นค่ากำลังรับแรงเฉือนสูงสุดลดลงเมื่อ  
ความเร็วของการเฉือนลดลง ผลการศึกษาการเพิ่มขึ้นของอุณหภูมิ ระบุว่าค่ากำลังรับแรงเฉือนสูงสุด  
ลดลงเมื่ออุณหภูมิเพิ่มขึ้น ค่ากำลังรับแรงเฉือนสูงสุดของรอยแตกผิวเรียบมีแนวโน้มไม่ขึ้นกับ  
อัตราส่วนความเค้นด้านข้าง ความเร็วของการเฉือน และอุณหภูมิ พลังงานความเครียดเชิงเบี่ยงเบนที่  
ใช้ในการเคลื่อนที่ของรอยแตก ภายใต้การผันแปรอัตราส่วนความเค้นด้านข้าง ความเร็วของการ  
เฉือน และอุณหภูมิเพิ่มขึ้นเชิงเส้นตรงตามค่าพลังงานความเครียดเฉลี่ย



สาขาวิชา เทคโนโลยีธรณี  
ปีการศึกษา 2561

ลายมือชื่อนักศึกษา พิธีราภรณ์ เวียงจันทน์  
ลายมือชื่ออาจารย์ที่ปรึกษา Anisong Chitnarin



PAJEERAPORN WEINGCHANDA : EFFECTS OF TEMPERATURE  
AND DISPLACEMENT VELOCITY ON FRACTURE SHEAR  
STRENGTH IN TAK GRANITE. THESIS ADVISOR : ASST. PROF.  
ANISONG CHITNARIN, Ph.D., 110 PP.

DILATION/TRIAXIAL SHEAR TEST/SHEARING RATES/ORTHOTROPIC  
STRESS

The objective of this study is to experimentally laboratory determined effects of lateral stress ratios, displacement velocity and temperature in Tak granite. The shear displacement velocities were varied from  $1.15 \times 10^{-5}$  to  $1.15 \times 10^{-2}$  mm/s at 303 kelvin and  $1.15 \times 10^{-4}$  to  $1.15 \times 10^{-2}$  mm/s at 473 kelvin. Smooth and rough fractures were tested. The results show that shearing resistance, dilation and areas of sheared-off asperities of rough fractures decreased when the lateral stress ratios increased. The peak shear strengths decreased with decreasing shear velocities. Results of elevated temperature testing indicated that the peak shear strengths decreased with increasing temperatures. The shear strengths of smooth surfaces tend to be independent of the lateral stress ratios, displacement velocity and temperature. The distortional strain energy ( $W_d$ ) required to displace the fractures under various lateral stress ratios, displacement velocity and temperatures increases linearly with mean strain energy ( $W_m$ ).

School of Geotechnology

Academic Year 2018

Student's Signature Pajeeraporn W.

Advisor's Signature Anisong Chitnarin

## ACKNOWLEDGMENTS

I wish to acknowledge the funding supported by Suranaree University of Technology (SUT).

I would like to express my sincere gratitude thanks to Asst. Prof. Dr. Anisong Chitnarin for his valuable guidance and efficient supervision. I appreciate for his strong support, encouragement, suggestions and comments during the research period. My heartiness thanks to Prof. Dr. Kittitep Fuenkajorn, Asst.Prof. Dr. Decho Phueakphum, Assoc. Prof. Pornkasem Jongpradist, Asst. Prof. Dr. Prachya Tepnarong and Asst. Prof. Dr. Akkhapun Wannakomol for their constructive advice, valuable suggestions and comments on my research works as thesis committee members. Grateful thanks are given to all staffs of Geomechanics Research Unit, Institute of Engineering who supported my work.

Finally, I would like to thank beloved parents for their love, moral support and constant encouragement.

Pajeeraporn Weingchanda

# TABLE OF CONTENTS

	<b>Page</b>
ABSTRACT (THAI).....	I
ABSTRACT (ENGLISH).....	II
ACKNOWLEDGEMENTS.....	III
TABLE OF CONTENTS.....	IV
LIST OF TABLES.....	VIII
LIST OF FIGURES.....	X
SYMBOLS AND ABBREVIATIONS.....	XIV
<b>CHAPTER</b>	
<b>I INTRODUCTION.....</b>	<b>1</b>
1.1 Background of problems and significance of the study.....	1
1.2 Research objectives.....	3
1.3 Research methodology.....	3
1.3.1 Literature review.....	3
1.3.2 Sample Preparation.....	4
1.3.3 Laboratory Testing.....	5
1.3.4 Development of mathematical relations.....	6
1.3.5 Discussions, Conclusions and thesis writing.....	6
1.4 Scopes and limitations.....	8

## TABLE OF CONTENTS (Continued)

	Page
1.5 Thesis contents .....	8
<b>II LITERATURE REVIEW</b> .....	<b>10</b>
2.1 Introduction .....	10
2.2 Factors affecting to joint shear strength .....	10
2.2.1 Effect of shearing rate on fracture shear strength .....	10
2.2.2 Effect of temperature on fracture shear strength .....	13
2.2.3 Roughness .....	18
2.2.4 Effect of $\sigma_2$ .....	19
2.2.5 Effect of cyclic loading .....	21
2.2.6 Effect of pore pressure .....	23
2.3 Activation energy .....	26
2.4 Tak Batholith .....	31
<b>III SAMPLE PREPARATION</b> .....	<b>34</b>
3.1 Introduction .....	34
3.2 Sample preparation .....	36
<b>IV LABORATORY TESTING</b> .....	<b>49</b>
4.1 Introduction .....	49
4.2 Triaxial shear test on tension-induced fractures and smooth saw-cut surface .....	49
4.3 Test procedure .....	52

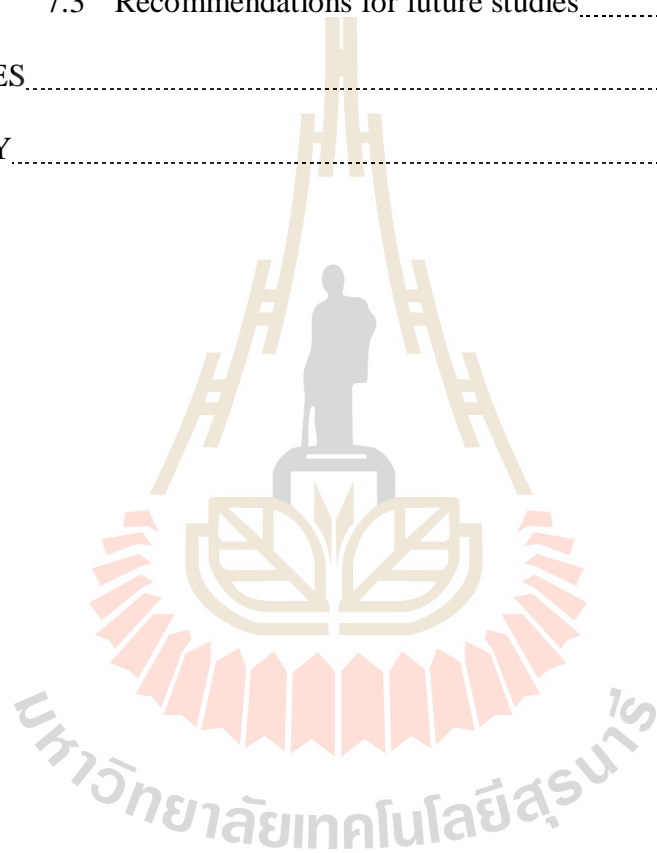
## TABLE OF CONTENTS (Continued)

	Page
<b>V TESTING RESULTS</b> .....	57
5.1 Tension-induced fractures under different $\sigma_p/\sigma_o$ ratios.....	57
5.1.1 Shear strength.....	57
5.1.2 Dilations.....	62
5.2 Shear strength of tension-induced fractures under various displacement velocities.....	66
5.2.1 Shear strength.....	66
5.2.2 Dilations.....	73
5.3 Triaxial shear tests on smooth saw-cut surfaces.....	79
<b>VI SHEAR STRENGTH CRITERIA</b> .....	82
6.1 Introduction.....	82
6.2 Empirical criterion under different $\sigma_p/\sigma_o$ ratios.....	82
6.3 Strain energy density criterion under lateral stress ratios.....	84
6.4 Criterion for tension-induced fractures under various displacement velocities.....	88
6.5 Strain energy density criterion under various displacement velocities.....	90
<b>VII DISCUSSIONS, CONCLUSIONS AND RECOMMENDATIONS FOR FUTURE STUDIES</b> .....	94
7.1 Discussions.....	94



**TABLE OF CONTENTS (Continued)**

	<b>Page</b>
7.2 Conclusions.....	97
7.3 Recommendations for future studies.....	98
REFERENCES.....	100
BIOGRAPHY.....	110



# **CHAPTER II**

## **LITERATURE REVIEW**

### **2.1 Introduction**

This chapter gives the results of literature review carried out to improve an understanding of joint shear strength, true triaxial or polyaxial stress, earthquake and new equations development. The topics reviewed here include factors affecting to joint shear strength, activation energy and earthquake.

### **2.2 Factors affecting to joint shear strength**

Some factors influencing the joint shear strength of granite rock were summarized in this section, including shearing rate, temperature, roughness, confinements, cyclic loading and pore pressure.

#### **2.2.1 Effect of shearing rate on fracture shear strength**

Different displacement velocities may impose different behavior to the shearing resistance of rock fractures. Crawford and Carrant (1981) state that the frictional resistance of rock joints depends on the rate of shear displacement. For hard rocks, the resistance decreases with increasing shear displacement rates were greater than a variable critical velocity. For soft rocks, the resistance increased with increasing shear velocity, up to a critical shear displacement rate, and there after remained essentially constant (Muralha et al., 2013). Laboratory test results by Curran and Leong (1983) suggested that the fracture shear strengths were sensitive to

a certain range of shear velocities. Above and below this range the fracture shear strengths were independent of the shear velocity. Li et al. (2012a, b) performed cyclic shear tests (with shear velocities ranging from 0.5 to 50 mm/min) on artificial rock fractures and concluded that the residual shear strength increased with displacement velocity. The effect of the shear velocity on the peak stress remains inconclusive due to the complex variability of the asperities.

Kleepmek and Fuenkajorn (2015) studied the rate-dependent shear strength of rock fractures by performing triaxial shear testing under various shear velocities and confinements. A polyaxial load frame was used to perform the shear tests on tension-induced fractures prepared in  $50 \times 50 \times 87$  mm<sup>3</sup> rectangular blocks. The fracture area was  $50 \times 100$  mm<sup>2</sup>. The specimens were prepared from granite, marl and sandstone. The confining pressures were varied from 1, 3, 7, and 12 to 18 MPa. The axial stresses were applied under constant rates equivalent to the shear velocities on the fractures from  $8.7 \times 10^{-6}$  to  $8.7 \times 10^{-3}$  mm/s. The asperity amplitudes on the fracture planes were measured from laser-scanned profiles along the shear direction and used to estimate the joint roughness coefficients (JRC) of the fracture. The JRC's were average 15, 8 and 6 for the granite, marl and sandstone respectively. The test results indicated that the peak shear strengths under each confinement increased with shear velocities. The Barton's criterion was modified to explicitly incorporate the shear velocity and confining pressure. The peak shear strength ( $\tau$ ) was presented as:

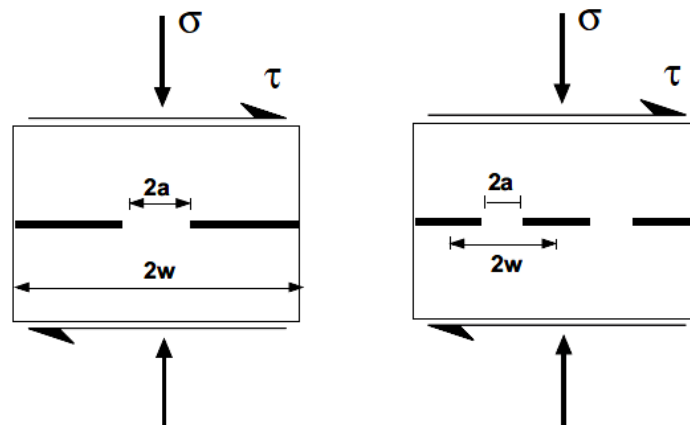
$$\tau = \sigma_n \cdot \tan \{ \phi_b + \text{JRC} \cdot \log [ \kappa \cdot (\dot{d}_s)^\lambda \cdot \exp ( \beta \cdot \sigma_3 ) / \sigma_n ] \} \quad (2.1)$$

where  $\sigma_n$  = normal stress,  $\phi_b^*$  = basic friction angle or apparent friction angle of saw cut surface,  $\kappa$ ,  $\lambda$ , and  $\beta$  were empirical constants,  $\dot{d}_s$  = shear velocity, and  $\sigma_3$  =

confining pressure. The equation fits well to their experimental results for all rock types. It allows a transition to the conventional direct shear test results by setting  $\sigma_3$  equal to zero. The equation can be used to predict rock fracture shear strengths under confining pressures and shear velocities beyond those used in their study.

Kemeny (2003) proposed a fracture mechanic model was developed to illustrate the importance of time-dependence for brittle fractured rock. In particular a model was developed for the time dependent degradation of rock joint cohesion. Degradation of joint cohesion was modeled as the time-dependent breaking of intact patches or rock bridges along the joint surface. A fracture mechanics model was developed utilizing subcritical crack growth, which results in a closed-form solution for joint cohesion as a function of time. A simple fracture mechanics model for the rock bridge was shown in Figure 2.1.

In this paper a model was developed for the time-dependent degradation of rock joint cohesion. Degradation of joint cohesion was modeled as the time-dependent breaking of intact patches or rock bridges along the joint surface. A fracture mechanics model was developed utilizing subcritical crack growth, which results in a closed-form solution for joint cohesion as a function of time. As an example, a rock block subjected to plane sliding was analyzed. The cohesion was found to continually decrease, at first slowly and then more rapidly. At a particular value of time the cohesion reduced to value that resulted in slope instability.



**Figure 2.1** Fracture mechanics models, a) single rock bridge under far field normal and shear stresses, b) multiple rock bridges under far field normal and shear stresses (Kemeny, 2003).

A second example was given where a variation in some of the material parameters was assumed. A probabilistic slope analysis was conducted, and the probability of failure as a function of time was predicted. The probability of failure was found to increase with time, from an initial value of 5% to a value at 100 years of over 40%. These examples show the importance of being able to predict the time-dependent behavior of a rock mass containing discontinuities, even for relatively short-term rock structures. In the future some actual field case studies using the model will be conducted, to evaluate the usefulness of the simple model for actual engineering design.

### 2.2.2 Effect of temperature on fracture shear strength

Temperature is one of the main factors influencing the mechanical behavior of rock (Stesky, 1975; Dwivedi et al. 2008). Several researchers (Blanpied et al., 1995; Ohnaka, 1995; Odedra et al., 2001; Shimada and Liu, 2000) studied the



effects of temperature on the rock physical and mechanical properties. The results indicated that temperature influences the friction angle, cohesion and shear strength of rocks. Based upon microscopic observation, Xu et al. (2009) and Shao et al. (2015) studied the effect of temperature on mechanical characteristics and behaviors of granite was analyzed by using experiments as scanning electron microscope (SEM), X-ray diffraction and acoustic emission (AE) and the micromechanism of brittle-plastic transition of granite under high temperature. The AE results showed that the increasing temperature reduces the stress thresholds for crack initiation and crack damage and extends the duration of stable crack propagation. The stress–strain and AE results reveal that the failure modes of Strathbogie granite specimens changed from brittle fracturing to quasi-brittle shear fracturing and eventually to ductile failure with increasing temperature. For soft rock, the increase of temperature, there was a diminution of Young's modulus, an increase of Poisson's ratio and a decrease of compression strength through the diminution of frictional coefficient. (Masri et al. 2014; LianYing et al. 2009).

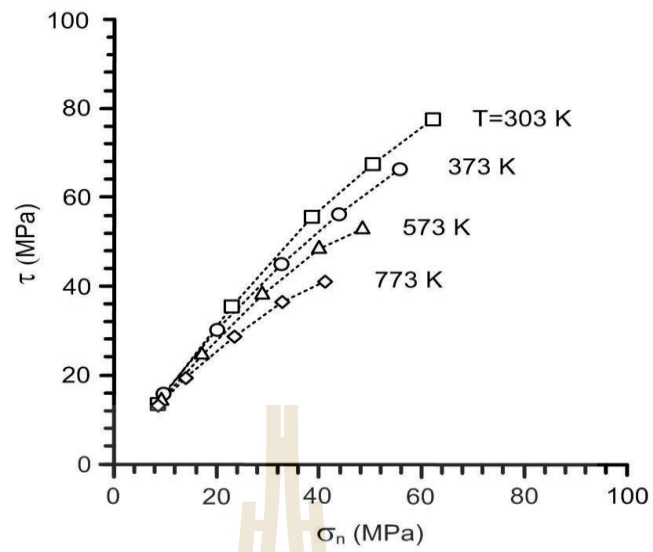
Fuenkajorn and Naphudsa (2014) showed the effect of the shear strength of fractures in Tak granite under the defined temperatures. Triaxial shear tests were performed using a polyaxial load frame conducted in 2 types of experiments: the effects of temperature on the peak shear strengths of tension-induced fractures and smooth surfaces. The testing temperatures ranged from 303, 373, 573 to 773 kelvin with confining stresses varied from 1, 3, 7, 12 to 18 MPa. The results clearly showed the thermal effect on the friction resistance of granite fractures. For rough fracture surfaces, the higher the temperatures can lower the shear strength (Figure 2.2). The reductions of the friction angle and cohesion with the increasing temperature were

observed. The proposed Barton's equation can be used to predict the friction resistances of the fractures under the temperatures within the range tested. The shear strength of smooth surface tends to increase with temperature particularly above 373 Kelvin (Figure 2.3). This may be due to stick-slip phenomenon.

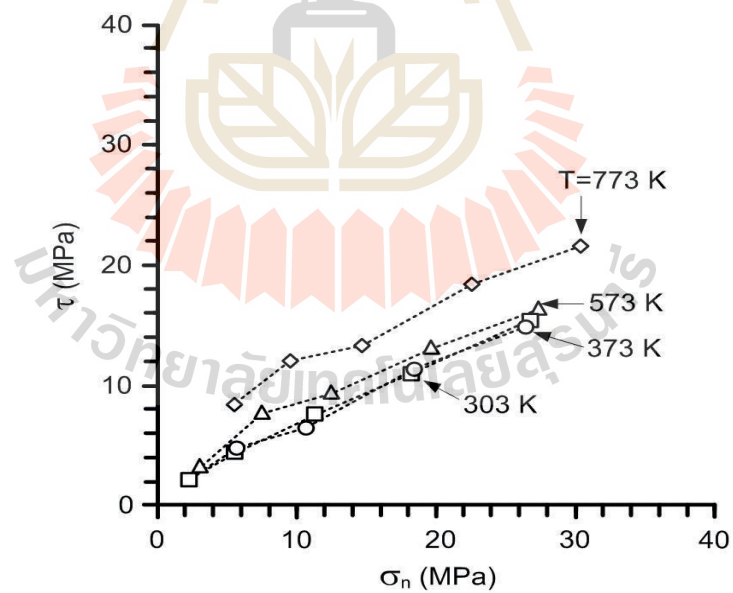
The shear strength decreased with increasing temperature, which can be best described by an empirical equation:

$$\tau = \alpha \cdot \sigma_n^{\beta} \cdot \exp(-\lambda/T) \quad (2.2)$$

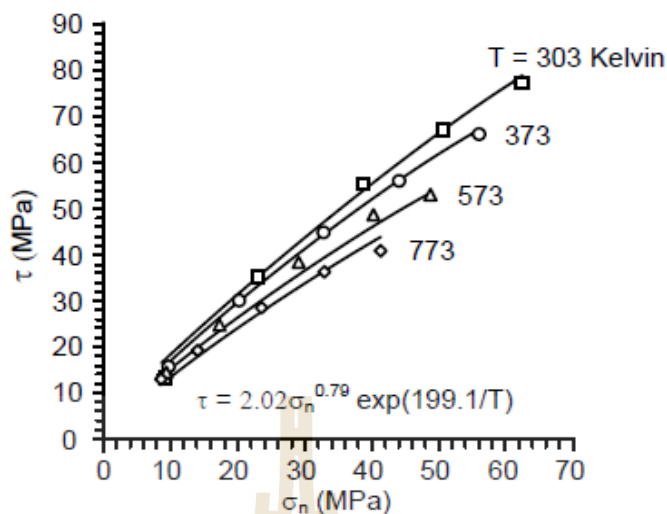
where  $\alpha$ ,  $\beta$ ,  $\lambda$  were empirical constants. Regression analysis on the test data using SPSS statistical software (Wendai, 2000) these parameters were defined as:  $\alpha = 2.02$ ,  $\beta = 0.79$ , and  $\lambda = -199.1$ . Figure 2.4 compares the test data with the curves fit of the proposed equation. This equation can be used to predict shear strength of fractures granite under elevated temperatures.



**Figure 2.2** Shear stresses as a function of normal stresses of tension-induced fractures (Fuenkajorn and Naphudsa, 2014).



**Figure 2.3** Shear stresses as a function of normal stresses of saw-cut surfaces (Fuenkajorn and Naphudsa, 2014).



**Figure 2.4** Comparison between test results (point) and curves fit (lines) (Fuenkajorn and Naphudsua, 2014).

Kawamoto and Shimamoto (1998) studied shearing experiments on mixed halite-calcite layers to understand the behavior of bimineralic fault zones, using a high-temperature biaxial testing machine at rate of  $0.3 \mu\text{m/s}$  and shear strains to about 30. Temperature was increased to  $700^\circ\text{C}$  in linear proportion to normal stress, with the experimental geotherm of about  $22^\circ\text{C/MPa}$ . The experimental data clearly demonstrate that the effect of mineral composition on the frictional strength at the temperature of  $600^\circ\text{C}$  and normal stress of about 24-27 MPa. The behavior of pure halite shear zones was fully plastic under these conditions that shear resistance was nearly independent of normal stress. No strength peak is observed in the 75% halite experiment. The 2% halite specimen displays stick-slip soon after the peak friction was exceeded, the specimens containing more than 5% halite show only stable slip throughout the experiments.

### 2.2.3 Roughness

Joint roughness has an essential influence on the shear behavior of rock joints. In engineering practice, the shear strength criterion proposed by Barton (1973) for rock joints is widely adopted. In which, the JRC (joint roughness coefficient) value for a given joint profile can be estimated visibly by comparing it with the ten JRC profiles whose JRC ranges were from 0 to 20. This set of profiles has subsequently been adopted as a standard by the ISRM. Zhao (1997a, 1997b) and Johansson and Stille, (2014) stated that the JRC-JCS model criterion by Barton tends to over-predict the shear strength for those natural joints with less matched surfaces. The new JRC-JMC model provides appropriate fining of the shear test results and gives a better interpretation and prediction, particularly for natural joints that do not have perfectly matched surfaces. Grasselli and Egger (2003) proposed a new constitutive criterion, relating stress and displacements, was proposed to model the shear resistance of joints under constant normal load conditions. The proposed criterion was also used to estimate the joint roughness coefficient (JRC) value. The predicting values were successfully correlated with JRC values obtained by back analysis of shear tests.

Barton and Choubey (1977) proposed empirical non-linear equation for peak shear strength of rough unfilled joints based on the results of direct shear tests performed on a wide variety of model tension fractures. The proposed equation for peak shear strength was as follows, which is sensitive both to variable joint roughness and compressive strength for the rock or joint walls:

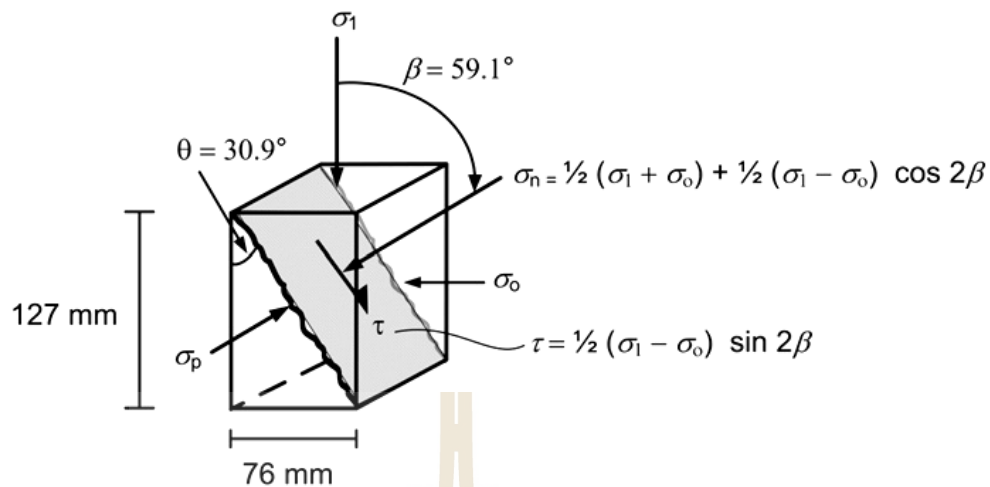
$$\tau = \sigma_n \tan [JRC \log_{10} (JRC / \sigma_n) + \phi_b] \quad (2.3)$$



where  $\tau$  is shear strength at failure,  $\sigma_n$  is stress normal to the shear plane,  $\phi_b$  is the basic friction angle on smooth planar sliding surface, JRC is the joint roughness coefficient and JCS is the joint wall compressive strength.

#### 2.2.4 Effect of $\sigma_2$

Kapang et al. (2013) performed the true triaxial shear tests to determine the peak shear strengths of tension-induced fractures in three Thai sandstones. The specimens used for the true triaxial shear tests were prepared from the Phu Kradung, Phu Phan and Phra Wihan sandstones (here after designated as PKSS, PPSS and PWSS). They were cut to obtain rectangular blocks with nominal dimensions of 76 x 76 x 126 mm<sup>3</sup>. The normal to the fracture plane makes an angle of 59.1° with the axial (major principal) stress. Dead weights were placed on the two lower bars to obtain the pre-defined magnitude of the lateral stresses ( $\sigma_o$  and  $\sigma_p$ ) on the specimen. Simultaneously the axial (vertical) stress was increased to the same value with  $\sigma_o$  to obtain the condition where both shear and normal stresses were zero on the fracture plane. This was set as an initial stress condition. The test was started by increasing the axial stress at a constant rate using the electric oil pump while  $\sigma_p$  and  $\sigma_o$  were maintained constant. The specimen deformations in the three loading directions were monitored. The readings were recorded every 10 kN of the axial load increment until the peak shear stress was reached. Figure 2.5 shows the directions of the applied stresses with respect to the fracture orientation.



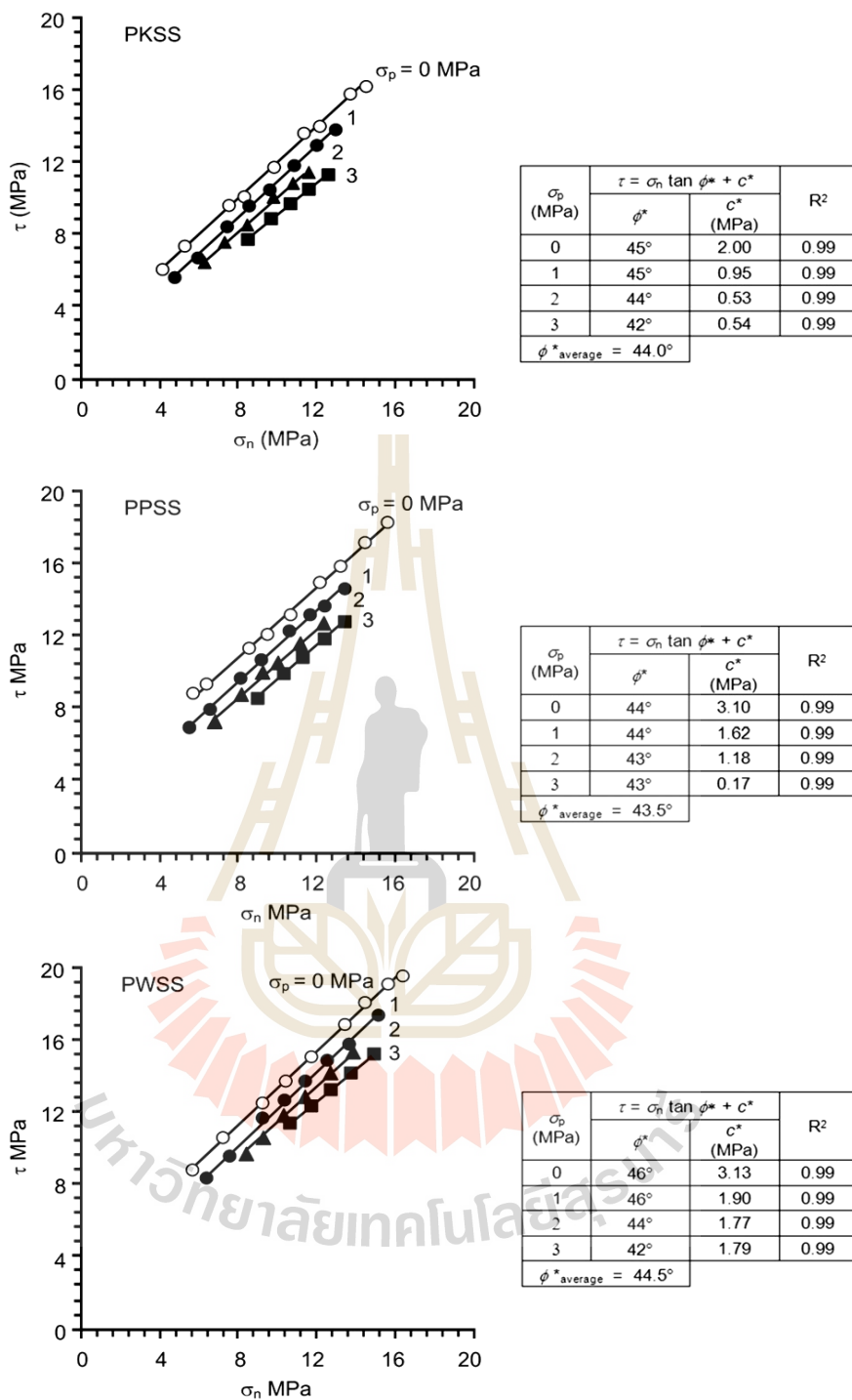
**Figure 2.5** Shear ( $\tau$ ) and normal ( $\sigma_n$ ) stresses calculated from the applied axial stress ( $\sigma_1$ ) and lateral stress on the fracture plane ( $\sigma_0$ ) (Kapang et al., 2013).

Four test series were performed: (1) true triaxial shear tests of tension-induced fractures under constant  $\sigma_p/\sigma_0$  ratio, (2) true triaxial shear tests of tension-induced fractures under constant  $\sigma_p$ , (3) true triaxial shear tests of smooth surfaces under constant  $\sigma_p$ , and (4) direct shear tests of tension-induced fractures. The peak shear strengths were determined for lateral stress ratios ( $\sigma_p/\sigma_0$ ) of 0, 0.5, 1, 2, 3 and 4. The conditions where  $\sigma_p/\sigma_0$  was 0 and 1 were equivalent to the direct shear testing and the triaxial shear testing, respectively. The configurations of the sandstone specimens and test procedure for this test series were identical to those mentioned above. Here  $\sigma_p$  was maintained constant at 1, 2 or 3 MPa while  $\sigma_0$  was varied from 1.5 to 6 MPa. The results were presented in the forms of  $\tau$ - $\sigma_n$  diagrams in Figure 2.6. For a comparison the true triaxial testing results at  $\sigma_p = 0$  were also incorporated into the figure. It was found that the lateral stress  $\sigma_p$  can notably decreased the fracture shear strengths. From

the results of their study it can be concluded that the lateral stress ( $\sigma_p$ ) parallel to the sliding plane and perpendicular to the sliding direction can significantly reduce the cohesion and friction angle of the fractures. The greater magnitudes of the lateral stress  $\sigma_p$  result in larger sheared off areas and larger dilations. In general the decreased of the fracture cohesion with increasing confining pressures (for the case of lateral stress ratio  $\sigma_p/\sigma_o = 1$ ) as observed agreed reasonably well with the experimental results obtained by Ramamurthy and Arora (1994). This means that the fracture shear strengths from the (unconfined) direct shear testing may not truly represent the fault or fracture shear strengths under the multi-axial stresses of in-situ conditions.

### **2.2.5 Effect of cyclic loading**

Kamonphet and Fuenkajorn (2013) studied the direct shear tests have been performed to determine the peak and residual shear strengths of fractures in sandstone, granite and limestone under cyclic shear loading. The fractures were artificially made in the laboratory by tension inducing and saw-cut methods. Results indicated that the cyclic shear load can significantly reduce the fracture shear strengths and stiffness. The peak shear strengths rapidly decreased after the first cycle and tend to remain unchanged close to the residual strengths through the tenth cycle. Degradation of the first order asperities largely occurs after the first cycle. The fracture dilation rates gradually decreased from the first through the tenth cycles suggesting that the second order asperities continuously degrade after the first load cycle. The residual shear strengths were lower than the peak shear strengths and higher than those of the smooth fractures. The strength of smooth fracture tends to be independent of cyclic shear loading.



**Figure 2.6** Peak shear strength ( $\tau$ ) as a function of normal stress ( $\sigma_n$ ) for various  $\sigma_p$  (Kapang et al., 2013).

Rajaram (1981) proposed a better understanding of soil/rock-structure interaction was invaluable in the seismic design of concrete and masonry structures. In an effort to understand the behavior of rock under cyclic compression, both intact and faulted specimens of Westerly granite (2.5 cm. dia. x 6.25 cm. long) were subjected to uniaxial and triaxial loading at a uniform rate of one cycle per second. The fatigue strength under uniaxial loading at 106 cycles was found to be about 70% of the static compressive strength, and confining pressure improved fatigue resistance considerably. The accumulated permanent strain at the maximum stress level was found to be independent of the stress path and bounded by the complete stress-strain curve. Cyclic loading produced dilatancy and the stress at the onset of dilatancy was significantly reduced by repeated cycling. In faulted specimens (sawcut at 30 degrees to the longitudinal axis), the first loading cycle produced a large amount of sliding; subsequent cycles resulted in a decelerating rate of increase in the amount of sliding, with a steady-state equilibrium being reached in a few cycles. Cyclic loading increased crack porosity, and progressive microcracking causes fatigue failure.

### **2.2.6 Effect of pore pressure**

Berumen (1996) proposed a new approach for interpreting the effect of pore pressure on the conductivity and permeability of artificially fractured rocks. The mathematical model formulated includes the non-linear effect of pressure dependence of fracture conductivity and formation permeability through a modified concept of fracture conductivity. New type curves for pressure-sensitive fracture formation systems were generated and a method of pressure analysis to interpret this effect was provided. The pressure behavior of wells intercepting pressure-sensitive finite



conductivity fractures was investigated by solving numerically the non-linear mathematical model. A conductivity modulus in the fracture ( $fD$ ) and a permeability modulus in the formation ( $D$ ) determine the intensity of the pore pressure effect. Results of our investigation demonstrate that when the fracture conductivity was pressure dependent, the use of conventional techniques to evaluate fractured wells may lead to incorrect estimates of the fracture-formation properties. The slope of the pseudo-bilinear flow period becomes function of  $CfD$  and  $fD$ , ranging from 0.25 to 0.35. The interpretation of pressure data was carried out through a graph of  $p$  vs  $t$ . However the pore pressure effect has no influence on the one-half slope of the linear flow. A novel correlation to detect the approximate time and pressure when the fracture closure occurs was presented. Equations relating the pseudo-bilinear slope with  $CfD$  and  $fD$  were obtained by using multivariate non-linear regression analysis. The expressions facilitate the analysis of well-test data and detect the pore pressure effect on conductivity.

Hou et al. (2017) investigated the effect of pore pressure distribution on fracture behavior of rock in gas fracturing, nitrogen fracturing experiments on the sandstone were performed under different gas filtration conditions. Results indicated that the breakdown pressure of the sandstone reduce with the decreasing amount of gas filtration. In no gas filtration case, the breakdown pressure value of the sample decreases by 69.98 and 45.6% in comparison to no gas invasion case and gas filtration case, respectively. The failure pattern of the sandstone sample was determined by borehole pressure and pore pressure, and it was mainly controlled by borehole pressure at high injection rate and controlled by pore pressure at low injection rate. In addition, pore pressure can promote microcracks initiation and high pore pressure

distribution contributes to generating complex multifractures network. Furthermore, in order to popularize the experimental results to the field application, a method of special graded particles was proposed to temporarily plug induced and natural fractures during fracturing processed and then prop these fractures after fracturing. The method was expected to improve fracturing efficiency and increase production of oil and gas in practical application.

Li et al. (2015) studied that the fluid flow driven by pore pressure gradient can influence the fracturing behaviour. To better capture the complex hydraulic fractures in rock materials, a ‘pinch-off’ breaking test was numerically conducted to illustrate the tensile failure of a rock specimen within a uniform pore pressure field. A double-notched specimen, with water pressure in one notch while keeping another one open to the atmosphere, was numerically extended to investigate how the water flow direction or the pore pressure gradient will influence the fracturing behaviour. The simulation results indicated that both pore pressure magnitude and the orientation and distribution of pore pressure gradient surrounding the fracture tip can affect fracturing process and macroscopic strength behaviour of rock materials.

AlTammar et al. (2018) proposed the hydraulic fracture initiation and propagation in the presence of multiple fluid injection sources and under far-field stresses were investigated experimentally utilizing a novel fracturing cell. Mixtures of plaster and clay were used to cast sheetlike, porous test specimens with injection holes in different configurations. The specimen was placed between two transparent plates that allow us to take videos of the speckled rock sample surfaces to facilitate digital image processing of rock displacement. Far-field differential stress was applied to the specimen via pneumatic jacks. Hydraulic fracture growth during the experiment was

recorded using a high resolution digital camera. Key frames were subsequently analyzed using Digital Image Correlation (DIC) to reveal micro-cracks, strains and other features that were difficult to detect with the naked eye. Experiments were conducted to examine fracture growth in proximity to a constant pressure injection source as well as propagation of multiple neighboring fractures in porous media. It was clearly shown that high pressure injection regions alter stress field appreciably. Consequently, a fracture propagating along the maximum far-field stress tends to turn towards a high pore pressure source. In addition, a secondary fracture can be induced when the magnitude of the pore pressure source was relatively large. Fracture turning and formation of secondary fractures due to the adjacent high pressure injection hole maybe suppressed under relatively high far-field differential stress. It was also observed that fractures tend to grow perpendicular to the maximum far-field stress direction for multiple, closely spaced injection holes. In the case of isotropic far-field stress state, fractures tend to initiate and propagate towards neighboring injection holes. Fracturing pressure was generally observed to be markedly lower for tests with multiple fluid injection sources compared to tests with a single injection hole. Our experimental work confirms and extends previous literature in the topic via direct monitoring of fracture growth and novel application of digital image processing.

### **2.3 Activation energy**

Stesky (1978) studied the mechanical properties of faulted and jointed rock under pressure and temperature and in the presence of water. At low effective confining pressures (below about 1 kilobar), the friction strength was quite variable and depends on the frictional resistance between gouge particles or asperities and on

the dilatancy of the fault. At higher pressures the friction strength was nearly independent of mineralogy, temperature, and rate, at least for rocks whose friction strength was less than the failure strength. Water tends to slightly weaken the fault. The type of sliding motion, whether stick-slip or stable sliding, was much more affected by environmental and mineralogical factors. In general, stick-slip was dominant at high pressures and low temperatures, in the presence of strong minerals such as quartz and feldspar, in the absence of gouge, for lower surface roughness, and perhaps in the presence of water. The microscopic deformation mechanisms were poorly understood. At low temperatures, cataclasis dominates in rocks containing mostly quartz or feldspar, and plastic deformation in rocks containing mostly calcite or platy silicates. At high temperature most minerals deform plastically, producing a greater temperature- and rate-dependence of the friction strength. Glass has been found in some sliding surfaces in sandstone.

By combining measurements of the rate- and temperature-dependence of friction strength, as well as the activation energy, the following “flow law” for frictional sliding was found:

$$\delta = \delta_0 \cdot \exp(\tau/\tau_0) \exp(-Q/RT) \quad (2.4)$$

where  $\delta$  was the sliding velocity,  $\tau$  was the friction strength,  $Q$  was the activation energy,  $R$  was the gas constant,  $T$  was the absolute temperature, and  $\delta_0$  and  $\tau_0$  were empirical constants. These measurements were made at a constant confining pressure of 2.5 kbars, so the role of normal stress was not included in equation (2.4). A few experiments made at 4 kbars pressure suggest that  $\tau_0$  was unchanged from the lower

pressure value at 450°C but at 700°C it was a factor of three higher. The effect of pressure on  $Q$  was not known.

Mostafa et al. (2003) studied the temperature dependence of the electrical resistivity of basalt and granite samples. The electrical resistivities of these samples were measured in the temperature range from RT to 1000 K. There was observed that, the electrical resistivity of all investigated samples was decreased with the increase of temperature. The results showed that, the behaviour of the electrical resistivity have two conduction regions for basalt and granite samples. In the first region (RT to 400 K) for basalt and (RT – 450 K) for granite samples, the electrical resistivity exhibits a slight decrease. In the second region (400 to 1000 K) for basalt and (450 to 1000 K) for granite samples, the electrical resistivity exhibit a rapid decrease with the increase of temperature. The average activation energies of investigated basalt and granite samples were calculated and discussed (Table 2.1).

This was observed in the field of correlation of resistivity with heat flow. It was well documented in the laboratory that the equation:

$$\rho = \rho_0 \exp (E/k_B T) \quad (2.5)$$

applies to nearly all minerals. Where  $\rho$  was electrical resistivity (usually expressed in ohm.cm),  $\rho_0$  was pre-exponential factor,  $k_B$  was the Boltzmann constant,  $T$  absolute temperature and  $E$  the activation energy in eV.

**Table 2.1** The activation energies of the investigated samples. ( $E_1$  and  $E_2$  were the activation energies for the first and second regions, respectively).

Sample	$E_1$ (eV)	$E_2$ (eV)	$\langle E_1 \rangle$ (eV)	$\langle E_2 \rangle$ (eV)
B1	0.273	0.834	{0.152}	{0.930}
B2	0.093	0.706		
B3	0.107	1.203		
B4	0.137	0.979		
G1	0.152	0.837	{0.140}	{0.761}
G2	0.148	1.120		
G3	0.126	0.473		
G4	0.134	0.616		

Alvarez et al. (1978) proposed the conductivity of four igneous rocks with, 49, 65, 77, and 84%  $\text{SiO}_2$  was measured as a function of temperature in the interval from 20° to 1280°C; measurements were made in a vacuum of  $10^{-3}$  torr. No simple relationships were found between conductivity and  $\text{SiO}_2$  content or versus major element groupings such as  $\text{Na}_2\text{O}=\text{K}_2\text{O}=\text{CaO}$  and  $\text{TiO}_2=\text{Cr}_2\text{O}_3=\text{Al}_2\text{O}_3=\text{Fe}_2\text{O}_3=\text{FeO}$ . An analytical expression was obtained between conductivity and the albite-quartz ratio, valid for temperatures between 300° and 1200°C. It was necessary to compute the CIPW norm in order to obtain the albite and quartz percentages. The onset of melting apparently occurred between 600° and 700°C. Petrography performed on two samples after cooling showed 70 and 85% partial melting. Three conduction regions were identified: 1) below 300°C, 2) between 300°C and 600°C, and 3) above 600°C. Different activation energies obtained for the heating and cooling intervals confirmed

that the sample undergoes textural changes in the heating-cooling cycle. Activation energy increments of 0.1 and 0.2 eV per decade of albite-quartz ratio were obtained.

Nordeng (2012) performed six samples of shale from the Bakken (Miss.-Dev.) Formation were analyzed using LECO TOC, Rock Eval 6 and multiple heating rate pyrolysis. The results indicated that within a single well penetrating thermally immature source rock, the frequency factor and activation energy vary in a log-linear fashion. Another sample from a similarly immature core produced almost identical kinetic parameters. The only sample that did not cluster along the linear trend was taken from a well situated within the most thermally mature portion of the basin. These results suggest that subtle variations in kerogen composition were responsible for the observed covariance in the activation energy and natural logarithm of the frequency factor.

In his solution, shows that the temperature that corresponds with the maximum reaction rate ( $T_p$ ) shifts with the heating rate ( $\beta$ ) in accordance with the activation energy ( $E_a$ ) and frequency factor ( $A$ ) as follows:

$$\ln(\beta/T_p^2) = \ln(AR/E_a) - E_a/RT_p \quad (2.6)$$

where  $E_a$  = Activation Energy (kJ/mole)

$R$  = Gas Constant (.008314) kJ/mol-°K

$A$  = Frequency factor ( min)

$T_p$  = Temperature that causes maximum reaction rates (°K)

$\beta$  = Heating Rate (° K/min)



These results also suggest that changes in the kinetic parameters caused by thermal maturation result in higher activation energies and smaller frequency factors that were conspicuously different than the kinetic parameters obtained from the less mature sample set.

## **2.4 Tak Batholith**

The Tak Batholith is located in Tak province and nearby areas in northern Thailand. The exposures of granitic rocks cover an area of more than 4,000 square kilometer (Pongsapich and Mahawat, 1977). The Mae Ping (or Moei) fault is a strike slip fault in northern Thailand, located northwest near and paralleling the western border. An earthquake of magnitude 5.6 Mb happened on 17 February 1975, took place in Tae Song Yang district, Tak province. The Mae Ping fault can be reliably assigned as the Active Fault (Charusiri et al., 1999; Charusiri et al., 2007). TL dates indicate several fault movement ca. 0.16, 0.17, 0.22, 0.49, 0.50, 0.58, and 1.17 Ma (Hinthong, 1995). Recent studies of this fault suggest recurrence intervals measured in tens of thousands of years and slip rate of 0.17-0.73 mm/year (Saithong, 2006; Saithong et al., 2005). Over the past 40 years, Thailand has experienced mid-sized earthquakes (magnitude 5.0-5.9) 8 times or once every 5 years. Five of these tremors struck in the north, while the other 3 were centered in the west. Virtually all earthquakes recorded in Thailand were under magnitude 6.0, although significant seismic activity in far-away locations like Indonesia or Myanmar can be felt in areas with soft soil like Bangkok.

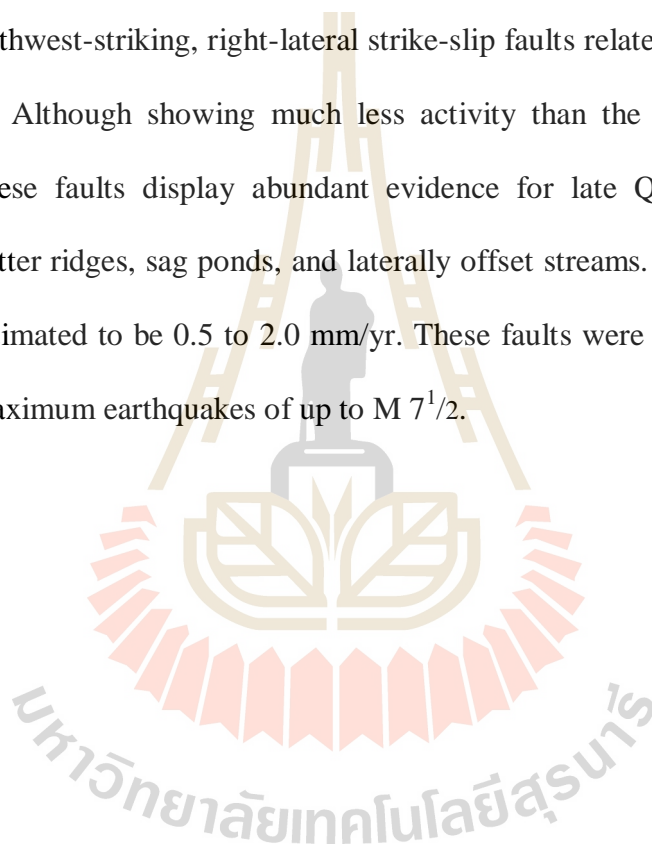
Charusiri et al. (1999) presented a critical review, to provide up-to-date information on the earthquake activities in Thailand, and to propose, based upon

several geological, geochronological, and seismological information, the active fault zones in Thailand. They subdivide major faults in Thailand into 5 zones (FZ), namely the northern, western-northwestern, central peninsular, southern peninsular and eastern-northeastern FZ. Not all FZ were considered to be active, especially those associated with extrusion tectonics and generated as a result of the India-Asia continental collision during middle Tertiary. Generally, the faults belonging to the southern and central peninsular FZs as well as those of the eastern-northeastern FZs were inferred to be potentially to tentatively active (PAF to TAF). Those faults of the northern and western-northwestern FZs were mostly regarded as active faults (AF). Based upon the fault activity in conjunction with the seismic zoning maps, the seismic risk map of Thailand was proposed.

Charusiri et al. (2011) studied the active faults in Kanchanaburi, western Thailand, particularly their orientation and movement history. The results from integrated data indicated 2 major fault zones, Three Pagoda fault zone (TPFZ) in the northwest-southeast (NW-SE) trend and Si Sawat fault zone (SSFZ) in northnorthwest-southsoutheast (NNW-SSE) trend. The last event of TPFZ occurred between 5,000-2,200 years ago with a maximum slip rate of 0.22-0.5 mm/yr and SSFZ occurred between 5,800 years ago with a maximum slip rate of 0.67 mm/yr.

Fenton et al. (2003) studied the number of active faults in Northern and Western Thailand. Northern Thailand was an intraplate basin and range province, comprised of north-south-trending Cenozoic intermontane grabens and half grabens, bounded by north- to northwest-striking normal to normal-oblique faults and northeast-striking left-lateral strike-slip faults. The basin-bounding normal faults were marked by steep, linear range fronts with triangular facets and wineglass canyons and

have slip rates of 0.1 to 0.8 mm/yr. Based on limited data; the average vertical displacement-per-event was about 1.0 to 1.5m. These faults were characterized by recurrence intervals of thousands to tens of thousands of years and were capable of generating earthquakes up to moment magnitude (M) 7, and larger. The northeast-striking strike-slip faults were marked by shutter ridges, and deflected drainages. Slip rates were 3 mm/yr or less. Western Thailand was dissected by a number of northwest- and north-northwest-striking, right-lateral strike-slip faults related to the Sagaing Fault in Myanmar. Although showing much less activity than the faults in neighboring Myanmar, these faults display abundant evidence for late Quaternary movement, including shutter ridges, sag ponds, and laterally offset streams. The slip rate on these faults was estimated to be 0.5 to 2.0 mm/yr. These faults were considered capable of generating maximum earthquakes of up to M 7<sup>1/2</sup>.

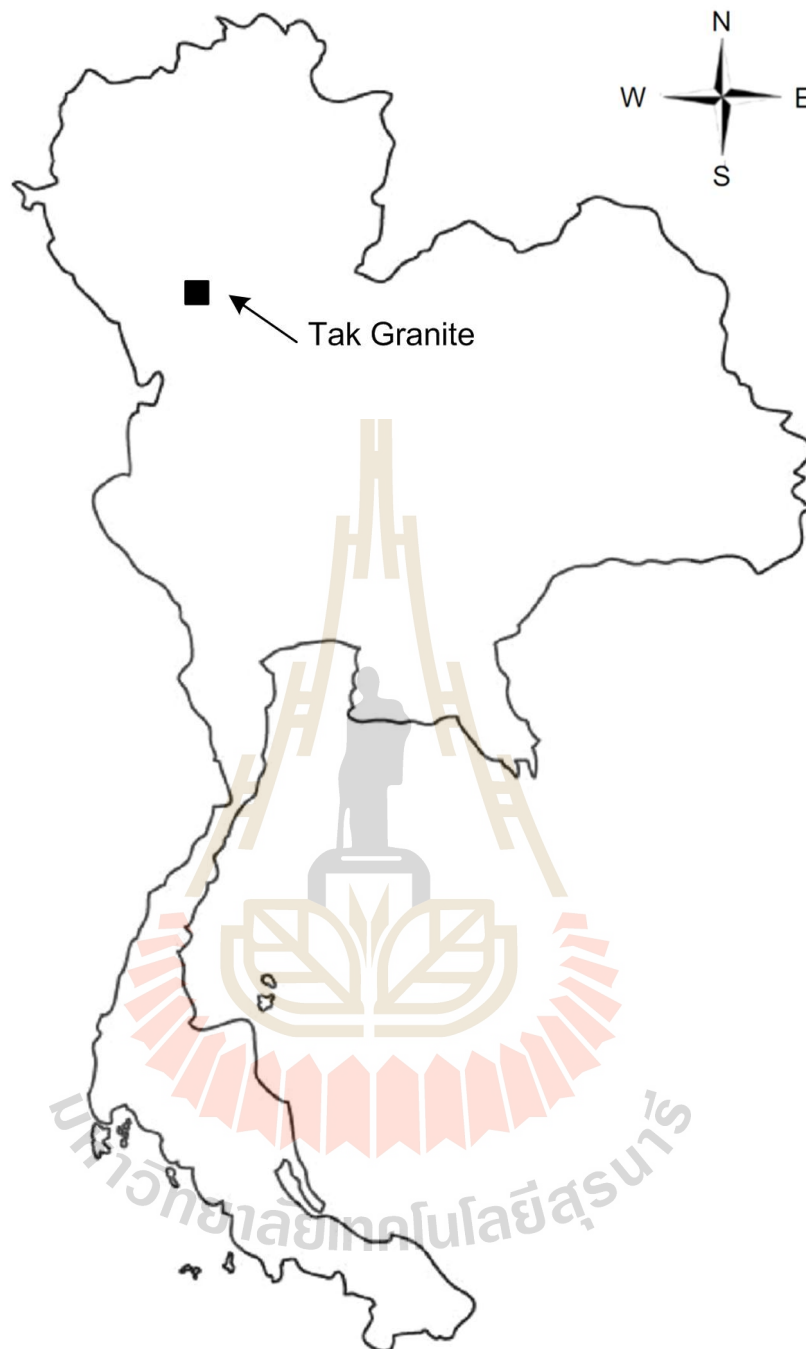


## CHAPTER III

### SAMPLE PREPARATION

#### 3.1 Introduction

Samples of the Tak granite from Tak province, Thailand, were selected for this study. Mahawat et al. (1990) gave detailed description and explained origin of the Tak granite. According to, Tak Pluton was cut by faults into the Eastern and Western plutons, contacts with Lower Palaeozoic sediments by faults. It is surrounded by extensive microgranite, porphyry and pegmatite dykes. The granite batholith is exposed in the northwest of Thailand where there are several active faults and seismic activities (Fenton et al., 2003). The tested granite was of fine texture with average sizes of 4-5 mm. The rock comprises 40% plagioclase (with grain sizes of 0.5-1 mm), 30% quartz (2-5 mm), 5% orthoclase (3-5 mm), 3% amphibole (1-2 mm), and 2% biotite (1-2 mm) (Kemthong and Fuenkajorn, 2007). Rodklang et al. (2015) determined the mechanical properties of the Tak granite to have: uniaxial compressive strength =  $118 \pm 5.2$  MPa, elastic modulus = 13.8 GPa, Poisson's ratio = 0.28, cohesion = 17.6 MPa, and internal friction angle =  $58^\circ$ . Table 3.1 shows the thermal properties of Tak granite.



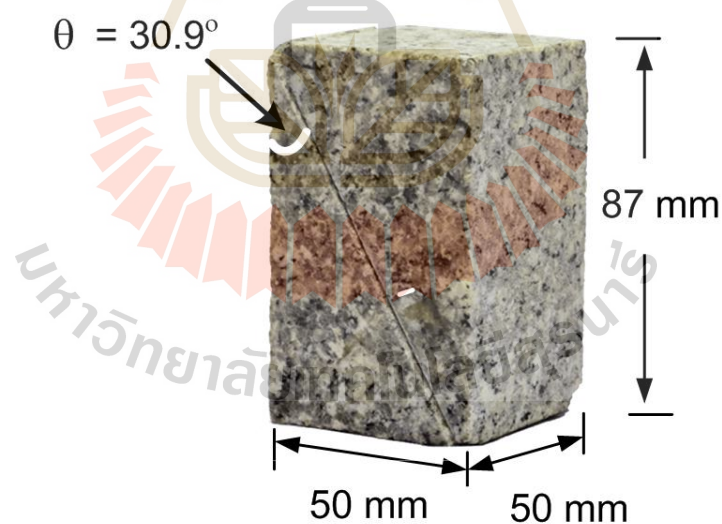
**Figure 3.1** Sampling location of Tak granite samples.

**Table 3.1** Thermal properties of Tak granite (Rodklang et al., 2015).

Property	Value
Thermal diffusivity (mm <sup>2</sup> /s)	1.71±0.04
Thermal conductivity(W/mK)	2.22±0.01
Specific heat (MJ/m <sup>3</sup> K)	1.30±0.03
Thermal expansion (K <sup>-1</sup> )	1.8×10 <sup>-7</sup>

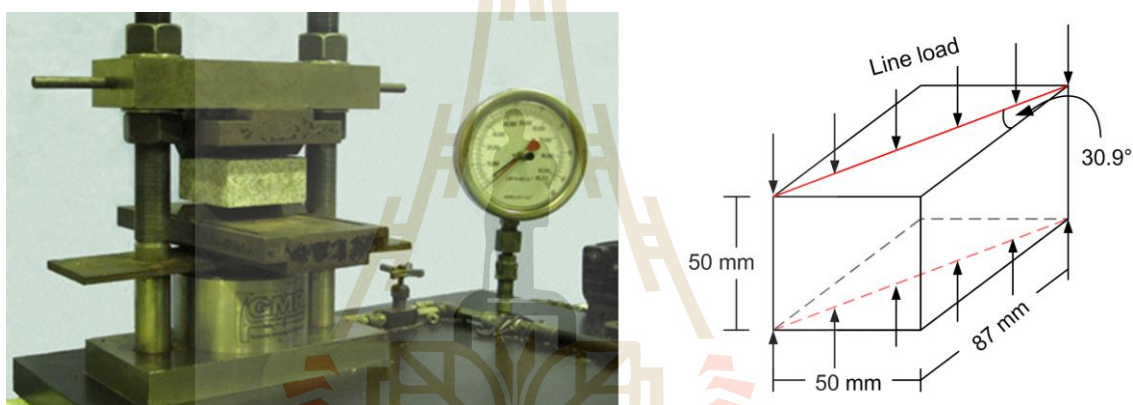
### 3.2 Sample preparation

The specimens were prepared to obtain rectangular blocks with nominal dimensions of 50×50×87 mm<sup>3</sup>. The fractures having nominal areas of 50×100 mm<sup>2</sup> are shown in Figure 3.2.

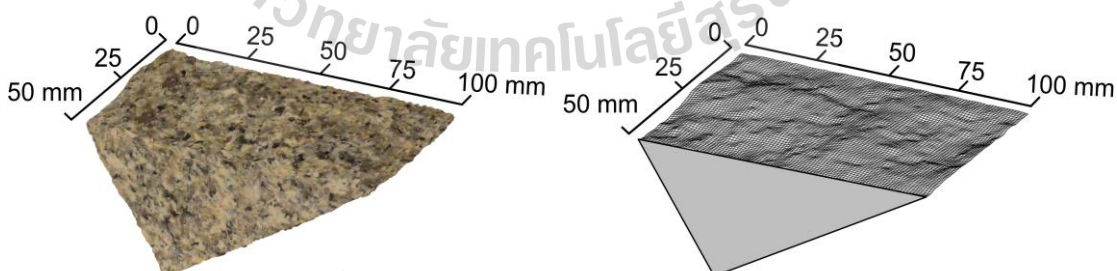
**Figure 3.2** Specimen dimensions.

The fractures were artificially made in the laboratory by tension inducing method (Figure 3.3). The normal to the fracture plane made an angle of about 59°

with the axis of the specimens. All fractures were clean and well mated. The asperity amplitudes on the fracture planes were measured from the laser-scanned profiles along the shear direction. The readings were made to the nearest 0.01 mm. Figure 3.4 shows laser scanned images of a tension-induced fracture. The maximum amplitudes were used to estimate the joint roughness coefficients (JRC) of each fracture based on Barton's chart (Barton, 1982) (Figure 3.6). Average JRC is equal to  $13 \pm 1$ . Figures 3.7-3.12 show Laser scanned profiles.



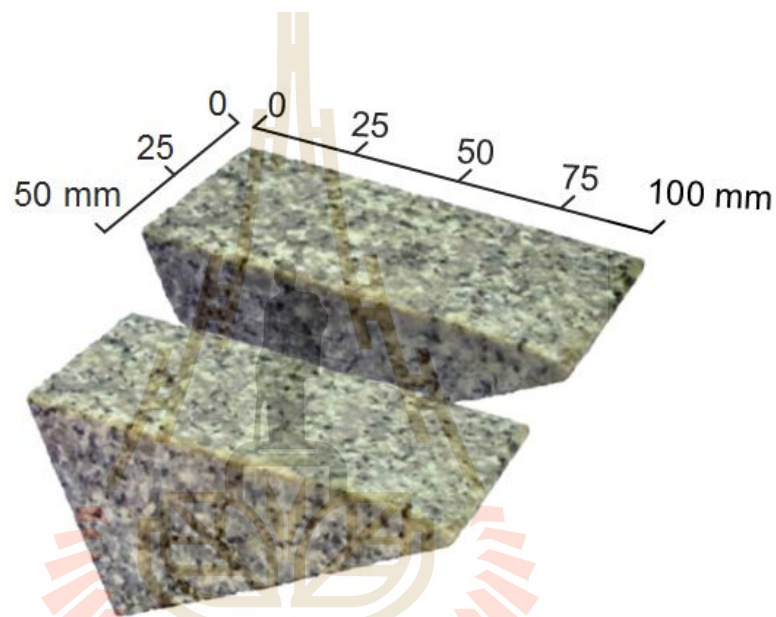
**Figure 3.3** Tension-induced fractures by line loading technique.



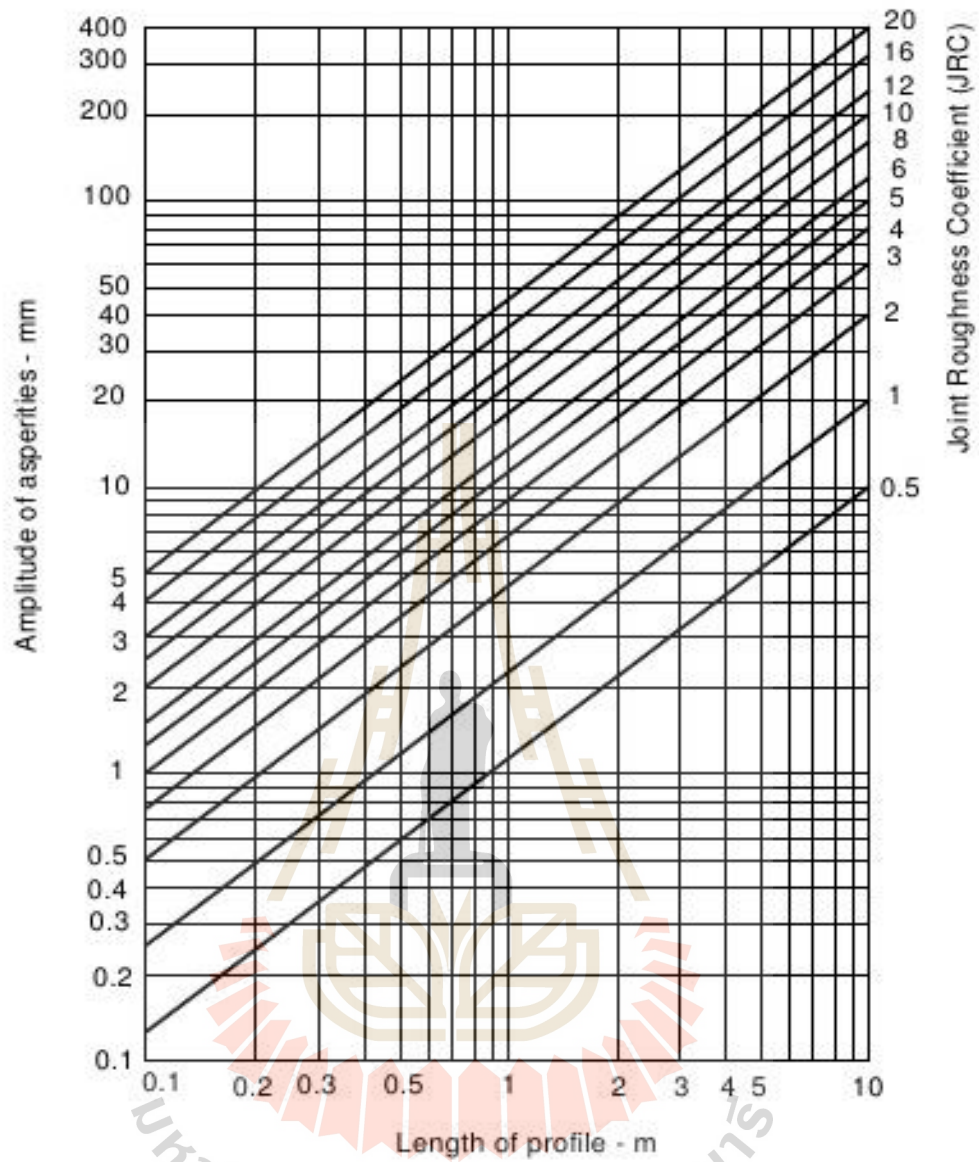
**Figure 3.4** Tension-induced fracture and its laser scanned images.



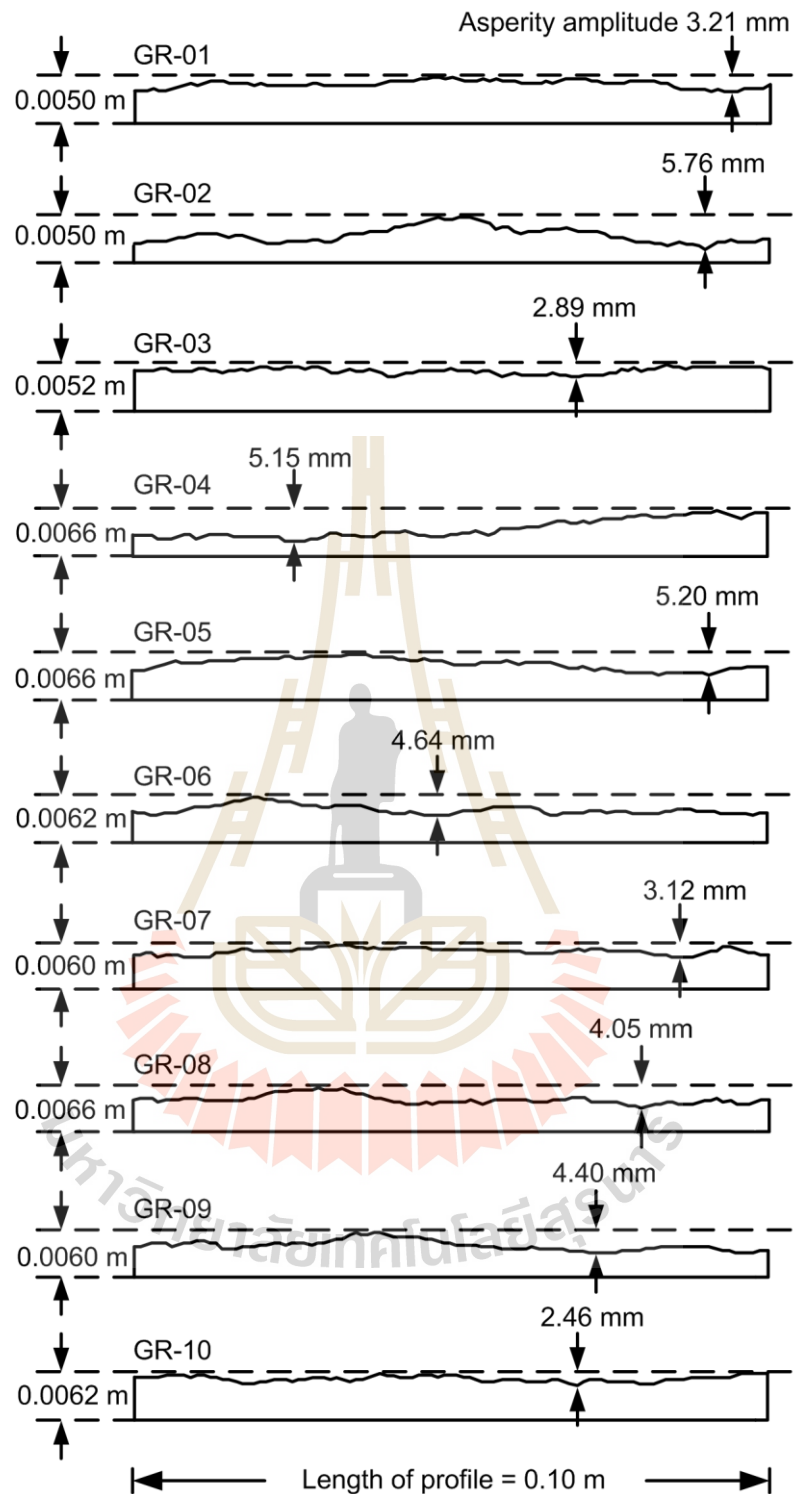
For the specimens with the saw-cut surface, two specimen blocks of each rock types were used to form a complete pair of specimens primarily to avoid the effect of the groove caused by the cutting blade (Figure 3.5). Each block is cut diagonally and hence obtaining the smooth fractures with the normal making an angle of  $60^\circ$  with the major axis of the specimen for the triaxial shear tests. Table 3.2-3.4 shows physical properties of the specimens.



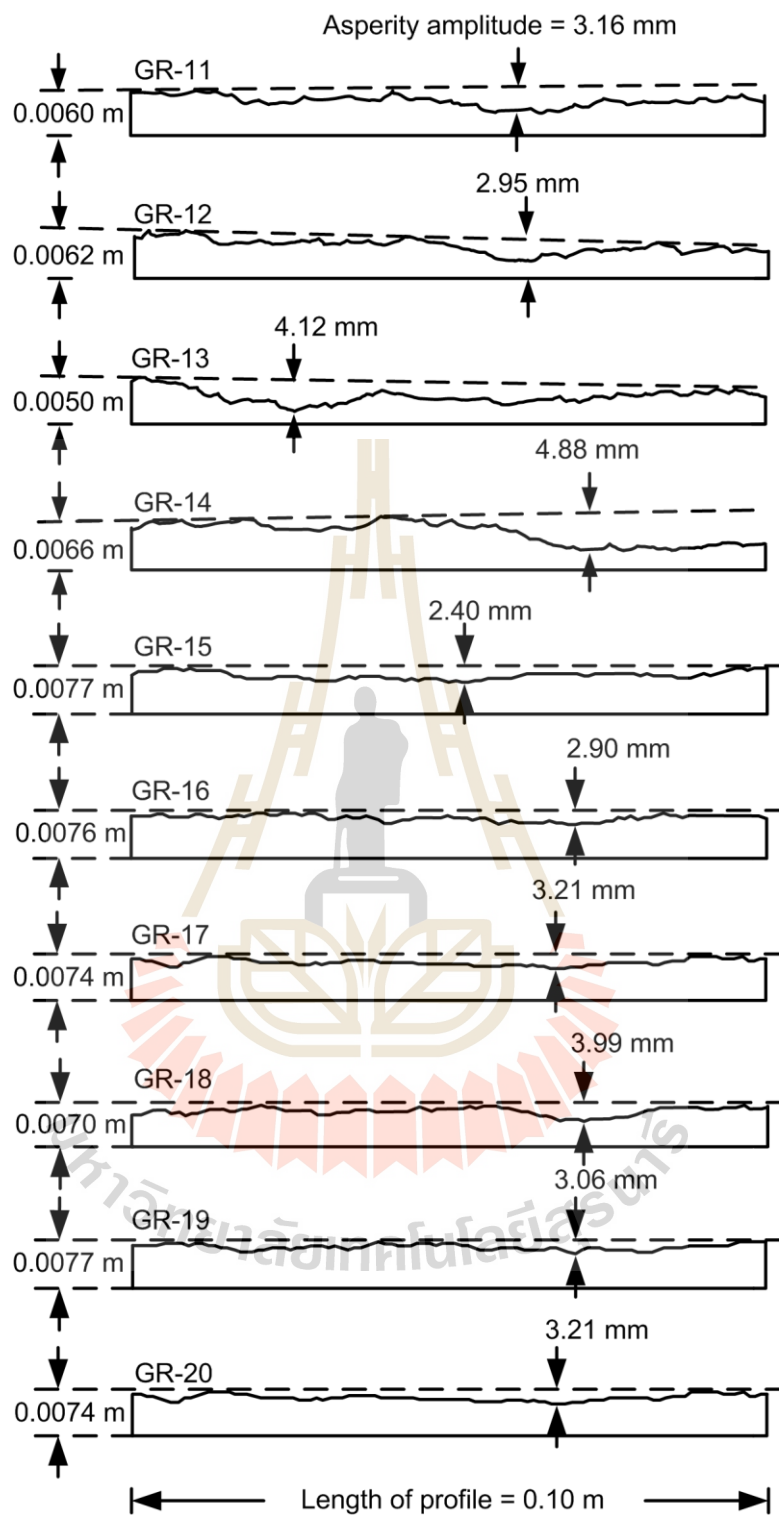
**Figure 3.5** Specimen prepared with saw-cut surface.



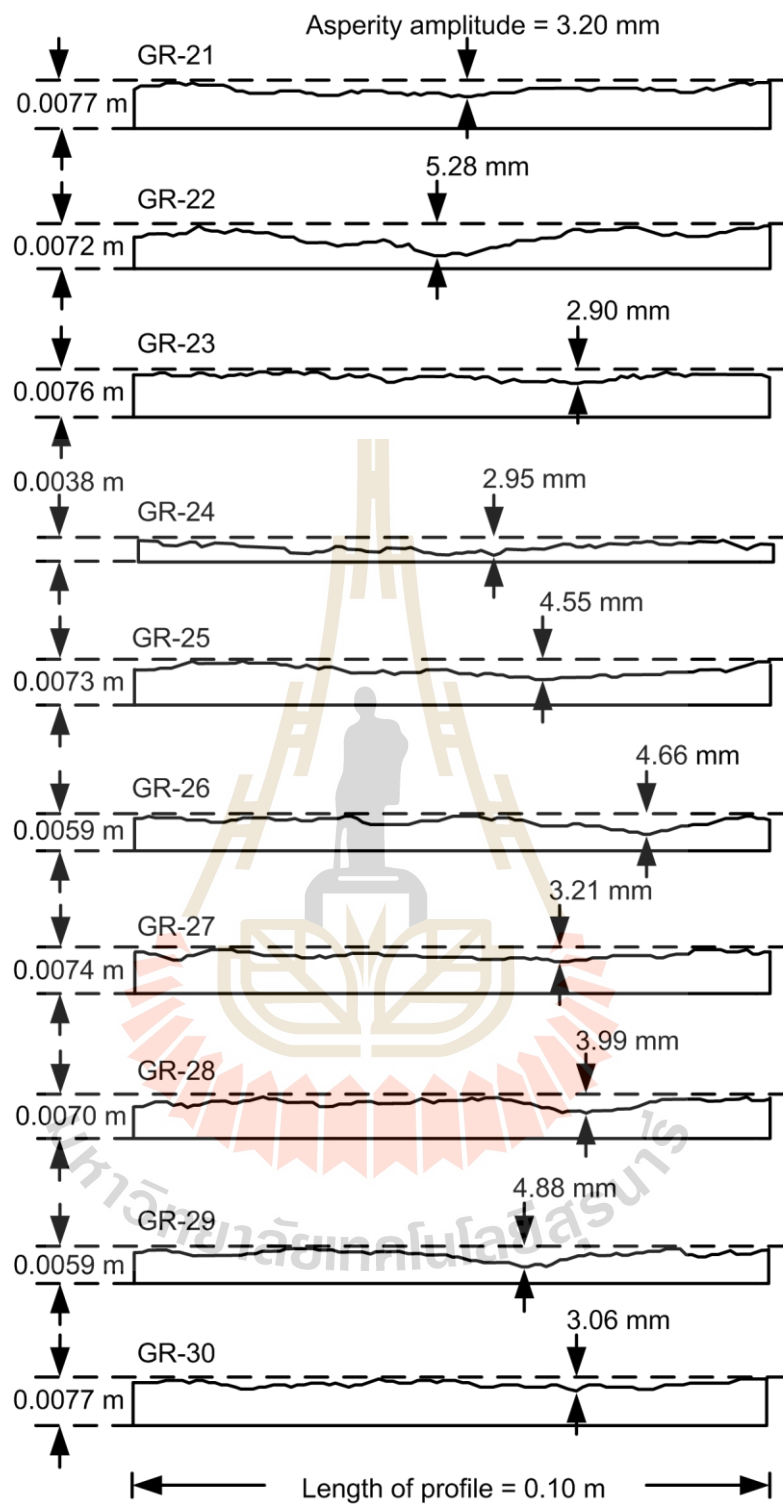
**Figure 3.6** Alternative method for estimating JRC from measurements of surface roughness amplitude from a straight edge (Barton,1982)



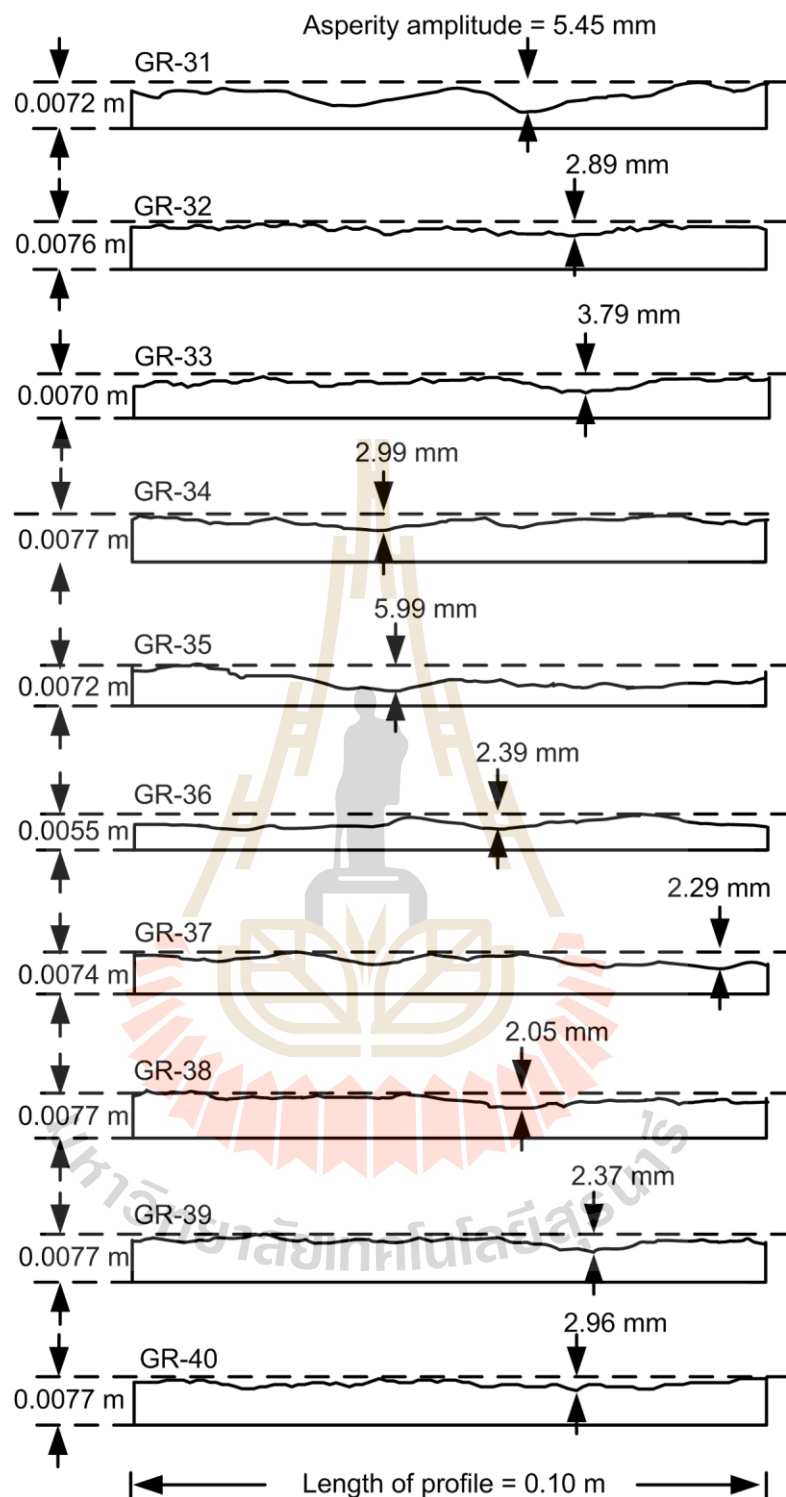
**Figure 3.7** Laser-scanned profiles to measure the maximum asperity amplitude to estimate the joint roughness coefficient (JRC).



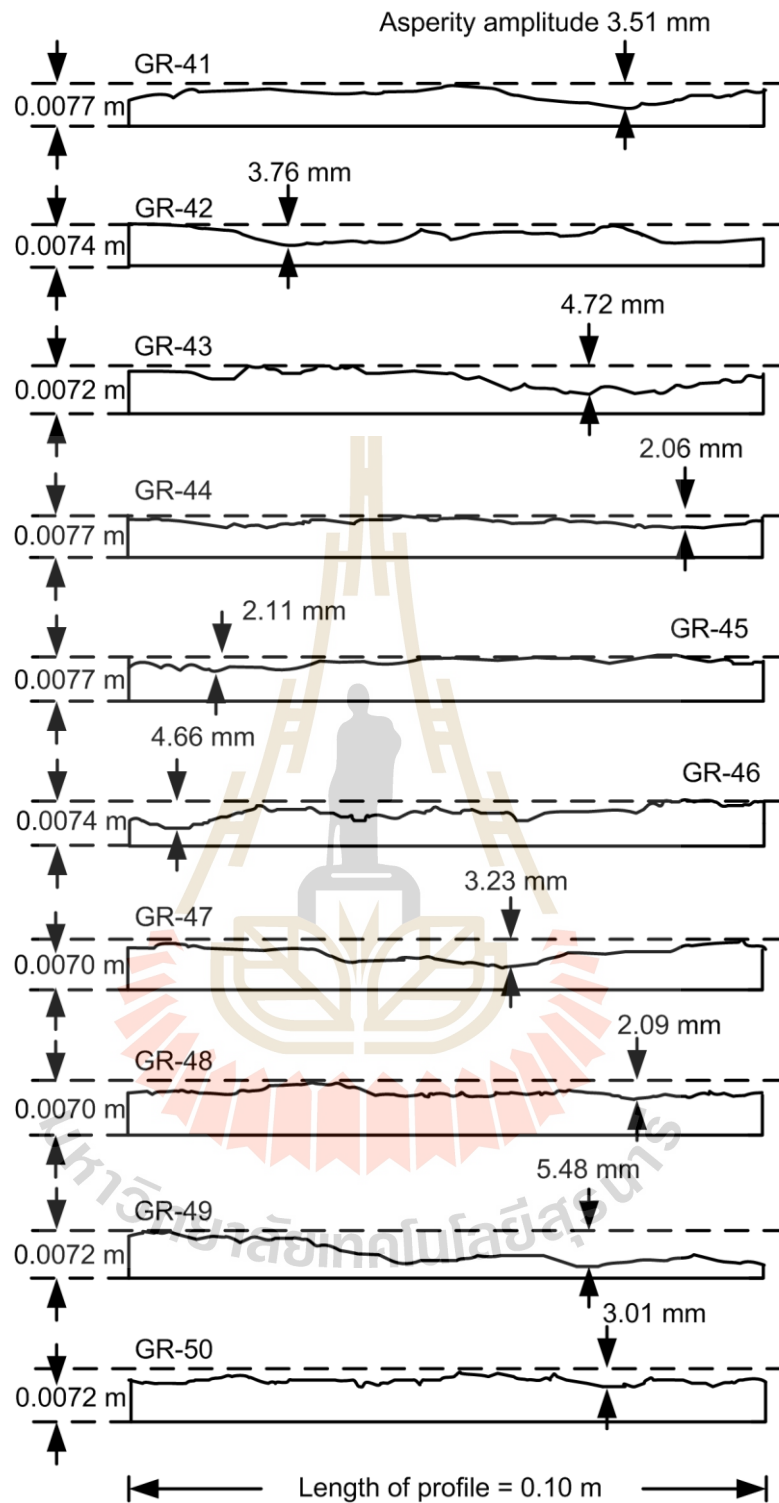
**Figure 3.8** Laser-scanned profiles to measure the maximum asperity amplitude to estimate the joint roughness coefficient (JRC) (Continue).



**Figure 3.9** Laser-scanned profiles to measure the maximum asperity amplitude to estimate the joint roughness coefficient (JRC) (Continue).

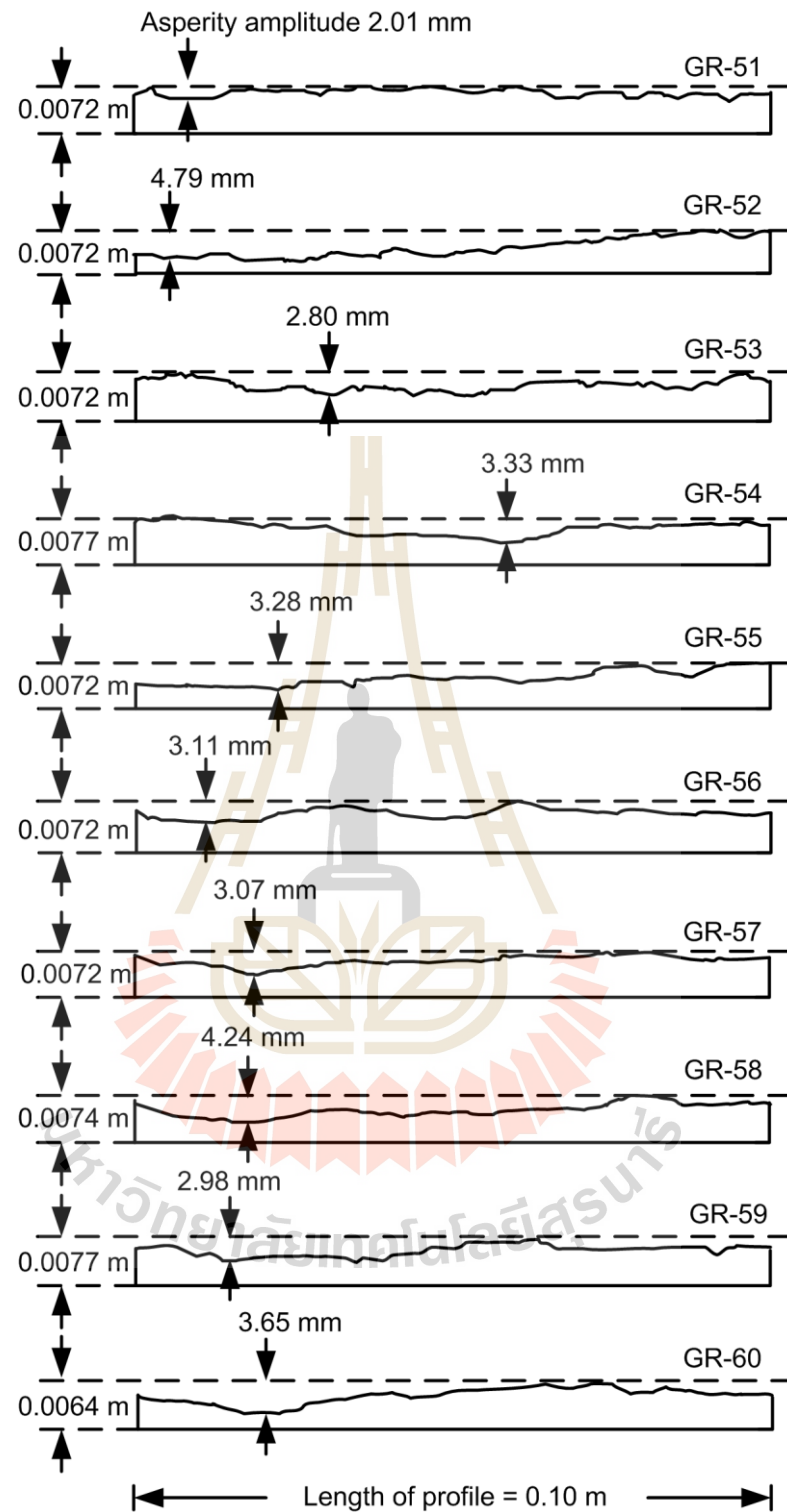


**Figure 3.10** Laser-scanned profiles to measure the maximum asperity amplitude to estimate the joint roughness coefficient (JRC) (Continue).



**Figure 3.11** Laser-scanned profiles to measure the maximum asperity amplitude to estimate the joint roughness coefficient (JRC) (Continue).





**Figure 3.12** Laser-scanned profiles to measure the maximum asperity amplitude to estimate the joint roughness coefficient (JRC) (Continue).

**Table 3.2** Specimen dimensions and JRC of the tension-induced fractures.

Specimen No.	Dimension (mm <sup>3</sup> )	Weight (g)	Density (g/cc)	JRC
GR-01	50.20×50.11×87.10	623.58	2.75	12
GR-02	50.02×50.00×87.21	626.89	2.73	13
GR-03	51.00×50.10×87.20	632.77	2.75	13
GR-04	52.10×52.00×87.00	662.81	2.75	13
GR-05	50.00×51.10×86.70	625.53	2.73	16
GR-06	49.98×49.99×86.90	609.85	2.74	16
GR-07	50.00×50.02×87.00	621.43	2.76	14
GR-08	52.00×52.00×86.92	659.82	2.72	12
GR-09	51.00×50.00×87.00	631.48	2.74	14
GR-10	51.00×51.00×87.10	635.79	2.73	14
GR-11	50.00×50.00×86.70	611.28	2.72	11
GR-12	51.10×50.10×87.72	628.67	2.73	13
GR-13	50.10×51.10×85.71	622.75	2.76	14
GR-14	52.10×51.10×87.72	659.67	2.72	13
GR-15	50.00×50.00×87.00	620.65	2.72	12
GR-16	51.10×52.20×86.73	664.15	2.74	12
GR-17	50.30×50.10×86.70	613.67	2.74	13
GR-18	50.00×50.00×87.70	606.04	2.73	16
GR-19	51.10×50.71×87.72	632.44	2.74	16
GR-20	50.30×50.20×86.71	615.34	2.75	14
GR-21	51.10×50.10×86.72	601.12	2.75	14
GR-22	50.00×50.00×87.71	613.88	2.73	13
GR-23	50.10×50.20×86.73	603.87	2.73	11
GR-24	51.20×51.30×87.72	659.69	2.74	13
GR-25	50.10×50.20×86.74	614.87	2.71	13
GR-26	49.91×50.18×85.72	598.79	2.71	14
GR-27	49.93×50.10×87.00	600.85	2.75	14
GR-28	50.10×51.15×88.72	632.56	2.73	12
GR-29	48.98×50.00×86.72	605.78	2.75	12
GR-30	52.20×51.35×86.74	640.67	2.75	14

**Table 3.3** Specimen dimensions and JRC of the tension-induced fractures (continue).

Specimen No.	Dimension (mm <sup>3</sup> )	Weight (g)	Density (g/cc)	JRC
GR-31	49.91×50.20×85.71	599.23	2.72	13
GR-32	50.10×52.02×86.72	650.22	2.73	13
GR-33	48.91×50.10×86.72	600.57	2.73	15
GR-34	50.10×51.30×85.72	600.18	2.69	15
GR-35	50.00×50.10×86.72	605.71	2.66	13
GR-36	50.20×50.10×85.74	600.86	2.74	14
GR-37	50.10×51.33×86.71	624.83	2.74	14
GR-38	51.10×50.50×87.72	616.67	2.74	16
GR-39	50.30×51.50×88.71	638.98	2.75	16
GR-40	50.25×51.30×86.73	622.94	2.75	12
GR-41	51.20×50.20×86.74	621.57	2.72	11
GR-42	50.50×50.25×87.73	610.32	2.69	12
GR-43	51.50×50.00×87.00	625.82	2.68	14
GR-44	52.25×51.82×88.72	656.89	2.74	14
GR-45	50.10×50.00×86.73	607.47	2.74	16
GR-46	48.95×50.10×87.71	601.67	2.71	14
GR-47	52.35×50.10×87.00	646.36	2.72	12
GR-48	51.10×50.50×86.72	611.41	2.67	12
GR-49	50.00×50.20×85.74	599.96	2.66	14
GR-50	50.10×50.10×85.72	599.84	2.72	16
GR-51	49.99×50.15×88.20	605.02	2.75	13
GR-52	49.95×50.15×86.74	597.69	2.73	12
GR-53	50.10×50.35×86.72	606.95	2.69	12
GR-54	50.00×50.00×87.73	608.71	2.72	12
GR-55	52.35×51.25×85.74	658.11	2.74	13
GR-56	50.15×50.00×85.71	600.68	2.73	13
GR-57	50.15×50.10×86.72	601.29	2.68	14
GR-58	51.15×50.15×85.72	612.56	2.71	14
GR-59	50.35×50.51×88.72	610.78	2.73	12
GR-60	51.30×50.00×86.71	626.78	2.73	12
Median				13±1

**Table 3.4** Summary of granite sample dimensions of the saw-cut surfaces.

Specimen No.	Dimension (mm <sup>3</sup> )	Density (g/cc)
GR-61	52.10×51.95×86.55	2.72
GR-62	50.95×49.95×85.87	2.73
GR-63	49.52×48.92×87.10	2.72
GR-64	49.98×49.95×86.35	2.74
GR-65	51.05×50.30×88.76	2.75
GR-66	50.02×50.85×86.95	2.75
GR-67	48.99×49.82×87.00	2.74
GR-68	50.00×50.30×86.45	2.73
GR-69	49.98×51.03×85.95	2.72
GR-70	51.95×50.85×86.75	2.75



## **CHAPTER IV**

### **LABORATORY TESTING**

#### **4.1 Introduction**

The objective of this section is to experimentally determine the shearing resistance of fractures in Tak granite specimens under triaxial stresses. The effort involves performing triaxial shear tests on tension-induced fractures and smooth saw-cut surfaces under ambient and elevated temperatures by using a polyaxial load frame.

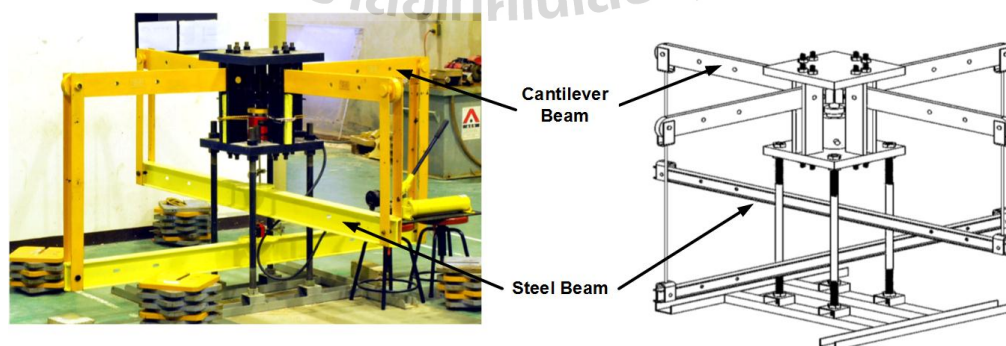
#### **4.2 Triaxial shear test on tension-induced fractures and smooth saw-cut surface**

A polyaxial load frame (Fuenkajorn et al., 2012) was used to apply triaxial stresses to the specimens because the cantilever beams with pre-calibrated dead weight can apply a truly constant lateral stresses (confining pressures) to the specimen. One of the lateral stresses was parallel to the strike of the fracture plane which is designated as  $\sigma_p$ . The other was normal to the strike of the fracture plane and designated as  $\sigma_o$ . The lateral stresses were applied by two pairs of 152 cm long cantilever beams set in mutually perpendicular directions. The outer end of each beam was pulled down by a dead weight placed on a lower steel bar linking the two opposite beams underneath. The beam inner end was hinged by a pin mounted between vertical bars on each side of the frame. During testing all beams were

arrange nearly horizontally, and hence a lateral compressive load results on the specimen placed at the center of the frame. Using different distances from the



pin to the outer weighting point and to the inner loading point, a load magnification of 17 to 1 was obtained. This loading ratio was also used to determine the lateral deformation of the specimen by monitoring the vertical movement of the two steel bars below. Figure 4.1 shows the polyaxial load frame used. The rock is installed into the polyaxial load frame. Neoprene sheets are used to minimize the friction at all interfaces between the loading platen and the rock surface. Dead weights are placed on the two lower bars to obtain the pre-defined magnitude of the lateral stresses on the specimen. Simultaneously the axial (vertical) stress is increased to the same value with lateral stresses. The specimen is first loaded under hydrostatic condition. The lateral stress ratios are varied ( $\sigma_p/\sigma_o$ ) from 0, 1, 1.5, 2, 2.5, 3 to 4, when  $\sigma_o$  varies from 1 to 18 MPa. Table 4.1 shows the test parameters for each specimen. The block specimen with the fracture is first subjected to a pre-defined initial stress where  $\sigma_1$  is first set equal to the lateral stress normal to the fracture plane ( $\sigma_3$ ). The axial stress is then increased under a constant rate of 0.01 mm/s while  $\sigma_p$  and  $\sigma_o$  are maintained constant. The axial and lateral displacements are recorded. The test is terminated when a total axial displacement of 8 mm is reached. After shearing the fractures are examined and photographed.



**Figure 4.1** Polyaxial load frame (Fuenkajorn et al., 2012).

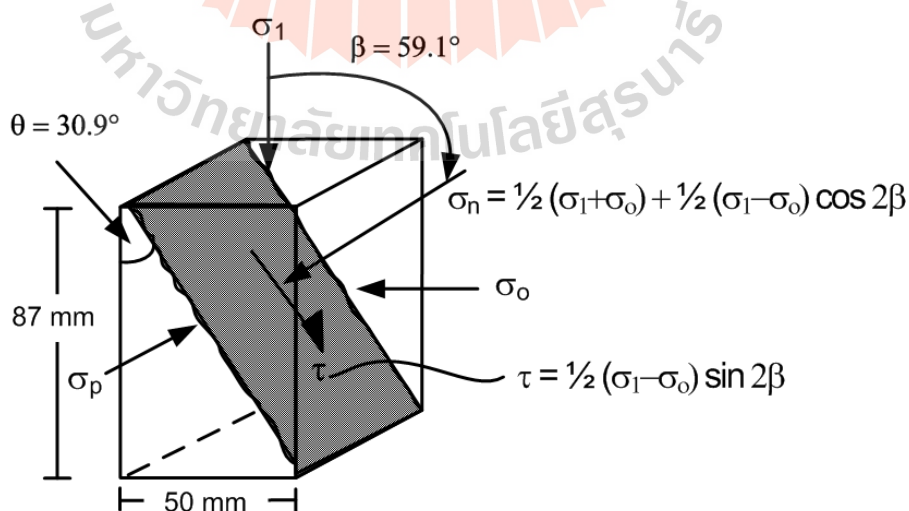


**Table 4.1** Shows the test parameters for each specimen.

Fracture Types	$\sigma_p/\sigma_o$	JRC	$\sigma_p$ (MPa)	$\sigma_o$ (MPa)
Tension-Induced Fracture	0	13	0	1
		13	0	3
		11	0	7
		10	0	12
		11	0	18
	1	13	1	1
		11	3	3
		10	7	7
		10	12	12
		11	18	18
	1.5	13	1.5	1
		13	4.5	3
		11	10.5	7
		10	18	12
	2	13	2	1
		11	6	3
		11	14	7
		13	18	9
	2.5	13	2.5	1
		13	5	2
		11	7.5	3
		11	12.5	5
		11	17.5	7
	3	11	3	1
		13	9	3
		11	15	5
		13	21	7
	4	10	4	1
		11	12	3
		10	20	5
Smooth saw-cut surface		-	0	1
	0	-	0	7
		-	0	12
		-	1	1
	1	-	7	7
		-	12	12
		-	2	1
	2	-	6	7
	-	14	12	

### 4.3 Test procedure

Each specimen was installed into the load frame with neoprene sheets placed at all interfaces between loading platens and rock surfaces to minimize the friction. Dead weights were placed on the two lower bars to obtain the pre-defined magnitude of the lateral stresses ( $\sigma_o$  and  $\sigma_p$ ) on the specimen. Simultaneously the axial (vertical) stress was increased to the same value with  $\sigma_o$  to obtain the condition where both shear and normal stresses were zero on the fracture plane. This was set as an initial stress condition. The test was started by increasing the axial stress at a constant rate using the electric oil pump while  $\sigma_p$  and  $\sigma_o$  were maintained constant. The specimen deformations in the three loading directions were monitored. The readings were recorded every 10 kN of the axial load increment until the peak shear stress was reached. Figure 4.2 shows the directions of the applied stresses with respect to the fracture orientation. It is assumed here that the sliding direction is on the  $\sigma_1$ - $\sigma_o$  plane, i.e., perpendicular to the  $\sigma_p$  axis.



**Figure 4.2** Directions of applied stresses with respect to the fracture orientation.

For the effect of temperatures on shear strength of fractures. Steel platens with heater coil are the key component for this experiment. Its dimensions are shown in Figure 4.3. The heater coil is around the steel platen (Figure 4.4). Electric heating is through a resistor converts electrical energy into heat energy. Electric heating devices use Nichrome (Nickel-Chromium Alloy) wire supported by heat resistant. A thermostat (Figure 4.5) is a component of a control system which senses the temperature of a system so that the system's temperature is maintained near a desired setpoint. A heating element converts electricity into heat through the process of resistive. Electric current passing through the element encounters resistance, resulting in heating of the element. The thermostat apparatus is SHIMAX MAC5D-MCF-EN Series DIGITAL CONTROLLER. The digital controller have a size of 48×48 mm and panel depth of 62-65 mm. Power supply is a 100-240V ± 10%AC on security surveillance system. The accuracy is ± 0.3%FS + 1digit. The thermocouple is type E1 that can measure the temperatures rang of 0-700°C.

The shear stress ( $\tau$ ) and its corresponding normal stress ( $\sigma_n$ ) can be determined from the applied principal stresses ( $\sigma_1$  and  $\sigma_o$ ) as follows (Jaeger et al., 2007; Barton, 2013):

$$\tau = \frac{1}{2}(\sigma_1 - \sigma_o) \cdot \sin 2\beta \quad (4.1)$$

$$\sigma_n = \frac{1}{2}(\sigma_1 + \sigma_o) + \frac{1}{2}(\sigma_1 - \sigma_o) \cdot \cos 2\beta \quad (4.2)$$

where  $\sigma_1$  and  $\sigma_o$  are the axial and lateral stresses and  $\beta$  is the angle between  $\sigma_1$  and  $\sigma_n$  directions. For all specimens the angle  $\beta$  equals to 59.1°.

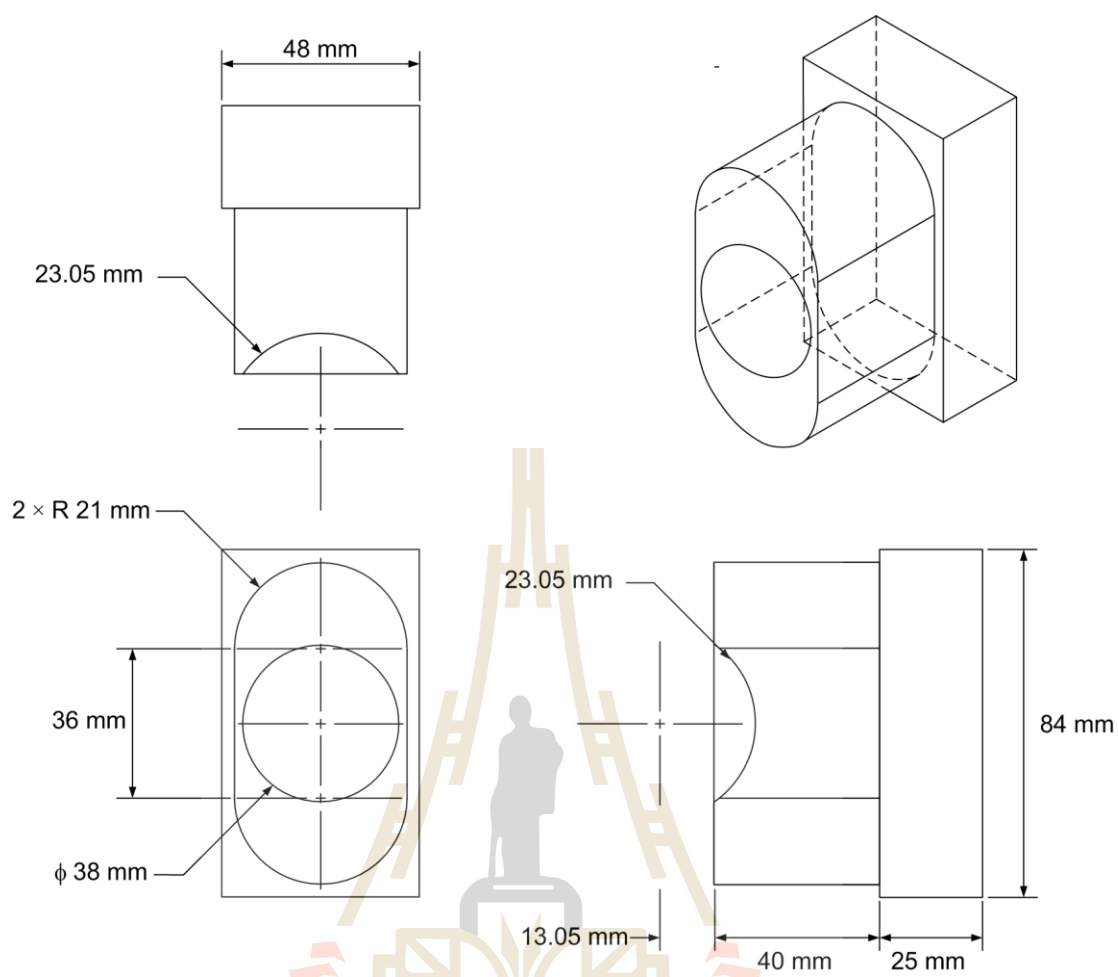


Figure 4.3 Steel platen dimensions.

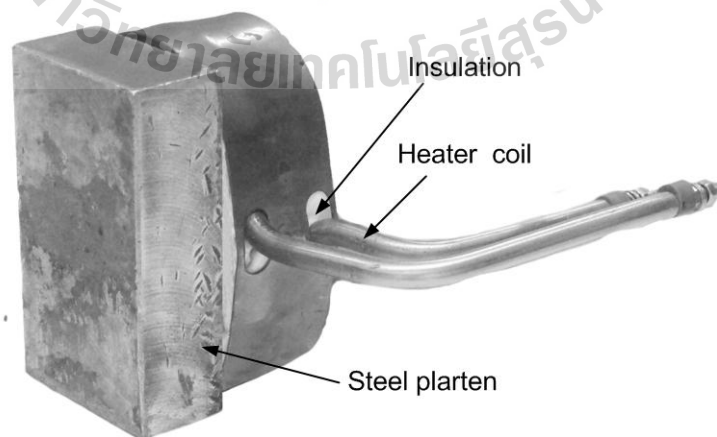
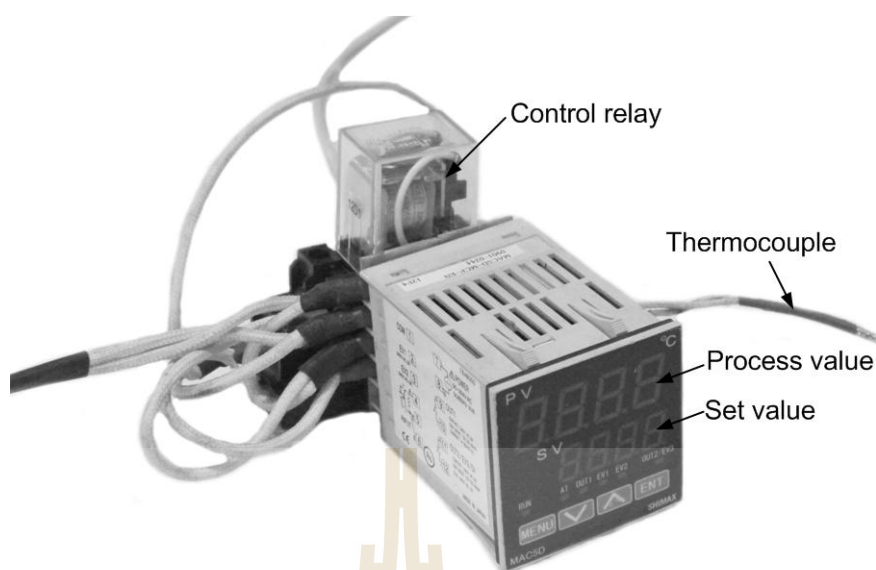


Figure 4.4 Heater coil entwined around steel platen.



**Figure 4.5** Thermostats.

The shear and normal (dilation) displacements ( $d_s$  and  $d_n$ ) can be calculated from the measured vertical and lateral displacements ( $d_1$  and  $d_3$ ) as follows (Kleppmek et al., 2016):

$$d_s = d_1 / \sin \beta \quad (4.3)$$

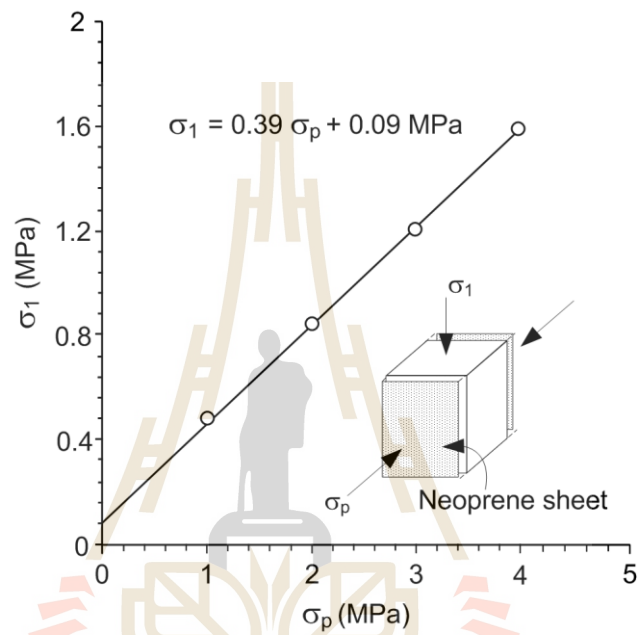
$$d_n = (d_{3,m} - d_{3,c}) \cdot \sin \beta \quad (4.4)$$

$$d_{3,c} = d_1 \cdot \tan(90 - \beta) \quad (4.5)$$

where  $d_{3,m}$  is the total lateral displacement measured during the test, and  $d_{3,c}$  are the calculated lateral displacement induced by the vertical displacement on the incline fracture plane.

The effect of the friction at the interfaces between the steel platen and the lateral neoprene sheet is measured by vertically loading an intact granite block with the

same dimensions as used above while the constant lateral stresses are applied. A linear relationship between the axial resistance and the applied lateral stresses is obtained as shown in Figure 4.6. The results are used to correct the magnitudes of the axial stress measured during the fracture shearing tests.



**Figure 4.6** Axial resistances between loading platens and neoprene sheets induced by lateral stress ( $\sigma_p$ ).

# CHAPTER V

## TEST RESULTS

### 5.1 Tension-induced fractures under different $\sigma_p/\sigma_o$ ratios

#### 5.1.1 Shear strength

For this test series the peak shear strengths are determined for the lateral stress ratios ( $\sigma_p/\sigma_o$ ) of 0, 1, 1.5, 2, 2.5, 3 and 4. A minimum of four specimens are tested for each lateral stress ratio. The condition where  $\sigma_p/\sigma_o$  is 0 and 1 is equivalent to the direct shear testing and the triaxial shear testing. Examples of the shear stress-displacement ( $\tau$ - $d_s$ ) curves for all specimens are shown in Figure 5.1. The shear and normal displacements ( $d_s$  and  $d_n$ ) are calculated by:

$$d_s = d_1 / \sin \beta \quad (5.1)$$

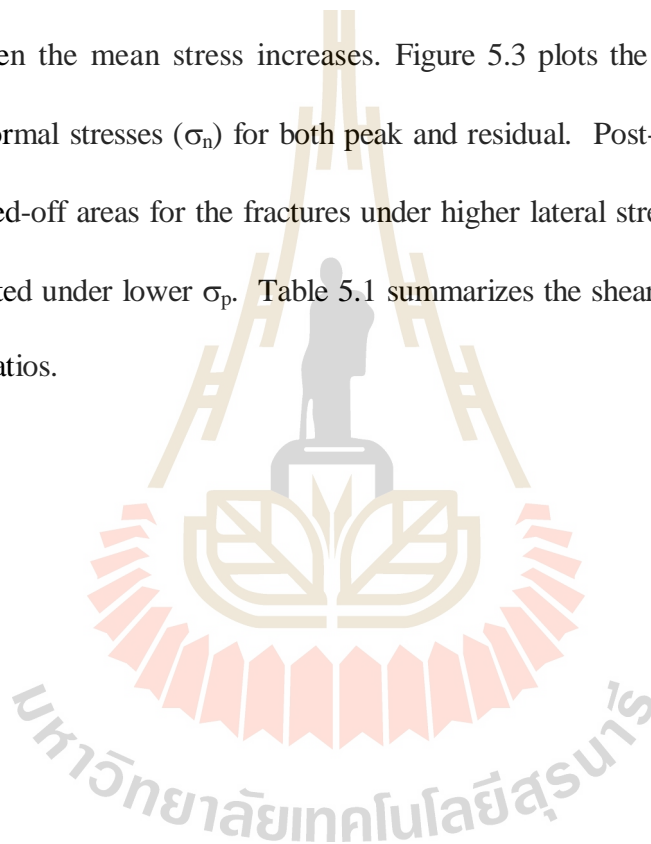
$$d_n = (d_{3,m} - d_{3,c}) \cdot \sin \beta \quad (5.2)$$

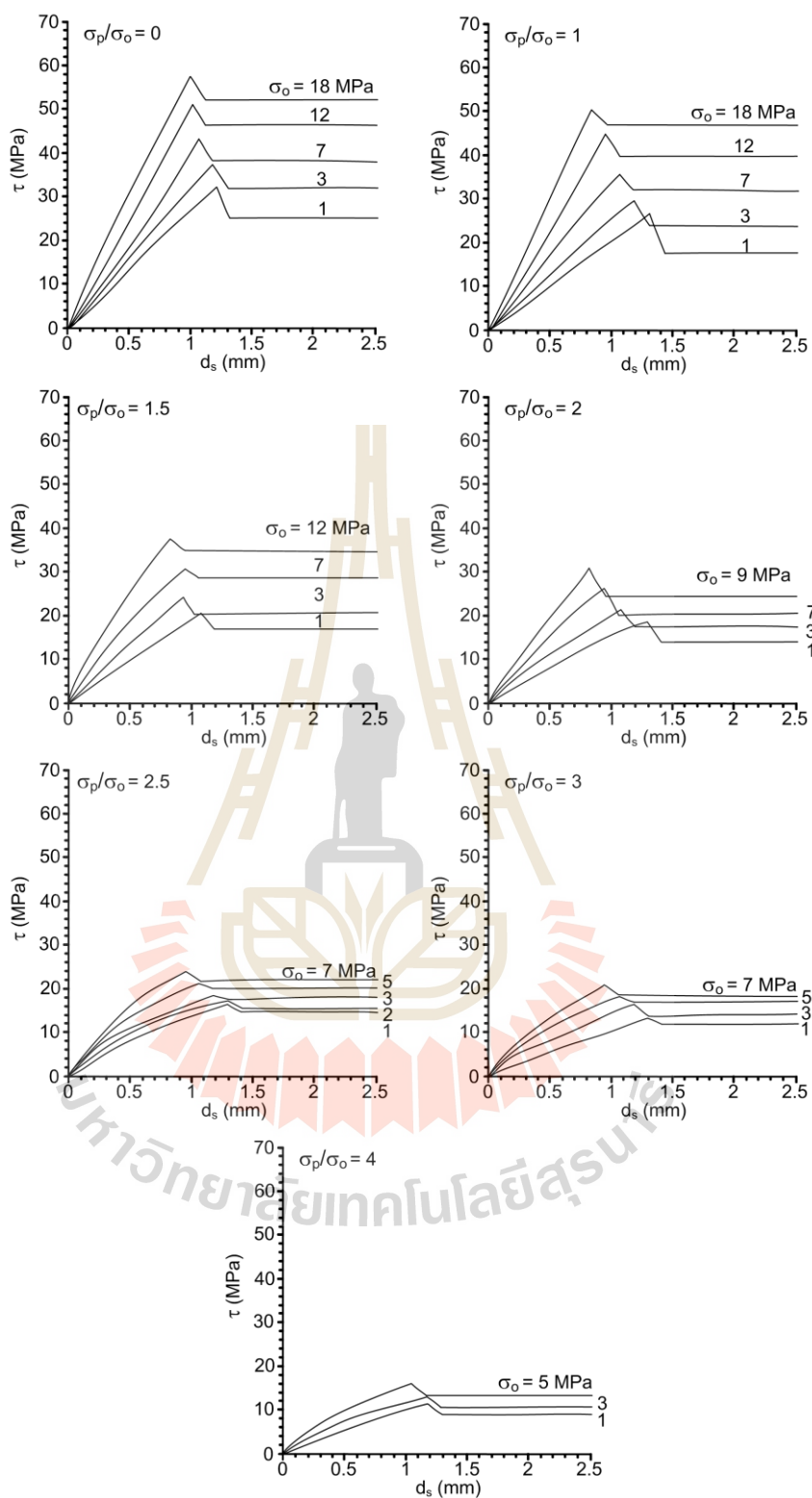
$$d_{3,c} = d_1 \cdot \tan(90 - \beta) \quad (5.3)$$

where  $d_{3,m}$  is the total lateral displacement measured during the test, and  $d_{3,c}$  are the calculated lateral displacement induced by the vertical displacement on the incline fracture plane.



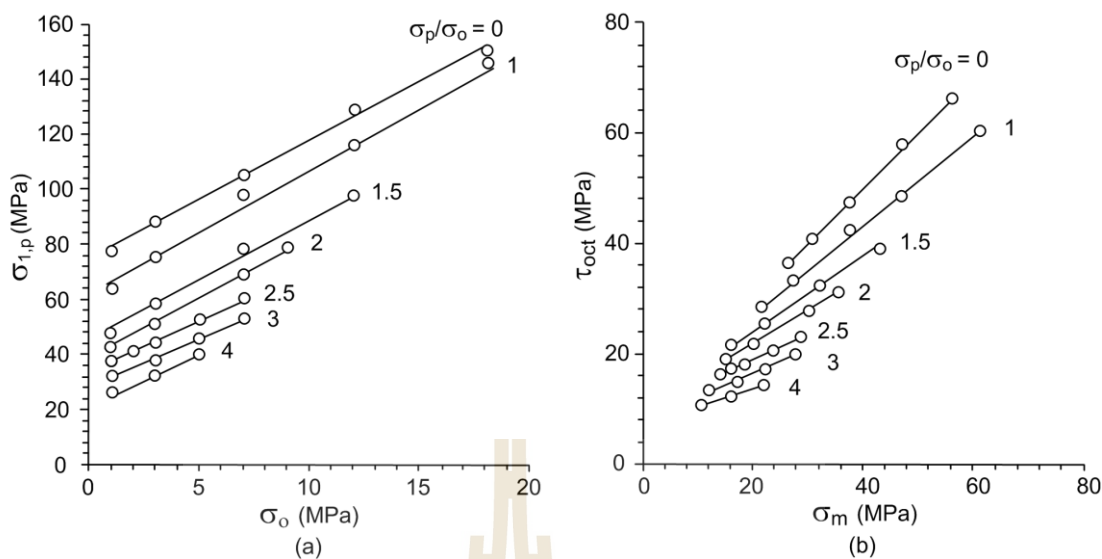
The maximum axial stresses corresponding to the peak shear strengths are plotted as a function of the lateral stress,  $\sigma_o$ , for various  $\sigma_p/\sigma_o$  ratios in Figure 5.2a, showing that the stress ratios can significantly reduce the fracture shear strengths for all  $\sigma_o$  values. To incorporate all principal stresses applied on the fractures the octahedral shear strengths ( $\tau_{oct}$ ) at the peak point are derived and presented as a function of the mean stress as shown in Figure 5.2b. The effect of the stress ratios is enhanced when the mean stress increases. Figure 5.3 plots the shear stresses ( $\tau$ ) as a function of normal stresses ( $\sigma_n$ ) for both peak and residual. Post-test observations show that the sheared-off areas for the fractures under higher lateral stress  $\sigma_p$  tend to be larger than those tested under lower  $\sigma_p$ . Table 5.1 summarizes the shear strength results for all lateral stress ratios.



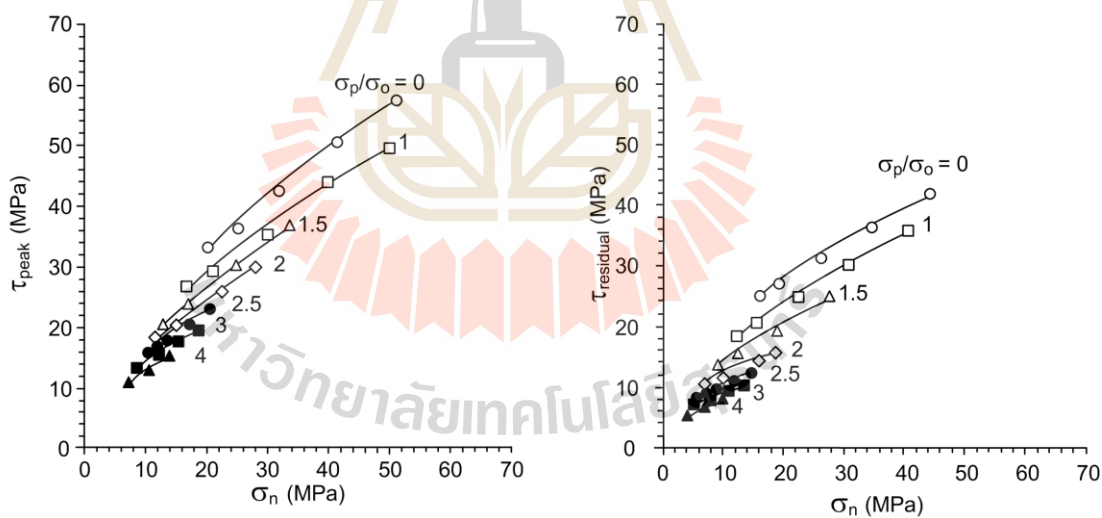


**Figure 5.1** Shear stresses ( $\tau$ ) as a function of shear displacement ( $d_s$ ) for different

$\sigma_p/\sigma_o$ .



**Figure 5.2** Major principal stresses at peak ( $\sigma_{1,p}$ ) as a function confining stresses ( $\sigma_o$ ) (a), and octahedral shear stresses as a function of mean stress (b) .



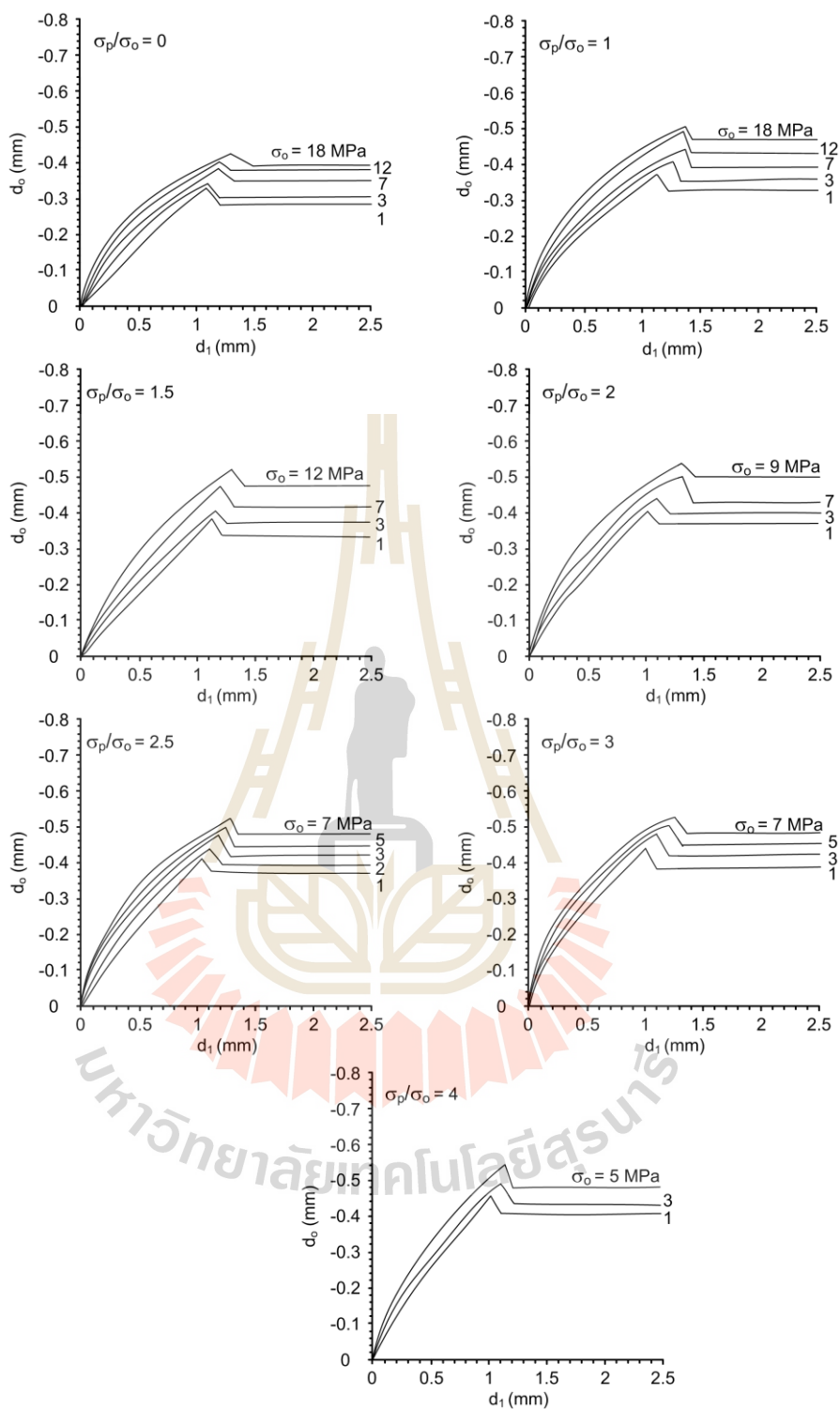
**Figure 5.3** Peak and residual shear stresses as a function of normal stress for different  $\sigma_p/\sigma_o$ .

**Table 5.1** Summary of peak shear strengths and their corresponding normal stresses for different  $\sigma_p/\sigma_o$  ratios.

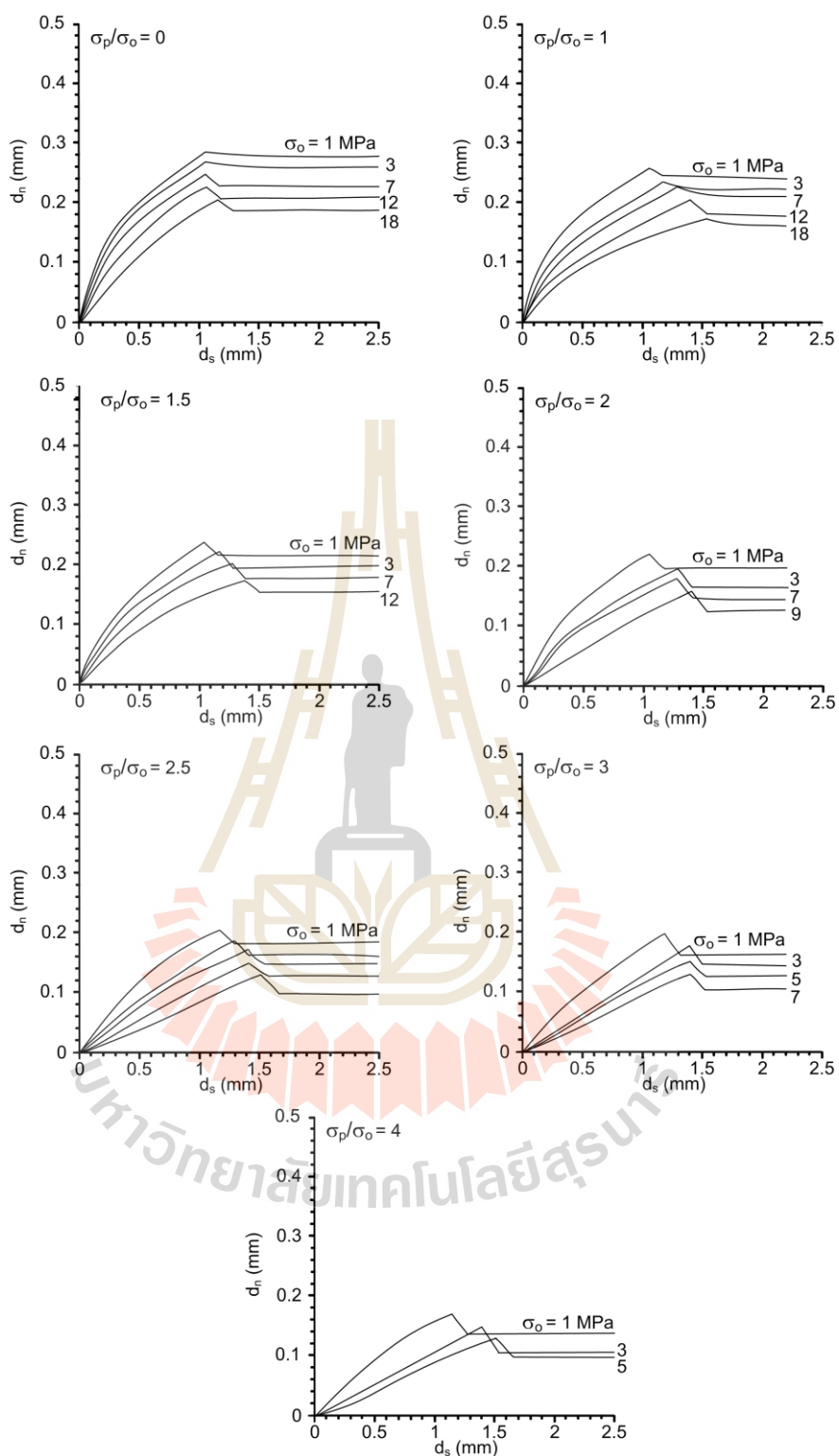
$\sigma_p/\sigma_o$	JRC	$\sigma_p$ (MPa)	$\sigma_o$ (MPa)	$\sigma_{1,peak}$ (MPa)	$\tau_{peak}$ (MPa)	$\sigma_n$ (MPa)	JRC Shear-off area
0	13	0	1	77.72	33.15	20.14	12
	13	0	3	88.40	36.43	25.19	11.5
	11	0	7	105.45	42.63	31.61	11
	10	0	12	129.46	50.77	41.31	10.5
	11	0	18	150.65	57.56	51.21	10
1	13	1	1	63.22	26.98	16.58	11.5
	11	3	3	75.30	29.31	21.07	11
	10	7	7	98.20	35.49	29.80	10.5
	10	12	12	116.59	44.20	39.83	10
	11	18	18	146.50	49.64	50.12	9.5
1.5	13	1.5	1	48.22	20.48	12.80	11
	13	4.5	3	58.80	24.03	16.95	10.5
	11	10.5	7	78.51	30.24	24.72	10
	10	18	12	98.28	37.00	33.57	9.5
2	13	2	1	41.18	18.45	11.65	10
	11	6	3	50.90	20.81	14.98	9.5
	11	14	7	69.38	26.12	22.34	9
	13	18	9	79.84	30.15	27.83	9
2.5	13	2.5	1	38.07	16.07	10.28	9.5
	13	5	2	40.95	16.88	11.75	9.1
	11	7.5	3	44.41	17.91	13.34	9
	11	12.5	5	52.59	20.68	16.94	8.5
	11	17.5	7	60.87	23.22	20.41	8.5
3	11	3	1	32.00	13.23	8.60	9
	13	9	3	38.22	15.80	12.12	8.5
	11	15	5	45.80	17.69	15.22	8
	13	21	7	52.62	19.74	18.40	8
4	10	4	1	26.23	10.84	7.26	8.5
	11	12	3	32.45	12.89	10.44	8
	10	20	5	40.18	15.37	13.87	7.5

### 5.1.2 Dilations

Figure 5.4 shows the lateral displacements ( $d_o$ ) as a function of vertical displacements ( $d_1$ ) for the tension-induced fractures. The diagrams show that the larger lateral stress ratios induce lower peak and residual stresses. Figure 5.5 shows the fracture dilation (normal displacement,  $d_n$ ) as a function of the shear displacement ( $d_s$ ) monitored during the test. The stress ratios also decrease the fracture dilation at the peak stress. Under the some  $\sigma_o$ , the fractures dilation at the peak strength decreases with increasing lateral stress ratios. In general this agrees with the test results obtained by Kapang et al. (2013). This may be caused by the lateral stress concentrations at the fracture asperities, and hence makes them fail more easily comparing to the lower stress ratio. This is supported by the JRC measurements obtained after shearing, as shown in Figure 5.6. The diagrams suggest that the higher stress ratio applied, the greater sheared-off area will be obtained. Table 5.2 shows some post-test specimens; showing that higher stress ratios induce larger sheared-off areas (indicated by light areas in the pictures) than those tested under lower stress ratios.

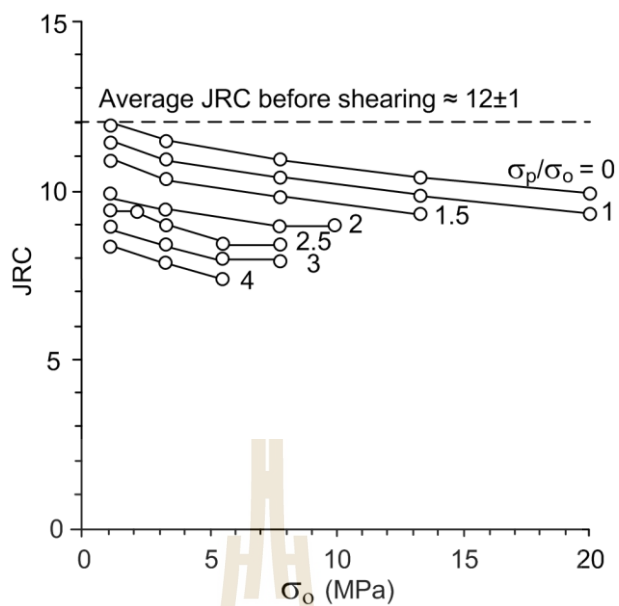


**Figure 5.4** Lateral-axial displacement ( $d_0$ - $d_1$ ) curves of tension-induced fractures for different  $\sigma_p/\sigma_o$ .





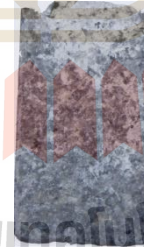







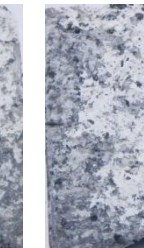
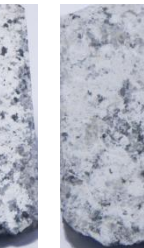
**Figure 5.5** Normal displacement ( $d_n$ ) as a function of the shear displacement ( $d_s$ ) for different  $\sigma_p/\sigma_o$ .





**Figure 5.6** Post-test JRC's as a function of  $\sigma_0$ .

**Table 5.2** Some post-test fractures under different lateral stress ratios.

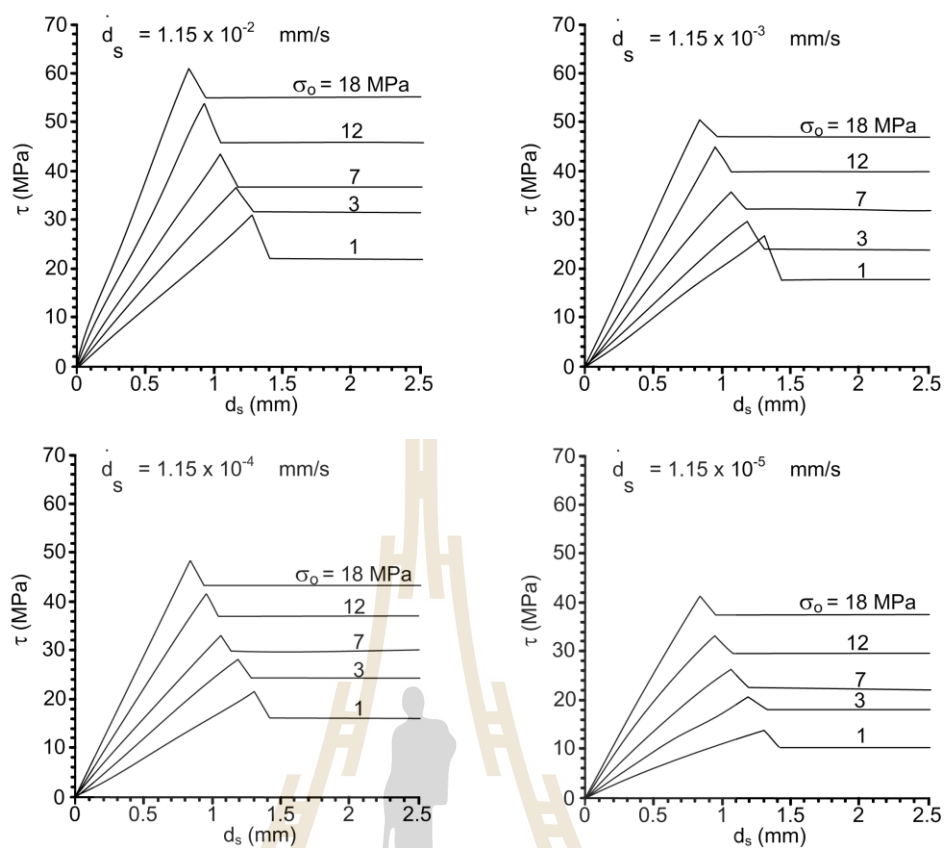
	$\sigma_p/\sigma_0$					
	0	1	2	2.5	3	4
1						
JRC	12	11.5	10	9.5	9	8.5
3						
JRC	11.5	11	9.5	9	8.5	8

## 5.2 Shear strength of tension-induced fractures under various displacement velocities

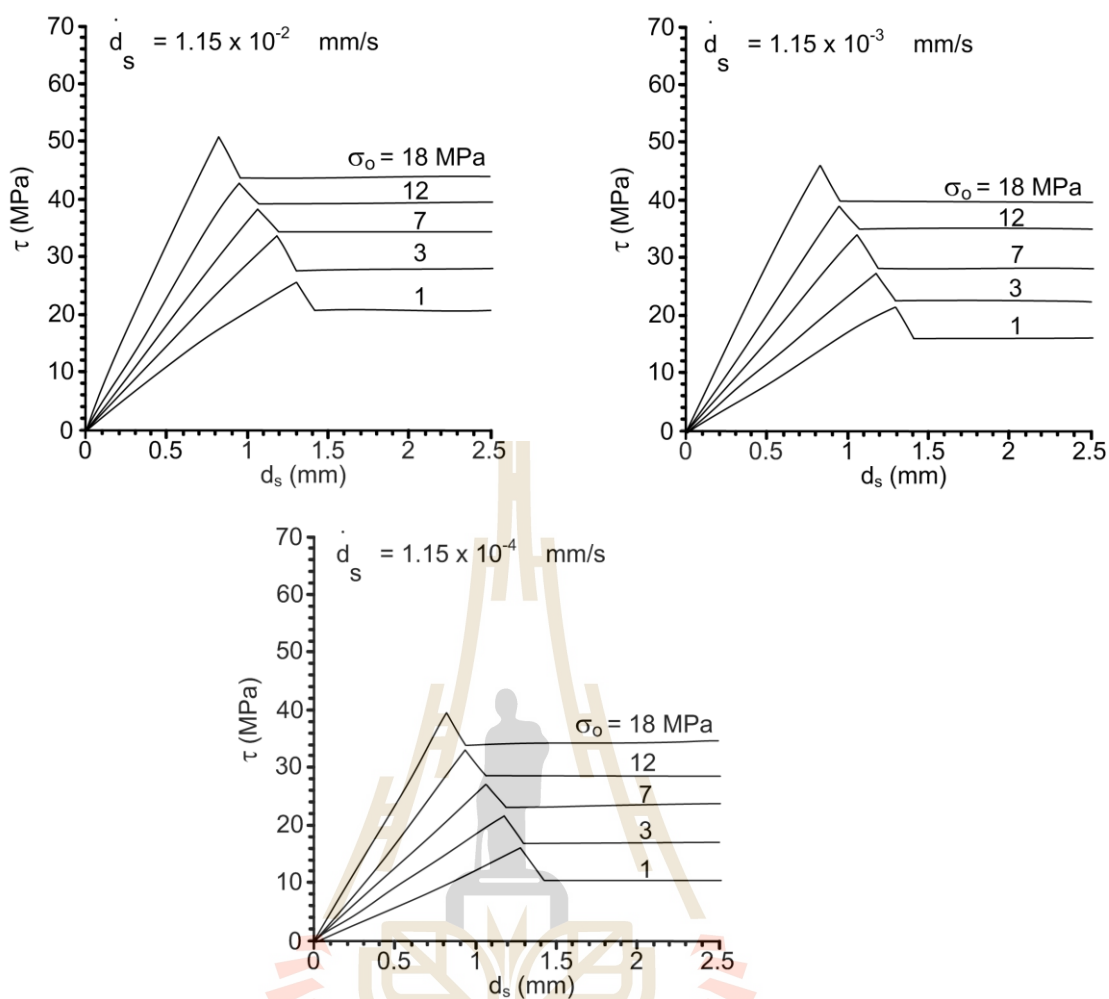
### 5.2.1 Shear strength

For this test series the shear strengths are determined for shear velocities varying from  $1.15 \times 10^{-5}$  to  $1.15 \times 10^{-2}$  mm/s with the constant confining pressures ( $\sigma_o$ ) from 1, 3, 7, 12 to 18 MPa. The lateral stress ratio is maintained constant at 1.0. Two nominal temperatures applied are 303 and 473 kelvin. The results are presented in forms of shear stress-displacement curves, shear strengths as a function of normal stress, and dilation of the fractures during shearing.

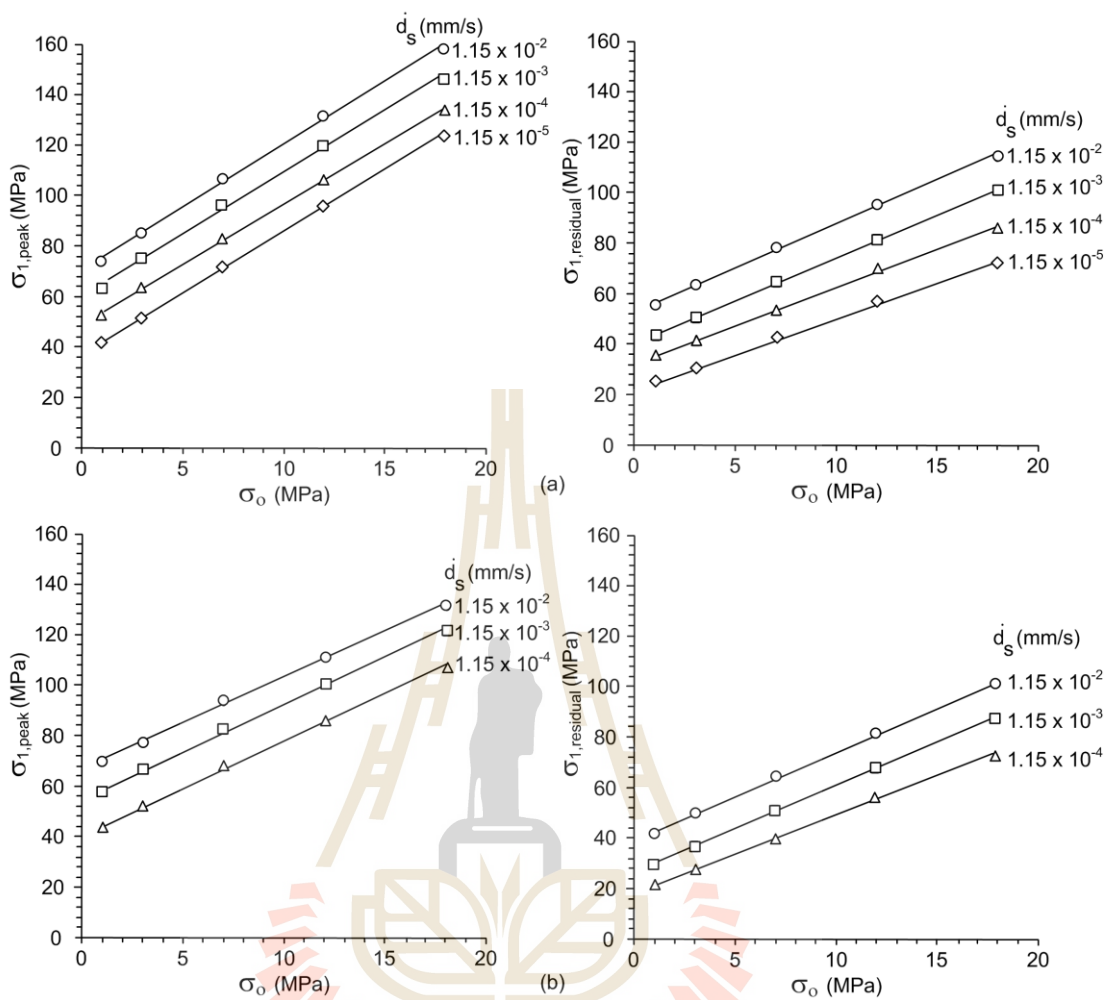
The shear stress-displacement ( $\tau$ - $d_s$ ) curve obtained under all displacement velocities and temperatures are shown in Figures 5.7 through 5.8. It is clear that the shear strengths increase with increasing the shear velocities and decreases with increasing temperature. The major principle stresses for the peak ( $\sigma_{1,P}$ ) and residual ( $\sigma_{1,R}$ ) increase with displacement velocities, and decreases with increasing temperature (Figure 5.9). The results of the triaxial shear tests performed here can be presented in the forms of the shear-normal stresses diagram. The stresses can be calculated from Eqs. (4.1) and (4.2) in chapter IV. Tables 5.3 through 5.4 show the calculation results. Figure 5.10 plots the shear stresses as a function of normal stresses for both peak and residual. Non-linear behavior of the  $\tau$ - $\sigma_n$  relation can be observed. Again the effects of the shear velocity and temperature can be seen by the reduction of the shear stresses as the shear velocities decrease and temperatures increase. The effects of shear velocity observed here agree well with those obtained by Klepemek et al., 2016.



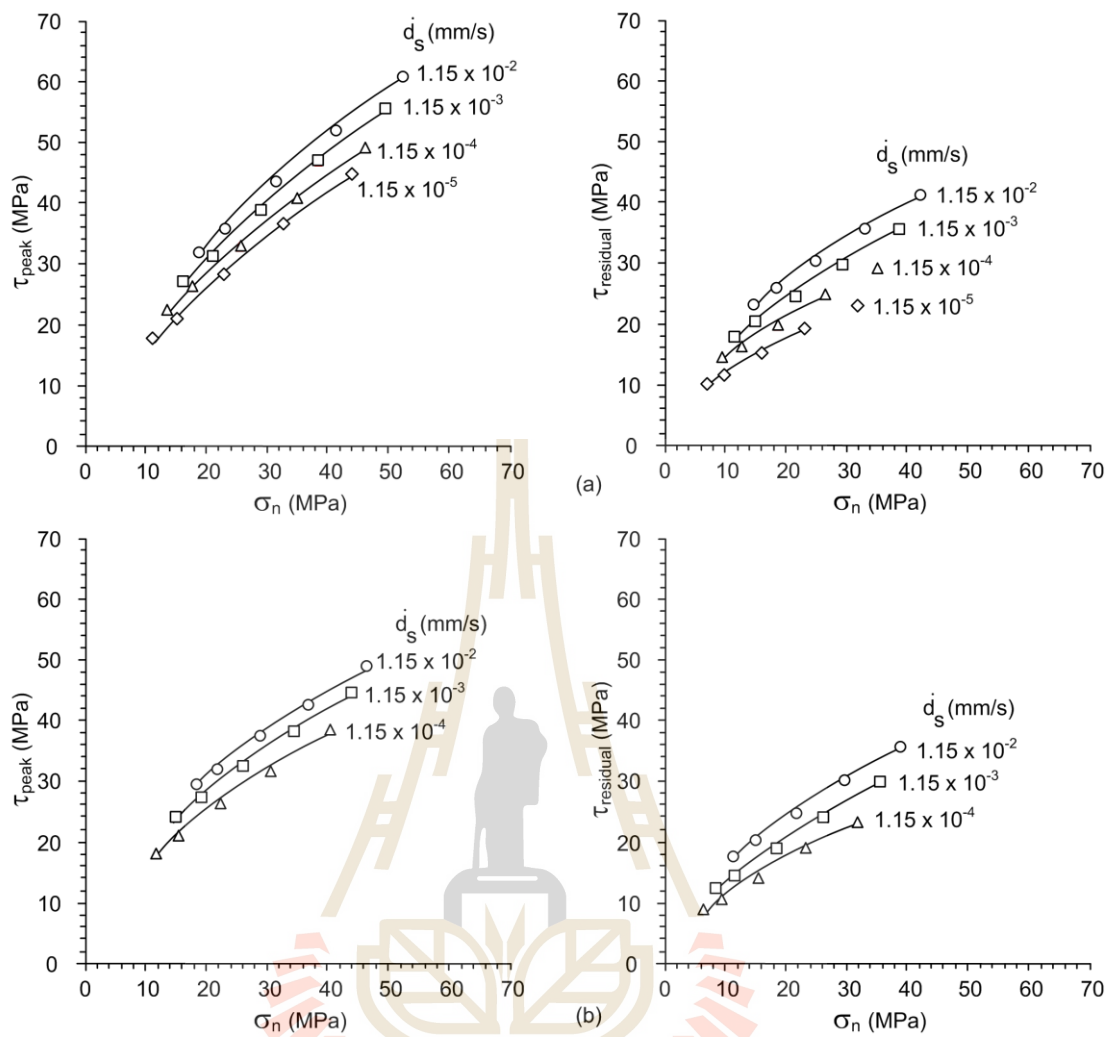
**Figure 5.7** Shear stresses ( $\tau$ ) as a function of shear displacement ( $d_s$ ) for 303 kelvin.



**Figure 5.8** Shear stresses ( $\tau$ ) as a function of shear displacement ( $d_s$ ) for 473 kelvin.



**Figure 5.9** Major principle stress ( $\sigma_1$ ) as a function of the confining stress ( $\sigma_0$ ) for 303 kelvin (a) and 473 kelvin (b).



**Figure 5.10** Peak and residual shear stresses as a function of normal stress for 303 kelvin (a) and 473 kelvin (b).

**Table 5.3** Summary of peak and residual shear strengths and their corresponding normal stresses for 303 kelvin.

$d_s$ (mm/s)	$\sigma_3$ (MPa)	Peak shear strength			Residual shear strength			JRC Shear-off area
		$\sigma_{1, \text{peak}}$ (MPa)	$\sigma_{n, \text{peak}}$ (MPa)	$\tau_{\text{peak}}$ (MPa)	$\sigma_{1, \text{residual}}$ (MPa)	$\sigma_{n, \text{residual}}$ (MPa)	$\tau_{\text{residual}}$ (MPa)	
$1.15 \times 10^{-2}$	1	73.99	18.57	30.42	55.44	14.61	23.57	12
	3	84.84	23.71	35.87	63.50	18.13	26.20	11.5
	7	106.78	31.22	41.95	77.95	24.74	30.72	11
	12	131.31	41.71	51.46	95.09	32.77	35.98	10.5
	18	158.19	52.67	60.05	114.24	42.06	41.67	10
$1.15 \times 10^{-3}$	1	63.22	16.58	26.98	43.34	11.59	18.34	11.5
	3	75.30	21.07	31.31	50.40	14.85	20.52	11
	7	98.20	29.8	39.49	64.51	21.38	24.90	10.5
	12	116.59	39.83	45.29	81.31	29.33	30.01	10
	18	146.50	50.12	55.64	100.80	38.70	35.85	9.5
$1.15 \times 10^{-4}$	1	52.42	13.16	21.06	35.28	9.57	14.84	11
	3	63.34	18.7	27.19	41.33	12.58	16.60	10.5
	7	82.59	25.71	32.41	53.26	18.56	20.03	10
	12	105.84	35.44	40.59	69.55	26.39	24.92	9.5
	18	133.39	45.26	47.21	85.68	34.92	29.31	9
$1.15 \times 10^{-5}$	1	42.07	8.54	13.07	25.20	7.05	10.48	9.5
	3	51.74	14.74	20.32	30.41	9.85	11.87	9
	7	72.24	21.76	25.56	42.67	15.92	15.45	8.5
	12	96.26	28.96	30.83	56.95	23.24	19.46	8
	18	123.98	41.76	38.88	72.24	31.56	23.49	7.5



**Table 5.4** Summary of peak and residual shear strengths and their corresponding normal stresses for 473 kelvin.

$\dot{d}_s$ (mm/s)	$\sigma_3$ (MPa)	Peak shear strength			Residual shear strength			JRC shear-off area
		$\sigma_{1, \text{peak}}$ (MPa)	$\sigma_{n, \text{peak}}$ (MPa)	$\tau_{\text{peak}}$ (MPa)	$\sigma_{1, \text{residual}}$ (MPa)	$\sigma_{n, \text{residual}}$ (MPa)	$\tau_{\text{residual}}$ (MPa)	
$1.15 \times 10^{-2}$	1	69.05	18.01	29.47	42.00	11.25	17.75	11.5
	3	76.94	21.49	32.02	50.06	14.77	20.38	11
	7	93.51	28.63	37.46	64.51	21.38	24.90	10.5
	12	110.38	36.59	42.60	81.65	29.41	30.16	10
	18	131.17	46.29	49.01	100.80	38.70	35.85	9.5
$1.15 \times 10^{-3}$	1	56.75	14.94	24.14	29.90	8.23	12.52	11
	3	66.39	18.85	27.45	36.96	11.49	14.71	10.5
	7	82.19	25.80	32.56	51.07	18.02	19.08	10
	12	100.13	34.03	38.16	67.87	25.97	24.19	9.5
	18	121.09	43.77	44.64	87.36	35.34	30.03	9
$1.15 \times 10^{-4}$	1	43.11	11.53	18.23	21.84	6.21	9.02	10.5
	3	51.71	15.18	21.09	27.89	9.22	10.78	10
	7	67.44	22.11	26.17	39.82	15.20	14.21	9.5
	12	85.18	30.29	31.69	56.11	23.03	19.10	9
	18	106.58	40.14	38.36	72.24	31.56	23.49	8.5

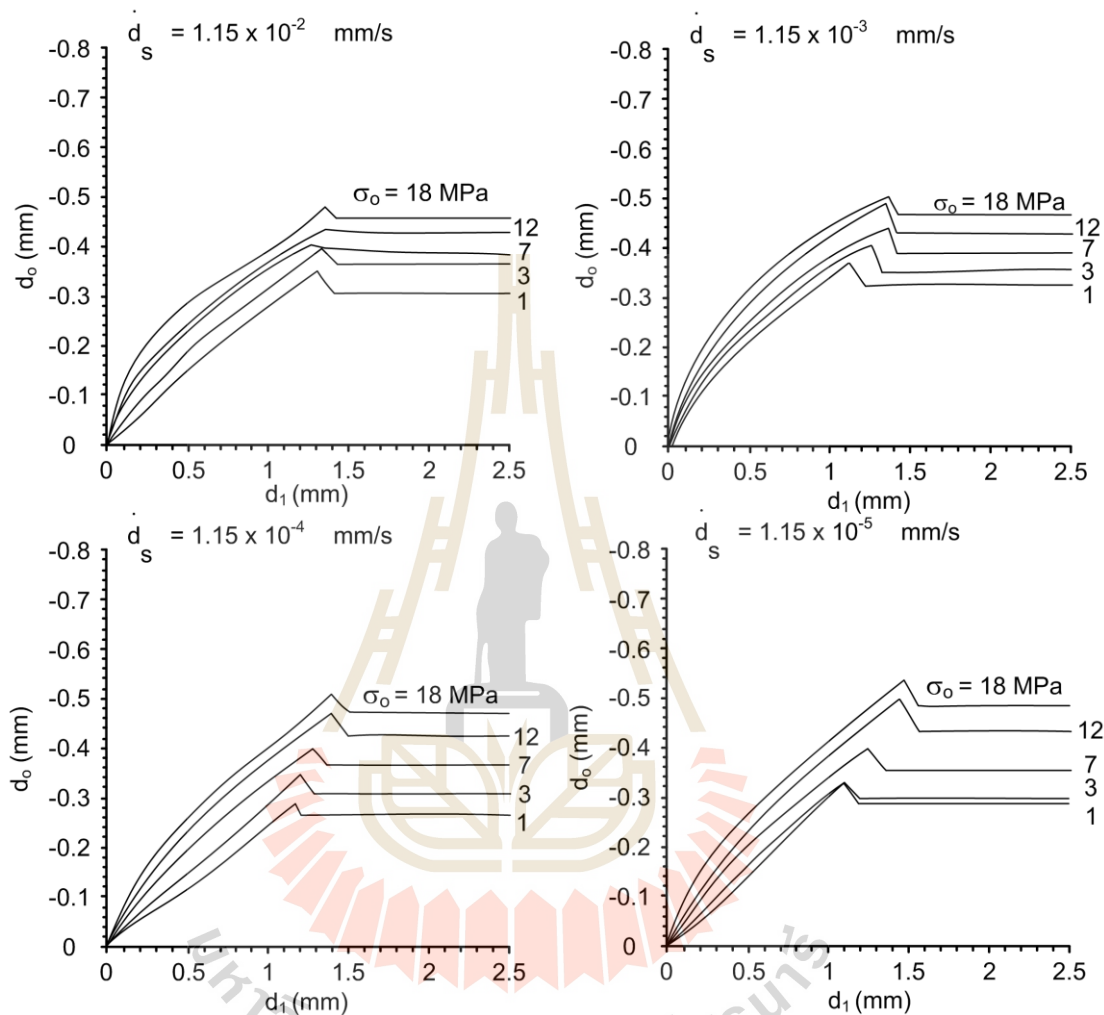
### 5.2.2 Dilation

Figures 5.11 through 5.12 show the lateral displacements ( $d_0$ ) as a function of vertical displacements ( $d_1$ ) for 303 and 473 kelvin. The diagrams show that the lateral displacement ( $d_0$ ) tends to increase with decreasing the shear velocity and decrease with increasing temperature.

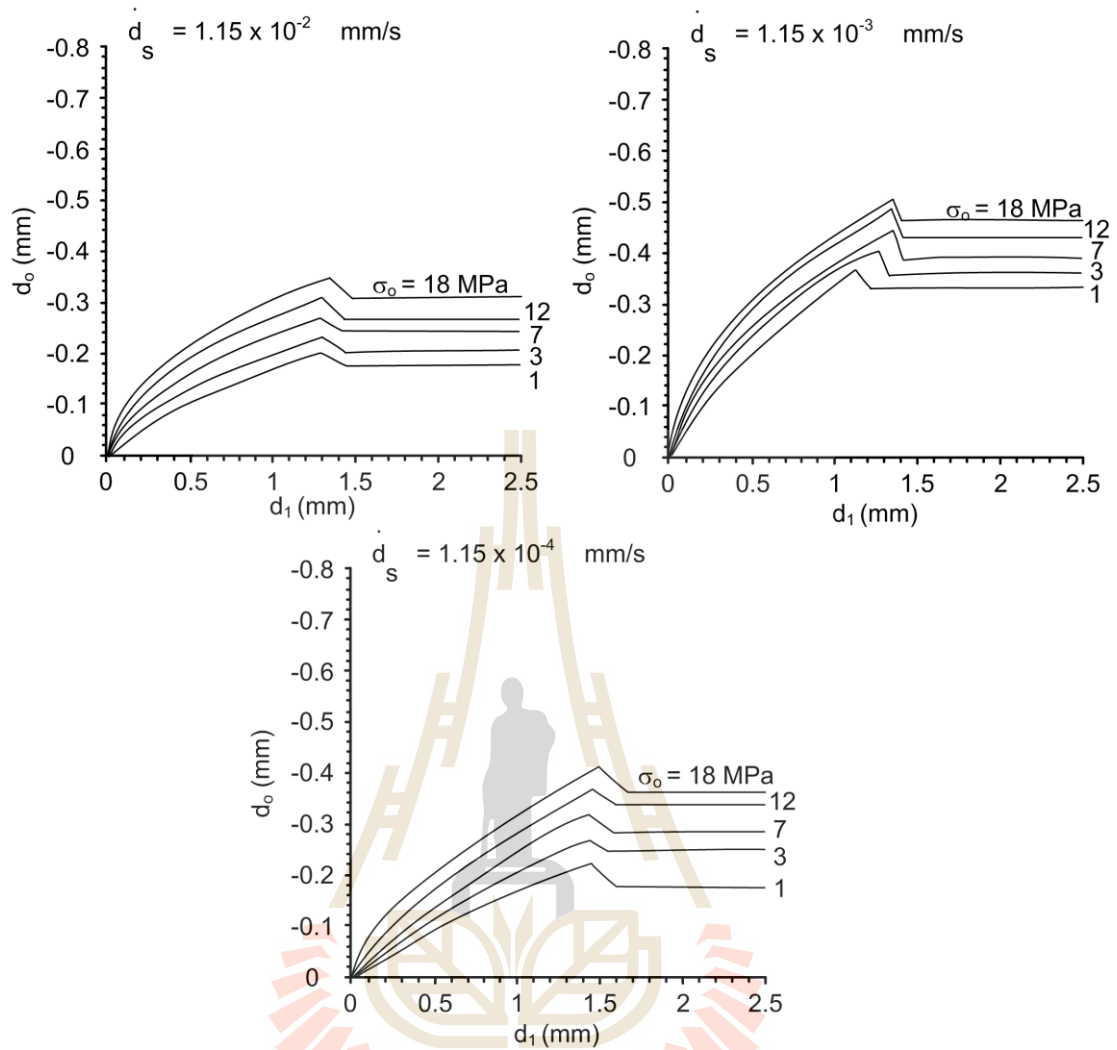
The shear and normal (dilation) displacements of the tested fractures can be calculated using Equations (5.1) and (5.2). Figures 5.13 through 5.14 shows the results in the form of  $d_n$ - $d_s$  diagrams. The dilations measured prior to and after the peak stresses notably decrease with the displacement velocity. Larger confining pressures also induce lower fracture dilations which agree with the test results obtained by Kleepmek et al., 2016.

Post-test fractures have been examined in attempt to qualitatively correlate the sheared-off areas with the shear velocity and temperature. The increases of confining stresses, temperature and the decrease of displacement velocities enhance the sheared-off areas. The post-test fractures are obscured by the deposition of the rock powder (gouges) resulting from the crushing of the asperities. Figure 5.15 plots the post-test JRC's as a function of  $\sigma_3$ . They support the previous observations that higher confining stresses and lower displacement velocities induce larger sheared-off areas. Figure 5.16 shows some examples of the post-test fractures, for the highest and lowest shear velocities and confining stresses for 303 and 473 kelvin. In the figure the light areas represent the sheared-off asperities with slight amount of gouge deposition. The post-test specimens have usually been broken around the edges. Obtaining the laser scan results along the same profile as that obtained before testing is virtually impossible. This makes more difficult by the relatively poor precision of the setting procedure of the available surface

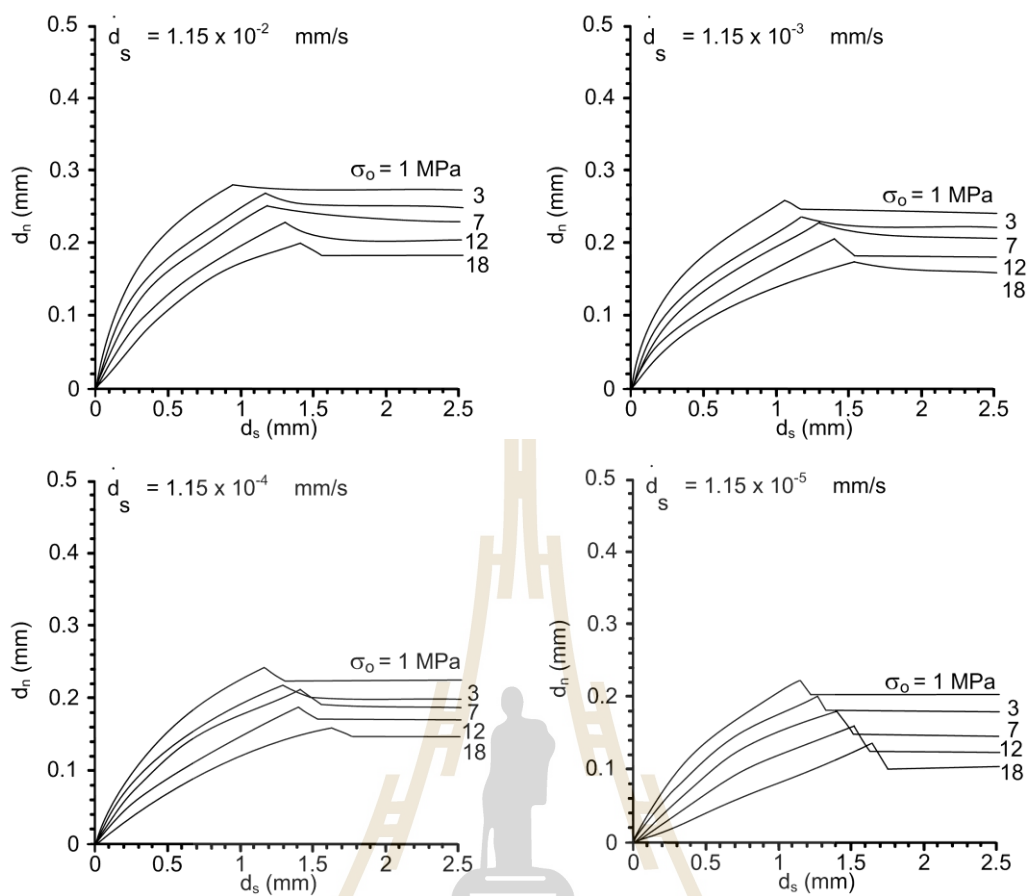
scanner. Nevertheless, some conclusions can be drawn. As expected, the increase of the confining stresses and temperature significantly increases the sheared-off areas.



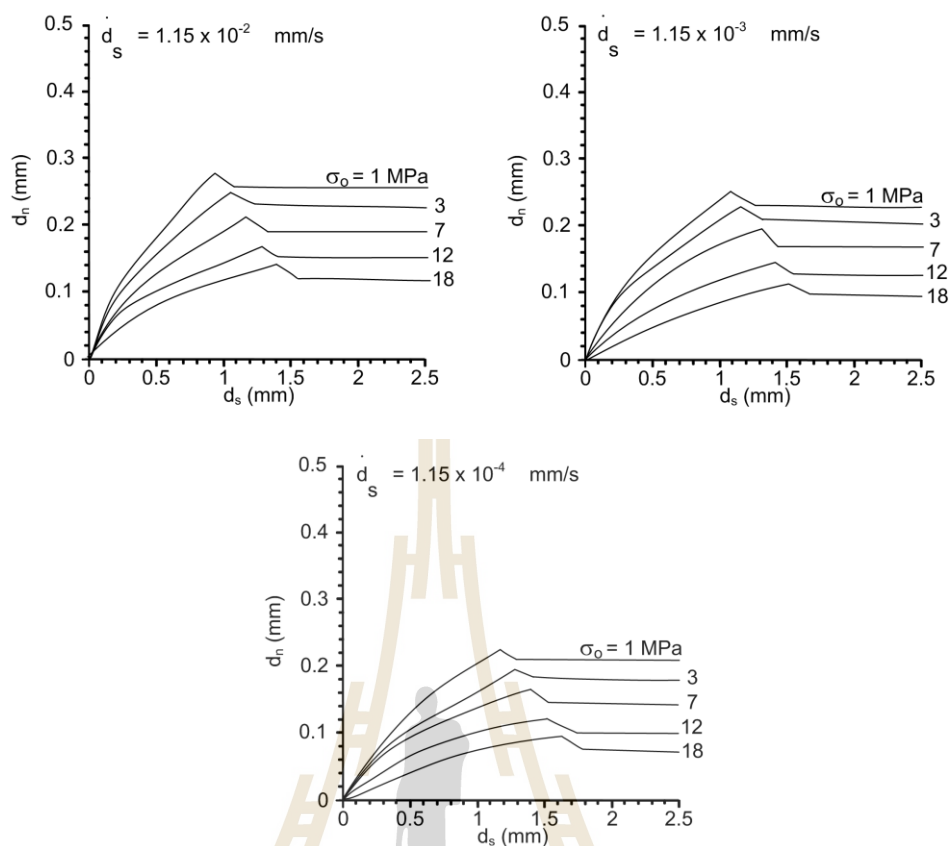
**Figure 5.11** Lateral-axial displacement ( $d_0-d_1$ ) curves of tension-induced fractures for 303 kelvin.



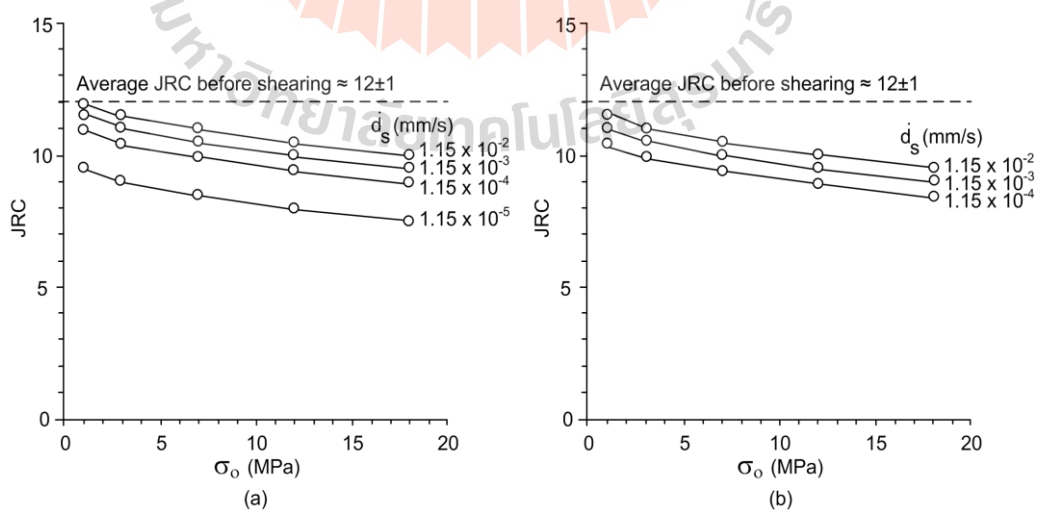
**Figure 5.12** Lateral-axial displacement ( $d_0-d_1$ ) curves of tension-induced fractures for 473 kelvin.



**Figure 5.13** Normal displacement ( $d_n$ ) as a function of the shear displacement ( $d_s$ ) for 303 kelvin.



**Figure 5.14** Normal displacement ( $d_n$ ) as a function of the shear displacement ( $d_s$ ) for 473 kelvin.



**Figure 5.15** Post-test JRC's as a function of  $\sigma_0$  for 303 kelvin (a) and 473 kelvin (b).





### 5.3 Triaxial shear tests on smooth saw-cut surfaces

For this test series the shear strengths of smooth saw-cut surfaces are determined under the confining pressures of 1, 7, and 12 MPa with shear velocity varying from  $1.15 \times 10^{-4}$  to  $1.15 \times 10^{-2}$  mm/s. The test results are obtained for  $\sigma_p/\sigma_o = 1.0$  with temperature equals to 473 kelvin. The test procedure and calculation method are identical to those of the tension-induced fractures. For the smooth saw-cut surface the Coulomb's criterion is used to represent the peak shear strengths under various shear velocities and confinements:

$$\tau = \sigma_n \cdot \tan (\phi^*) + c^* \quad (5.4)$$

where  $\phi^*$  and  $c^*$  are defined here as the apparent friction angle and apparent cohesion of the saw-cut surfaces. This is primarily to avoid confusing with the fracture cohesion ( $c$ ) and friction angle ( $\phi$ ) conventionally obtained from the direct shear test with constant normal stress. Tables 5.5 and 5.6 summarize the shear strength results of smooth saw-cut surfaces for 303 and 473 kelvin. The shear stress ( $\tau$ ) and normal stress ( $\sigma_n$ ) are calculated from the major principal ( $\sigma_1$ ) and confining ( $\sigma_0$ ) stresses, using Eqs. (4.1) and (4.2). The above equation (5.4) is fitted to the test results in the forms of  $\tau$ - $\sigma_n$  diagrams in Figure 5.15. The apparent basic friction angles are determined as  $30^\circ$ ,  $30^\circ$  and  $27^\circ$ , and the apparent cohesions are 1.54, 1.55 and 1.02. The diagrams suggest that the shearing resistances for the smooth surfaces tend to be independent of the shear velocities as evidenced by the similar values of  $\phi^*$  and  $c^*$  obtained under different shear velocities (Figure 5.17). In another word the effect of shear velocity on the fracture strength only pronounces on the rough fractures.

**Table 5.5** Summary of peak shear strengths and their corresponding normal stresses for smooth saw-cut surfaces at various  $\sigma_p/\sigma_o$ .

$\sigma_p/\sigma_o$	$\sigma_o$ (MPa)	$\sigma_1$ (MPa)	$\sigma_n$ (MPa)	$\tau$ (MPa)
0	1	8.84	2.96	3.39
	7	28.9	12.47	9.48
	12	40.8	19.2	12.47
1	1	7.65	2.66	2.88
	7	28.56	12.39	9.34
	12	39.78	18.95	12.03
2	1	6.8	2.45	2.51
	3	13.26	5.57	4.44
	7	25.5	11.63	8.01

**Table 5.6** Summary of peak shear strengths and their corresponding normal stresses for smooth saw-cut surfaces at various temperature.

$\dot{d}_s$ (mm/s)	$\sigma_3$ (MPa)	303 kelvin			473 kelvin		
		$\sigma_1$ (MPa)	$\sigma_n$ (MPa)	$\tau$ (MPa)	$\sigma_1$ (MPa)	$\sigma_n$ (MPa)	$\tau$ (MPa)
$1.15 \times 10^{-2}$	1	8.23	2.81	3.13	6.23	2.31	2.27
	7	30.28	12.82	10.08	24.47	11.37	7.56
	12	40.83	19.21	12.48	35.95	17.99	10.37
$1.15 \times 10^{-3}$	1	7.65	2.66	2.88	5.53	2.13	1.96
	7	28.54	12.39	9.33	22.75	10.94	6.82
	12	39.78	18.95	12.03	34.57	17.64	9.77
$1.15 \times 10^{-4}$	1	6.37	2.34	2.33	5.06	2.02	1.76
	7	26.24	11.81	8.33	20.66	10.42	5.92
	12	38.23	18.56	11.36	32.97	17.24	9.08

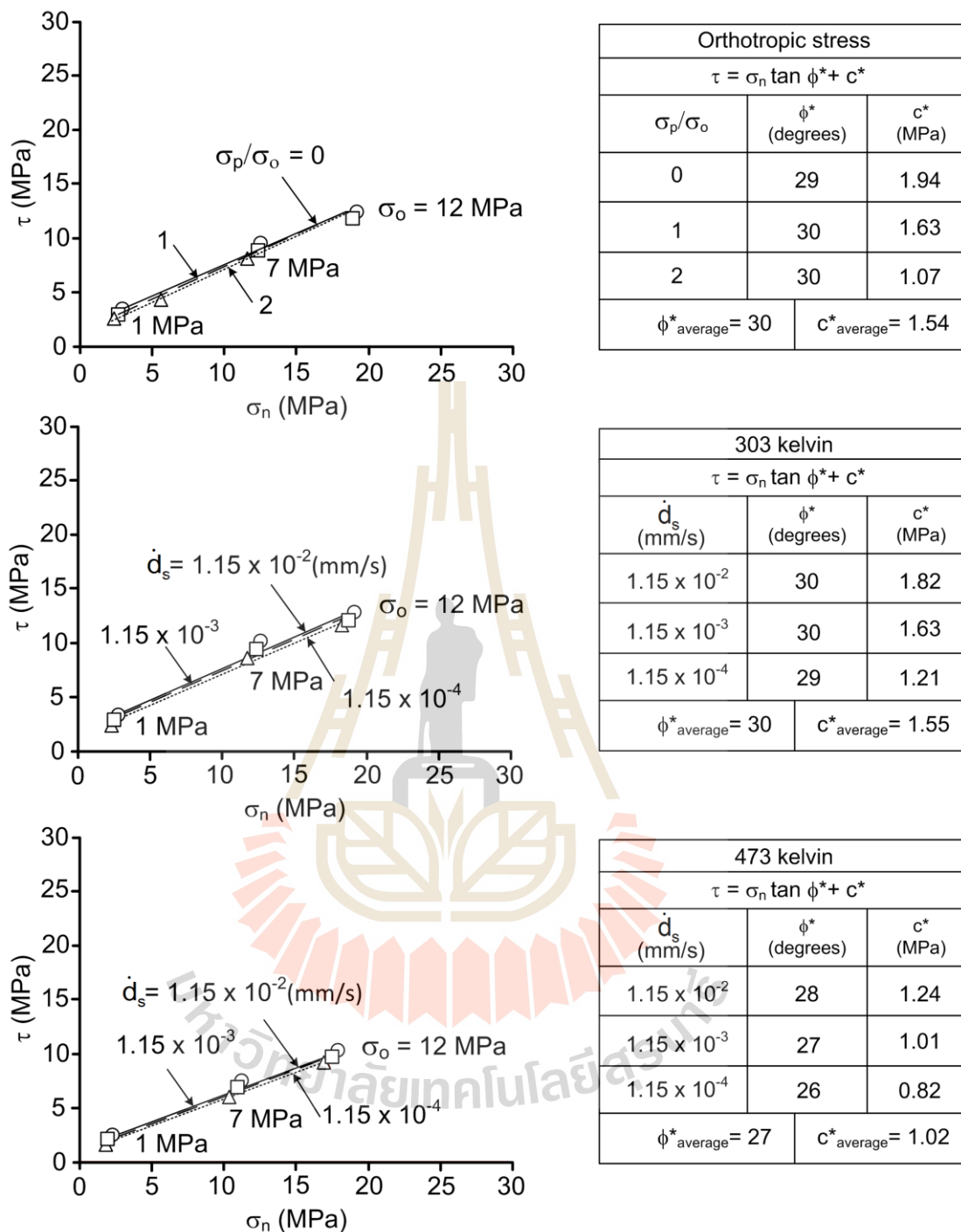


Figure 5.17 Shear strengths of smooth saw-cut surfaces.

# CHAPTER VI

## SHEAR STRENGTH CRITERIA

### 6.1 Introduction

An attempt has been made to derive strength criteria that can explicitly the effects of lateral stress ratios, normal stress, displacement velocity and temperature. Such criteria would be useful for the prediction of fracture shear strengths under the boundary conditions ( $\sigma_p/\sigma_o$ ,  $\sigma_3$  and  $\dot{d}_s$ ) beyond those used in this study. This chapter describes the normalization of the lateral stress ratios, shear displacement rate and temperature, derivative of the strength criteria for peak regions.

### 6.2 Empirical criterion under different $\sigma_p/\sigma_o$ ratios

An attempt is made here to develop an empirical strength criterion that can explicitly incorporate the effect of the lateral stress ratio and the normal stress. The power equation is proposed as follows:

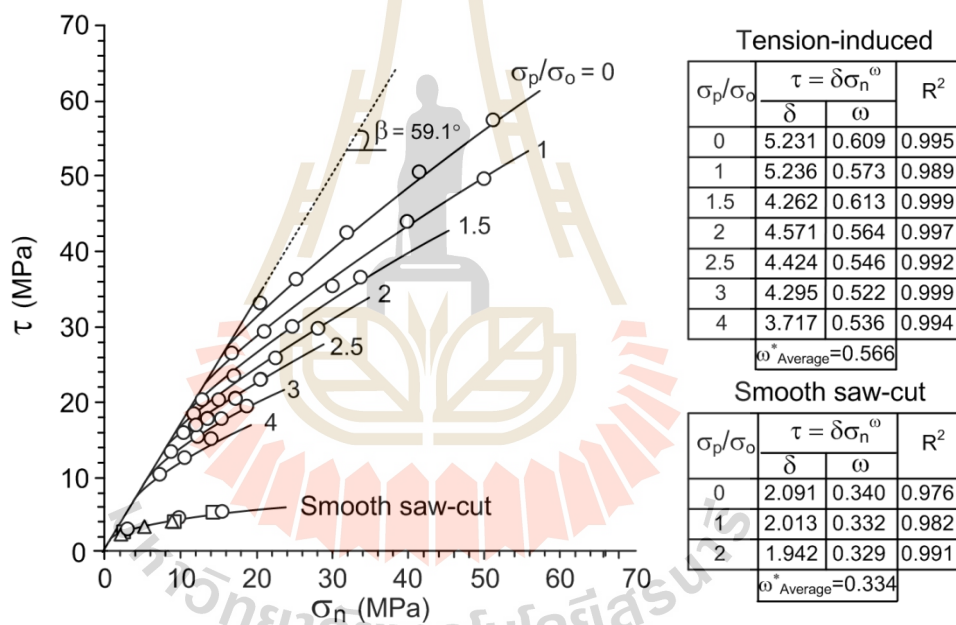
$$\tau = \delta \cdot \sigma_n^\omega \quad (6.1)$$

where  $\delta$  and  $\omega$  are empirical constants. The above equation is fitted to the experimental results in the forms of  $\tau$ - $\sigma_n$  diagrams in Figure 6.1. Non-linear behavior of the  $\tau$ - $\sigma_n$  relation is observed. Regression analysis of the test data by SPSS software (Colin & Paul, 2012) are performed on Equation (6.1) using the peak shear strength data given in Table 5.1. The parameter  $\omega$  can be defined as 0.566 and 0.334 for rough

and smooth surfaces. The parameter  $\delta$  decreases with increasing the stress ratios ( $\sigma_p/\sigma_o$ ), which can be described by a linear equation:

$$\delta = \psi - \eta \cdot (\sigma_p / \sigma_o) \quad (6.2)$$

where  $\psi$  and  $\eta$  are empirical constants. For the tension-induced (rough) fractures the parameters  $\psi$  and  $\eta$  are 5.274 and 0.370. For the saw-cut (smooth) fractures  $\psi$  and  $\eta$  are 2.090 and 0.075. Equations (6.1) and (6.2) fit well with the test results ( $R^2 > 0.9$ ).



**Figure 6.1** Shear strengths ( $\tau$ ) as a function of normal stress ( $\sigma_n$ ) for tension-induced fracture and smooth saw-cut surfaces.

### 6.3 Strain Energy Density Criterion under Lateral Stress Ratios

The activation energy has been widely used for the predictions of fault movements under great depth (high confining pressures) and elevated temperatures (Stesky, 1978; Ohnaka, 1995; Odedra, Ohnaka, Mochizuki, & Sammonds, 2001), where the fault dilation is neglected (i.e. plastic deformation of the shear zone). For shallow faults or fractures with low temperatures the lateral dilation of the fractures (brittle deformation) can not be ignored. An alternative approach is used here. The strain energy density principle is applied to describe the fracture strength and deformation under high confining pressures. The distortional strain energy ( $W_d$ ) required to displace the fractures can be defined as a function of mean strain energy ( $W_m$ ) as follows:

$$W_d = \zeta \cdot W_m \quad (6.3)$$

where  $\zeta$  is an empirical constant. The distortional and mean strain energies can be calculated from the test results as (Jaeger et al., 2007):

$$W_d = 3/2 \tau_{oct} \cdot \gamma_{oct} \quad (6.4)$$

$$W_m = 3/2 \sigma_m \cdot \varepsilon_m \quad (6.5)$$

where

$$\gamma_{oct} = (1/3) [2 (\varepsilon_{1,p} - \varepsilon_{o,p})^2]^{1/2} \quad (6.6)$$

$$\tau_{oct} = (1/3) [2 (\sigma_{1,p} - \sigma_o)^2]^{1/2} \quad (6.7)$$

$$\sigma_m = (\sigma_{1,p} + 2\sigma_o) / 3 \quad (6.8)$$

$$\varepsilon_m = (\varepsilon_{1,p} + \varepsilon_{o,p}) / 3 \quad (6.9)$$

Assuming that the intact portion of the specimen is rigid, the vertical and lateral strains can be determined from the fracture displacements:

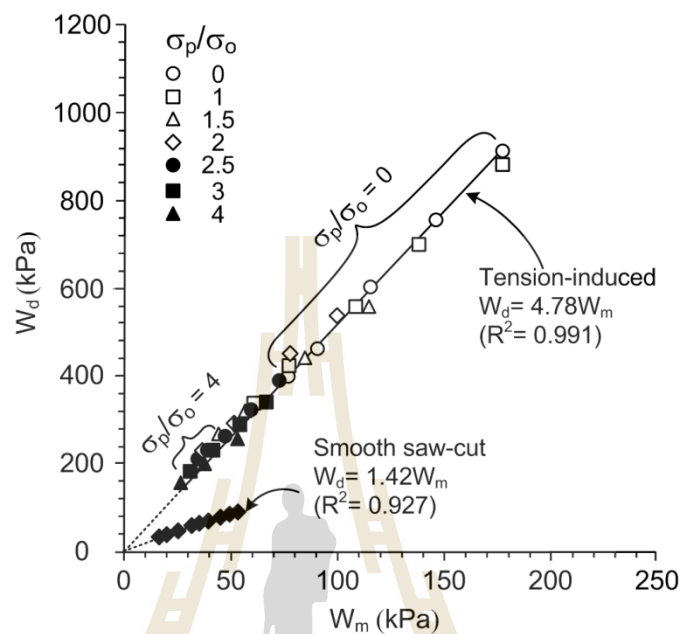
$$\varepsilon_{1,p} = d_{1,p} / L \quad (6.10)$$

$$\varepsilon_{o,p} = d_{o,p} / W \quad (6.11)$$

where  $d_{1,p}$  and  $d_{o,p}$  are the vertical and lateral displacements normal to the fracture strike,  $\varepsilon_{1,p}$  and  $\varepsilon_{o,p}$  are their vertical and lateral strains,  $L$  is the specimen length (87 mm), and  $W$  is the specimen width (50 mm). Table 6.1 gives the distortional and mean strain energy calculated for the rough and smooth fractures. Note that the strain that is parallel to the fracture strike is equal to zero because the test configurations (loading platens) do not allow lateral displacement in this direction.

Regression analysis of Equations (6.3) indicates that  $\delta$  equals to 4.78 for the rough fractures, and equals to 1.42 for the smooth fractures (Figure 6.2). The proposed criterion fit well to the test data with the correlation coefficient ( $R^2$ ) greater than 0.9. It implicitly incorporates the effects of stress ratio and confining pressure on the fractures. The  $W_d$  obtained from the rough fractures under high stress ratio is in the lower portion of the curve. The mean strain energy can be related to the depth of the fractures. The distortional strain energy represents the deviatoric stresses that cause the shear displacement. The ratios of  $W_d$  to  $W_m$  (or  $\delta$ ) are probably governed by the

roughness and strength of the fracture asperities. The  $W_d$ - $W_m$  curve of the smooth fractures would represent the lower bound of the energy required to shear the fractures.



**Figure 6.2** Distortional strain energy ( $W_d$ ) at peak shears strength as a function of mean strain energy ( $W_m$ ) for different  $\sigma_p/\sigma_o$  ratios.



**Table 6.1** Distortional and mean strain energy densities for different  $\sigma_p/\sigma_o$  ratios.

Fracture Types	$\sigma_p/\sigma_o$	$\sigma_p$ (MPa)	$\sigma_o$ (MPa)	$d_{1,p}$ (mm)	$d_{o,p}$ (mm)	$\epsilon_{1,p}$ (milli-strain)	$\epsilon_{o,p}$ (milli-strain)	$W_d$ (kPa)	$W_m$ (kPa)
Tension-Induced Fracture	0	0	1	1.09	-0.33	12.53	-6.58	405.53	78.05
		0	3	1.11	-0.34	12.76	-6.74	470.88	91.68
		0	7	1.20	-0.38	13.79	-7.58	613.22	116.44
		0	12	1.22	-0.39	14.02	-7.76	767.65	147.66
		0	18	1.26	-0.41	14.48	-8.10	925.54	179.41
	1	1	1	1.11	-0.36	12.76	-7.16	338.86	60.86
		3	3	1.18	-0.39	13.54	-7.78	420.07	78.05
		7	7	1.25	-0.43	14.37	-8.50	565.98	109.73
		12	12	1.35	-0.48	15.52	-9.56	707.63	139.59
		18	18	1.37	-0.49	15.75	-9.74	883.10	182.72
	1.5	1.5	1	1.13	-0.39	12.99	-7.82	263.17	43.69
		4.5	3	1.20	-0.43	13.79	-8.56	327.12	57.83
		10.5	7	1.28	-0.47	14.71	-9.38	439.86	85.33
		18	12	1.37	-0.52	15.75	-10.30	559.21	116.46
	2	2	1	1.15	-0.41	13.23	-8.12	235.62	37.63
		6	3	1.20	-0.43	13.79	-8.60	301.78	51.84
		14	7	1.32	-0.49	15.17	-9.90	453.05	79.42
		18	9	1.39	-0.53	16.02	-10.60	551.19	96.57
	2.5	2.5	1	1.15	-0.42	13.22	-8.30	218.35	34.08
		5	2	1.18	-0.43	13.56	-8.60	239.69	39.66
		7.5	3	1.24	-0.46	14.25	-9.20	272.76	46.24
		12.5	5	1.29	-0.49	14.83	-9.70	334.25	59.90
		17.5	7	1.33	-0.51	15.29	-10.10	397.50	73.81
	3	3	1	1.16	-0.43	13.38	-8.58	186.06	28.80
		9	3	1.25	-0.47	14.31	-9.40	234.82	41.10
		15	5	1.30	-0.49	14.94	-9.94	291.48	54.86
		21	7	1.34	-0.52	15.40	-10.36	343.35	67.75
	4	4	1	1.19	-0.45	13.68	-8.92	155.42	24.77
12		3	1.26	-0.48	14.43	-9.60	198.30	38.16	
20		5	1.34	-0.52	15.34	-10.40	258.68	53.72	
Smooth saw-cut surface	0	0	1	1.00	-0.05	11.49	-0.90	27.42	17.50
		0	7	1.02	-0.24	11.72	-4.80	46.28	35.58
		0	12	1.15	-0.36	13.22	-7.20	70.92	48.80
	1	1	1	1.27	-0.13	18.14	-2.60	42.00	24.56
		7	7	1.29	-0.36	14.83	-7.20	57.25	38.54
		12	12	1.37	-0.51	16.71	-10.20	85.78	51.84
	2	2	1	1.28	-0.14	14.71	-2.80	32.06	17.81
		6	3	1.30	-0.19	14.94	-3.80	43.29	31.03
		14	7	1.44	-0.38	16.55	-7.60	62.07	44.98

#### 6.4 Criterion for tension-induced fractures under various displacement velocities

The empirical shear strength criterion for fractures under high confining pressures proposed by Barton (1976) and Barton and Choubey (1977) cannot be applied to the test results obtained here because as the confining stresses increase the  $\tau$ - $\sigma_n$  relations for the three rock types tend to be non-linear. An alternative empirical criterion is proposed to represent the fracture shear strengths as a function of normal stress, as follows:

$$\tau = \alpha \cdot \sigma_n^\lambda \quad (6.12)$$

where  $\alpha$  and  $\lambda$  are empirical parameters, depending on rock types. Regression analyses are performed on Equation (6.12) using the peak shear strength data given in Table 5.3. Good correlations are obtained ( $R^2 \geq 0.9$ ). The parameters  $\alpha$  and  $\lambda$  determined for each shear velocity are summarized in Table 6.2. The parameter  $\alpha$  tends to be independent of the shear velocity. It probably relates to the fracture roughness. The parameter  $\alpha$  increases with shear velocity ( $\dot{d}_s$ ), which can be best represented by:

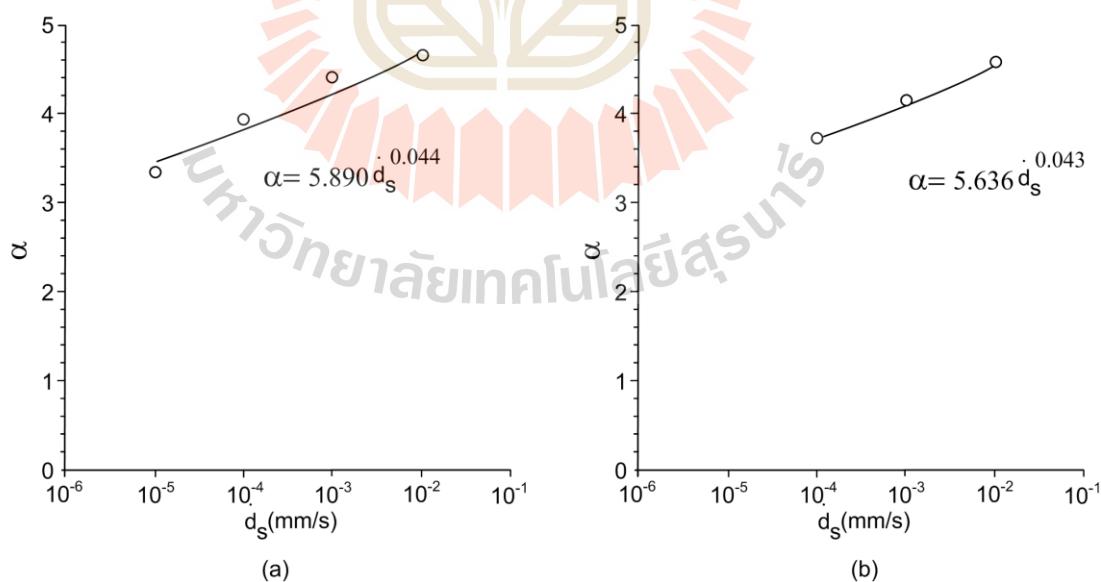
$$\alpha = \kappa \dot{d}_s^\beta \quad (6.13)$$

where  $\kappa$  and  $\beta$  are empirical constants. Their numerical values are given in Fig. 6.3. This means that  $\alpha$  is also dependent of fracture roughness, as evidenced by that's  $\alpha$  for the peak shear strengths at 303 kelvin are higher than those for the 473 kelvin. Substituting Equation (6.13) into Equation (6.12) the fracture shear strength criterion that considers the shear velocity effect is obtained. Figure 6.4 compares the proposed

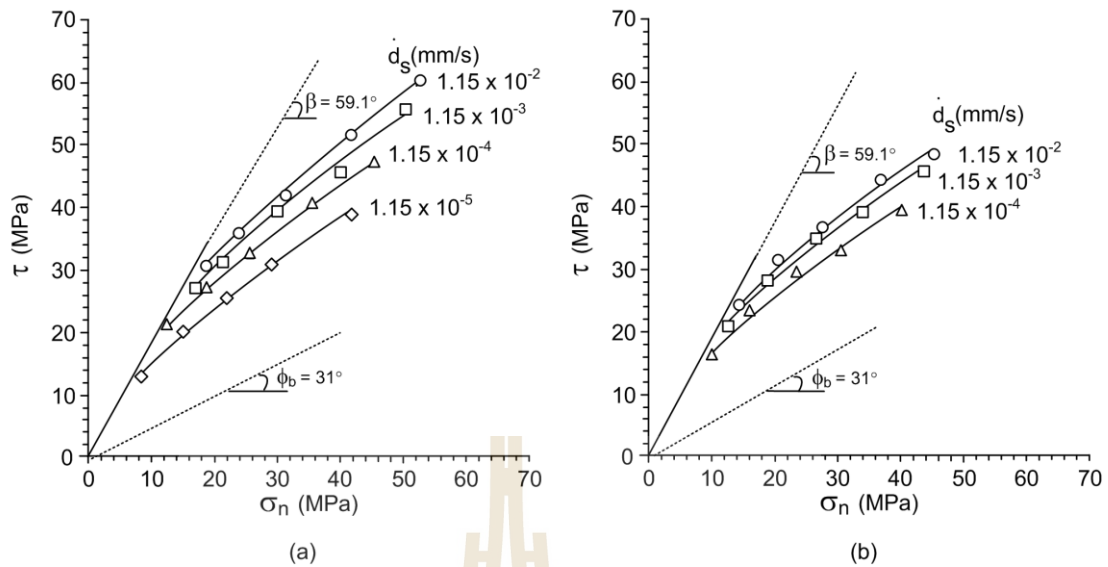
criterion with the peak shear strength results. The upper bound of the shear strengths is defined by the angle  $b$  which is maintained constant at  $59.1^\circ$ . The lower bound is defined by the basic friction angle ( $\phi_b$ ) obtained from the smooth saw-cut surfaces testing.

**Table 6.2** Parameters  $\alpha$  and  $\lambda$  for 303 kelvin and 473 kelvin

$\dot{d}_s$ (mm/s)	303 kelvin		473 kelvin	
	$\alpha$	$\lambda$	$\alpha$	$\lambda$
$1.15 \times 10^{-2}$	4.56	0.649	4.60	0.612
$1.15 \times 10^{-3}$	4.51	0.636	4.20	0.631
$1.15 \times 10^{-4}$	3.99	0.649	3.77	0.635
$1.15 \times 10^{-5}$	3.39	0.721	-	-



**Figure 6.3** Parameter  $\alpha$  as a function of shear velocity for 303 kelvin (a) and 473 kelvin (b).



**Figure 6.4** Proposed empirical criteria for peak shear strengths compared with test data for 303 kelvin (a) and 473 kelvin (b).

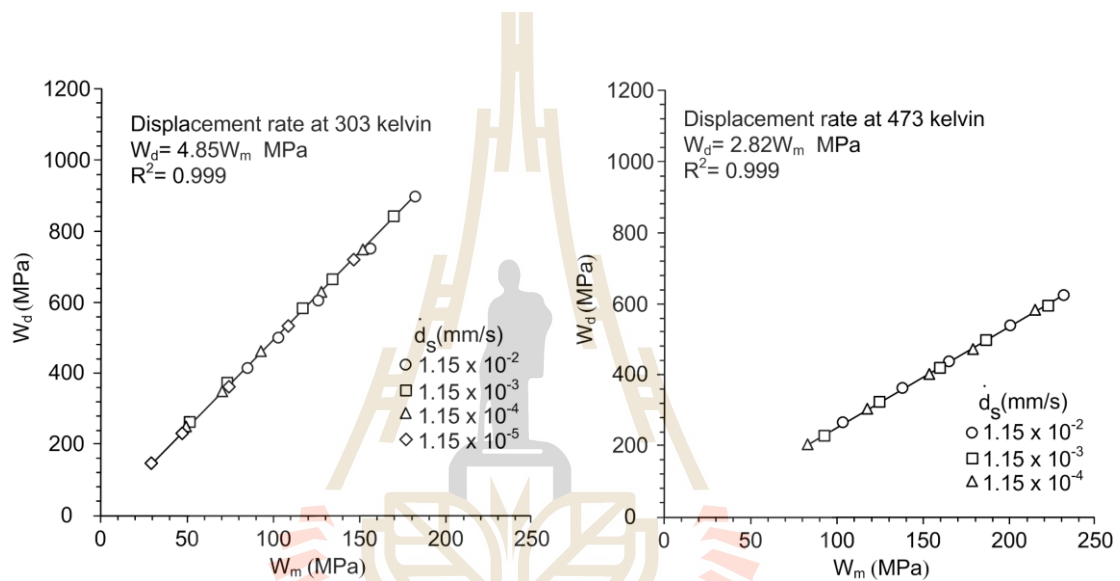
## 6.5 Strain Energy Density Criterion under various displacement velocities

The strain energy density principle is applied to describe the rock strength and deformation under triaxial shear tests. The distortional and mean strain energy at failure ( $W_d$ ,  $W_m$ ) can be calculated for each specimen, as follows:

$$W_d = \chi \cdot W_m \quad (6.14)$$

where  $\chi$  is an empirical constant. It is found that the distortional strain energy at dilation ( $W_d$ ) varies linearly with the mean strain energy ( $W_m$ ). Tables 6.3 and 6.4 gives the distortional and mean strain energy calculated for the rough surface at 303 and 473 kelvin.

Regression analysis of Equations (6.14) indicates that  $\chi$  equals to 4.85 for 303 kelvin, and equals to 2.82 for 473 kelvin (Figure 6.5). The proposed criterion fit well to the test data with the correlation coefficient ( $R^2$ ) greater than 0.9. It implicitly incorporates the effects of displacement velocity and confining pressure on the fractures. The  $W_d$  obtained from the rough fractures under high temperature is in the lower portion of the curve.



**Figure 6.5** Distortional strain energy ( $W_d$ ) at peak shears strength as a function of mean strain energy ( $W_m$ ) for 303 kelvin (a) and 473 kelvin (b).

**Table 6.3** . Distortional and mean strain energy densities for 303 kelvin.

$\dot{d}_s$ (mm/s)	$\sigma_o$ (MPa)	$d_{1,p}$ (mm)	$d_{0,p}$ (mm)	$\epsilon_{1,p}$ (milli-strain)	$\epsilon_{0,p}$ (milli-strain)	$W_d$ (kPa)	$W_m$ (kPa)
$1.15 \times 10^{-2}$	1	1.30	-0.40	14.94	-7.90	414.97	85.99
	3	1.31	-0.42	15.06	-8.30	499.34	103.45
	7	1.33	-0.44	15.29	-8.88	601.08	125.63
	12	1.33	-0.46	15.29	-9.26	749.51	155.60
	18	1.34	-0.48	15.40	-9.68	891.58	183.75
$1.15 \times 10^{-3}$	1	1.11	-0.36	12.76	-7.16	338.86	60.86
	3	1.18	-0.39	13.54	-7.78	420.07	78.05
	7	1.25	-0.43	14.37	-8.50	565.98	109.73
	12	1.35	-0.48	15.52	-9.56	707.63	139.59
	18	1.37	-0.49	15.75	-9.74	883.10	182.72
$1.15 \times 10^{-4}$	1	1.10	-0.33	12.64	-6.68	243.03	51.33
	3	1.20	-0.39	13.79	-7.84	349.97	71.23
	7	1.28	-0.45	14.71	-8.90	454.00	92.87
	12	1.39	-0.50	15.98	-10.02	624.75	128.81
	18	1.40	-0.53	16.09	-10.50	742.79	152.08
$1.15 \times 10^{-5}$	1	1.10	-0.36	12.64	-7.10	153.61	30.66
	3	1.10	-0.37	12.64	-7.32	240.86	49.57
	7	1.29	-0.46	14.83	-9.16	363.29	75.60
	12	1.46	-0.55	16.78	-10.90	537.45	109.66
	18	1.48	-0.56	17.01	-11.26	715.68	146.68



**Table 6.4** . Distortional and mean strain energy densities for 473 kelvin.

$\dot{d}_s$ (mm/s)	$\sigma_o$ (MPa)	$d_{1,p}$ (mm)	$d_{0,p}$ (mm)	$\varepsilon_{1,p}$ (milli-strain)	$\varepsilon_{0,p}$ (milli-strain)	$W_d$ (kPa)	$W_m$ (kPa)
$1.15 \times 10^{-2}$	1	1.27	-0.19	14.60	-3.80	268.83	104.14
	3	1.28	-0.22	14.71	-4.40	364.05	139.01
	7	1.28	-0.26	14.71	-5.20	438.32	165.85
	12	1.27	-0.29	14.60	-5.80	541.27	201.31
	18	1.31	-0.33	15.06	-6.60	625.60	232.21
$1.15 \times 10^{-3}$	1	1.26	-0.17	14.48	-3.40	226.65	93.15
	3	1.28	-0.22	14.70	-4.40	324.84	125.64
	7	1.29	-0.26	14.82	-5.24	420.03	160.48
	12	1.29	-0.30	14.83	-6.00	498.27	187.42
	18	1.31	-0.33	15.06	-6.60	590.58	223.47
$1.15 \times 10^{-4}$	1	1.44	-0.20	16.55	-4.00	202.02	83.30
	3	1.44	-0.26	16.55	-5.20	306.76	117.91
	7	1.45	-0.31	16.67	-6.20	403.82	153.89
	12	1.47	-0.36	16.90	-7.20	473.21	179.69
	18	1.48	-0.40	17.01	-8.00	584.31	216.05



# CHAPTER VII

## DISCUSSIONS, CONCLUSIONS AND RECOMMENDATIONS FOR FUTURE STUDIES

### 7.1 Discussions

This section discusses the key issues relevant to the reliability of the test schemes and the adequacies of the test results. Comparisons of the results and findings from this study with those obtained elsewhere under similar test conditions have also been made.

For the triaxial shear testing in this study, the angle  $\beta$  which is maintained constant at  $60^\circ$  seems to limit the lower ends of the  $\sigma_1$ - $\sigma_0$  curves and  $\tau$ - $\sigma_n$  curves for all test specimens (Figures 5.2 and 6.1). This angle is primarily set because it yields the length-to-width ratio of the block specimens of about 2.0. The block shape is most suitable for the polyaxial loading device. Larger angles might be produced in the longer block specimen and can not be installed in the available device. It is believed that if the angle is reduced to below  $45^\circ$  the shear sliding on the fractures may not occur, instead the compression failure of the intact rock wedge would taken place. In principle, the angle  $\beta$  should not affect the  $\sigma_1$ - $\sigma_0$  or  $\tau$ - $\sigma_n$  relations.

As evidenced by the good correlation coefficients obtained from the proposed empirical strength equation (Figure 6.1), the test results of lateral stress ratio are believed to be highly reliable. This is true for all test series: triaxial shear test results on rough and smooth fractures. The results obtained here agree reasonably will with



Naphudsua and Fuenkajorn (2014) who conducted the triaxial shear test of fractures in Tak granite sample, and Kapang et al. (2013) who conducted the test on fractures in sandstone.

Figure 5.5 shows the fracture dilation (normal displacement,  $d_n$ ) as a function of the shear displacement ( $d_s$ ) monitored during the test. The stress ratios also decrease the fracture dilation at the peak stress. Under the some  $\sigma_o$ , the fractures dilation at the peak strength decreases with increasing lateral stress ratios. In general this agrees with the test results obtained by Kapang et al. (2013). This may be caused by the lateral stress concentrations at the fracture asperities, and hence makes them fail more easily comparing to the lower stress ratio.

It is however not intention here to claim that the proposed empirical form (Equation 6.1) of the peak shear strength criterion is universally applicable and all fracture characteristics. Different forms of the mathematical relation may be suitable for all test series. The proposed equation however has obvious advantage that it can represent the fracture shear strengths under lateral stress ratios, various shear velocities and temperature. In this low confinement region, based on the proposed criterion, the peak shear strength is highly sensitive to the normal stresses. The discrepancy could be minimized or eliminated if more test data in this region are available. In practice, however, due to the limitation of the available polyaxial loading device, obtaining the confining stress  $\sigma_3$  lower than 1 MPa is not possible. The test data under large confinements up to 21 MPa seem adequate and uniformly distributed.

For the shear velocity and temperature testing, an assessment of the effect of the degrees of the fracture roughness on the response to the shear velocity can not be made. Only one degree of roughness (JRC) is obtained from the tension-inducing

method. Nevertheless, the research findings clearly indicate that the rougher the fracture surface the more effect from the shear velocity and temperature is pronounced. This is also evidenced by the shear strength of the smooth saw-cut surfaces is independent of the shear velocity and temperature (Figure 6.4).

The shear and normal (dilation) displacements of the tested fractures can be calculated using Equations (5.1) and (5.2). Figures 5.13 and 5.14 show the results in the form of  $d_n$ - $d_s$  diagrams. The dilations measured prior to and after the peak stresses notably decrease with the displacement velocity. Larger confining pressures also induce lower fracture dilations which agree with the test results obtained by Klepemek et al., (2016).

It is invoked by the test results that fracture roughness is a factor that is coupled with the shear velocity and temperature effect. The shear strengths of smooth fracture tend to be independent of the shear velocity and temperature. The rougher fracture surfaces, the greater effect from the shear velocity and temperature. Since the degree of roughness is limited to only one tested here, it would be desirable to obtain shear strengths under the same shear velocity but different degrees of roughness or JRC values. This task would be very difficult to accomplish because fracture roughness obtained by tension-inducing method can not be controlled by test procedure. They are rather controlled by petrographic characteristics of the rock (e.g. crystal, mineral composition, texture, etc.). It should be also noted that comparison of the fracture shear strengths that are obtained with different JRC values may not be strictly valid as they may pose different joint wall strengths and shearing mechanisms.

## 7.2 Conclusions

All objectives and requirements of this study have been met. The results of the laboratory testing and analyses can be concluded as follows:

- (1) The effect of lateral stress ratios can be observed from  $\sigma_1$ - $\sigma_0$  and  $\tau$ - $\sigma_n$  diagrams. The shearing resistance, dilation and areas of sheared-off asperities of the rough fractures decrease when the lateral stress ratios increase. The shear strengths of smooth saw-cut surfaces tend to be independent of the stress ratios (see Figure 5.3 and Tables 5.1).
- (2) The fractures dilation at the peak strength decreases with increasing lateral stress ratios (see Figure 5.5).
- (3) The areas of the sheared-off asperities increase with the confining pressure, as evidenced by the lower JRC values measured from the post-test fractures (see Figure 5.6 and Table 5.2).
- (4) The effects of the stress ratio and confining pressure on the shear strengths of the rough fractures can be well described by a power equation (Equation (6.1)). The equation can be used as a strength criterion to determine the stability of engineering structures near ground surface (e.g., foundations, slope embankments and tunnels) where the applied shear and normal stresses and stress ratio are known.
- (5) The distortional and mean strain energy densities are calculated from the test results. Their linear relation has implicitly incorporated the effects of lateral stress ratio and confining pressure (Figure 6.2).
- (6) The effect of shear velocity and temperature can be observed from  $\sigma_1$ - $\sigma_0$  and  $\tau$ - $\sigma_n$  diagrams. The lower shear velocity is applied, the lower peak shear strengths are obtained. The shear strengths decrease proportionally with the decrease

of the order of the shear velocity and decrease with increasing the temperature (see Figure 5.10 and Tables 5.3 and 5.4).

(7) The fractures with larger JRC values tend to be more sensitive to the shear velocity and temperature than those with lower JRC values (Figure 5.9). The shear strength of the smooth saw-cut surfaces is independent of the shear velocity (Figure 5.17).

(8) The fracture dilations measured prior to and after the peak strengths significantly decrease with increasing the confining pressures and decreasing the shear velocities and decrease with increasing the temperature (Figures 5.13 and 5.14).

(9) The behavior of the fracture dilations above are supported by the post-test observations on the shear fractures that the reduction of the shear velocity notably increases the sheared-off areas on the fractures, particularly when the fractures are subject to high confining stresses (see Figure 5.12).

(10) The distortional and mean strain energy densities are calculated from the test results. Their linear relation has implicitly incorporated the effects of lateral stress ratio and confining pressure (Figure 6.2). The  $W_d$ - $W_m$  curve of rough fractures is steeper than that of the smooth fracture, suggestion that lower strain energy is required to displace the rough fractures than the smooth ones.

### **7.3 Recommendations for future studies**

Recognizing that the numbers of the specimens and the test parameters used here are relatively limited, more testing and measurements are recommended, as follows:

(1) The fracture areas used in this study ( $100 \times 50 \text{ mm}^2$ ) are relatively small even though they are well complied with the relevant standard practice and internationally suggested method. Testing on larger fracture areas would provide a more representative of the shear strength results when they are applied to the actual fractures under in-situ condition. The scale effect on the fracture shear strengths has also been addressed by Braton and Bandis (1980).

(2) The effects of the shear velocity would be more rigorously determined and its criterion be more accurately calibrated if lower shear displacement velocities are applied, i.e., one or two orders of magnitude lower than those used in this study. This results in the test period of 2 days. The shear velocity with two orders of magnitude lower than this would take about 200 days (equivalent to 3.6 mm/year) to complete one fracture specimen. This would require special measurement device to monitor the displacements under such long period of testing. The results can however be a great benefit because the displacement velocity is similar to those of the actual fault movement in the north of Thailand (about 1 mm/year) (Fenton et al., 2003).

(3) Increasing the number of the specimens would statistically enhance the reliability of the test results and the predictability of the proposed strength criterion.

(4) A high precision laser scanner system may be needed to obtain the fracture profiles prior to and after shearing (preferable in 3-dimension). Care however should be taken to ensure that the line scanning in 2-dimension or the 3-dimensional images of the fractures prior to and after shearing can be precisely overlain to examine the alteration of the fracture surfaces due to shearing under various conditions.

## REFERENCES

- Alexeev, A. D., Revva, V. N., Bachurin, L. L., and Prokhorov, I. Y. (2008). The effect of stress state factor on fracture of sandstones under true triaxial loading. **International Journal of Fracture**. 149(1): 1-10.
- AlTammar, M. J., Sharma, M. M., and Manchanda, R. (2018). The Effect of Pore Pressure on Hydraulic Fracture Growth: An Experimental Study. **Rock Mechanics and Rock Engineering**. pp.1-24.
- Alvarez, R., Reynoso, J. P., Alvarez, L. J., and Martinez, M. L. (1978). Electrical conductivity of igneous rocks: composition and temperature relations. **Bulletin Volcanologique**. 41(4):317–327.
- Barton, N. (1976). The Shear strength of rock and rock joint. **International Journal of Rock Mechanics and Mining Sciences and Geomechanics Abstracts**.13(9): 255-279.
- Barton, N. (1982). Characterizing rock masses to improve excavation design. Panel Report. Theme II Tunnelling and Excavation. **Proceeding of 4<sup>th</sup> Congress international Association for Engineering Geology and Environment**. New Delhi.
- Barton, N. and Bandis, S. (1980). Some effects of scale on shear strength of rock joints. **International Journal of Mechanics and Mining Sciences and Geomechanics Abstracts**. 17(1): 69-73.

- Barton, N. and Choubey, V. (1977). The shear strength of rock joints in theory and practice. **International Journal of Rock Mechanics and Mining Sciences and Geomechanics Abstracts**. 10(1-2): 1-54.
- Barton, N. R. (1973). Review of a new shear strength criterion for rock joint deformation. **Engineering Geology**. 7: 287-332.
- Berumen, S. and Tiab, D. (1996). Effect of pore pressure on conductivity and permeability of fractured rocks. In **SPE Western Regional Meeting**. Society of Petroleum Engineers.
- Blanpied, M. L., Lockner, D. A., and Byerlee, J. D. (1995). Frictional slip of granite at hydrothermal conditions. **Journal of Geophysical**. 100(B7): 13,045-13,064.
- Brady, B. H. G. and Brown, E. T. (2006). **Rock mechanics for underground mining**. thirded. Springer, Netherlands.
- Cai, M. (2008). Influence of intermediate principal stress on rock fracturing and strength near excavation boundaries-insight from numerical modeling. **International Journal of rock Mechanics and Mining Sciences**. 45: 763-772.
- Charusiri, P., Rhodes, B. P., Saithong, P., Kosuwan, S., Pailopli, S., Wiwegwin, V. D., Hinthong, C., and Klaipongpan, S. (2007). Regional Tectonic Setting and Seismicity of Thailand with Reference to Reservoir Construction. In **proceeding of Geothai 07 international conference on geology of Thailand: towards sustainable development and sufficiency economy**. Bangkok, Thailand.
- Charusiri, P., Kosuwan, S., Lumjuan, S., and Wechbunthung, B. (1999). Review of active faults and seismicity in Thailand. **Ninth regional congress on geology, mineral and energy resources of southeast Asia 98<sup>th</sup>**. Kuala Lumpur, Malaysia.



- Charusiri, P., Kosuwan, S., Saithong, P., Khaowiset, K., Pananont, P., Thitimakorn, T., and Pailoplee, S. (2011). Active fault study in Kanchanaburi province, Western Thailand. **In Technical report, Thailand Research Fund.** Bangkok, Thailand.
- Colin, D. G. and Paul, R. K. (2012). **IBM SPSS statistics 19 made simple.** Psychology Press, New York.
- Colmenares, L. B. and Zoback, M. D. (2002). A statistical evaluation of intact rock failure criteria constrained by polyaxial test data for five different rocks. **International Journal of Rock Mechanics and Mining Sciences.** 39: 695-729.
- Crawford, A. M. and Currant, J. H. (1981). The influence of shear velocity on the frictional resistance of rock discontinuities. **International Journal of Rock Mechanics and Mining Sciences and Geomechanics Abstracts.**18(6): 505-515.
- Curran, J. H. and Leong, P. K. (1983). Influence of shear velocity on rock joint strength. In: **Proceeding of 5<sup>th</sup> ISRM Congress. International Society for Rock Mechanics.** Melbourne, Australia, A235-A240.
- Dwivedi, R. D., Goel, R. K., Prasad, V. V. R., and Sinha, A. (2008). Thermo-mechanical properties of Indian and other granites. **International Journal of Rock Mechanics and Mining Sciences.** 45(3): 303-315.
- Fenton, C. H., Charusiri, P., and Wood, S. P. (2003). Recent paleoseismic investigations in Northeast and Western Thailand. **Annals of Geophysics.**46(5): 957-981.
- Fuenkajorn, K. and Kenkhuntod, N. (2010). Influence of loading rate on deformability and compressive strength of three Thai sandstones. **Geotechnical and Geological Engineering.** 28: 707-715.
- Fuenkajorn, K. and Naphusa, P. (2014). Effect of temperatures on shear strength of fractures in granite. **The Journal of KMUTNB.** 24(2): 298-307.



- Fuenkajorn, K., Sriapai, T., and Samsri, P. (2012). Effect of loading rate on strength and deformability of Maha Sarakham salt. **Engineering Geology**. pp. 135-136.
- Grasselli, G. and Egger, P. (2003). Constitutive law for the shear strength of rock joints based on three-dimensional surface parameters. **International Journal of Rock Mechanics and Mining Sciences**. 40 (1): 25-40.
- Haimson, B. (2006). True triaxial stresses and brittle fracture of rock. **Pure and Applied Geophysics**. 163: 1101-1113.
- Haimson, B. and Chang, C. (2000). A new true triaxial cell for testing mechanical properties of rock and its use to determine rock strength and deformability of Westerly granite. **International Journal of Rock Mechanics and Mining Sciences**. 37(1-2): 285-296.
- Haimson, B. and Rudnicki, J. W. (2010). The effect of the intermediate principal stress on fault formation and fault angle in siltstone. **Journal of Structural Geology**. 32(11): 1701-1711.
- Hinthong, C. (1995). The study of active faults in Thailand. Technical. **Conference Progression and vision of Mineral Resources Development (Department of Mineral Resources)**. Bangkok, Thailand, pp. 129-140.
- Hou, P., Gao, F., Gao, Y., Yang, Y., and Cai, C. (2017). Effect of pore pressure distribution on fracture behavior of sandstone in nitrogen fracturing. **Energy Exploration and Exploitation**. 35(5): 609-626.
- Jaeger, J. C., Cook, N. G. W., and Zimmerman, R.W. (2007). **Fundamentals of rock mechanics**. Fourth ed. Blackwell Publishing, Malden, USA.

- Johansson, F. and Stille, H. A. (2014). A conceptual model for the peak shear strength of fresh and unweathered rock joints. **International Journal of Rock Mechanics and Mining Sciences**. 69:31–38.
- Kamonphet, T. and Fuenkajorn, K. (2013). Effect of cyclic loading on fracture shear strength. In **Proceeding of the Fourth Thailand Symposium on Rock Mechanics**, January 24-25, 2013, Im Poo Hill Resort, Nakhon Ratchasima, Thailand, Published by Geomechanics Research Unit, Suranaree University of Technology, Nakhon Ratchasima.
- Kapang, P., Walsri, C., Sriapai, T., and Fuenkajorn, K. (2013). Shear strengths of sandstone fractures under true triaxial stresses. **Journal of Structural Geology**. 48: 57-71.
- Kato, A., Ohnaka, M., Yoshida, S., and Mochizuki, H. (2003). Effect of strain rate on constitutive properties for the shear failure of intact granite in seismogenic environment. **Geophysical research letters**. 30(21): 1-4.
- Kawamoto, E. and Shimamoto, T. (1998). The strength profile for biminerale shear zones: an insight from high-temperature shearing experiments on calcite–halite mixtures. **Tectonophysics**. 295(1–2): 1-14.
- Kemeny, L. (2003). The time-dependent reduction of sliding cohesion due to Rock bridges along discontinuities: a fracture mechanics Approach. **Rock Mechanics and Rock Engineering**. 36(1): 27-38.
- Kemthong, R. and Fuenkajorn, K. (2007). Prediction of joint shear strengths of ten rock types using field-identified parameters. **Rock Mechanics Proceedings of First Thailand Symposium**. Nakhon Ratchasima, Thailand. pp. 195-209.

- Klempmek, M. and Fuenkajorn, K. (2015). Strengths of rock fractures as affected by shear velocities and confinements. **Vietrock 2015 an ISRM specialized conference**. Hanoi, Vietnam, March 12-13.
- Klempmek, M., Khamrat, S., Thongprapa, T., and Fuenkajorn, K. (2016). Displacement velocity effects on rock fracture shear strengths. **Journal of Structural Geology**. 90: 48-60.
- Lane, K. S. and Heck, W. J. (1964). Triaxial testing for strength of rock joints. **Proceedings of the 6<sup>th</sup> U.S. Symposium on Rock Mechanics (USRMS)**. October 28-30, Rolla, Missouri, pp. 98-108.
- Li, B., Jiang, Y., and Wang, G. (2012a). Evaluation of shear velocity dependency of rock fractures by using repeated shear tests. **Proceeding of 12<sup>th</sup> ISRM Congress, Harmonising Rock Engineering and the Environmental**. Beijing, China, pp. 699-702.
- Li, C., Zhang, Q., Wang, S., Jia, D., Zhang, D., Zhang, Y., and Zhang, X. (2015). Useful fluid flow and flow rate in grinding: an experimental verification. **The International Journal of Advanced Manufacturing Technology**. 81(5): 785-794.
- Li, Y., Wang, J., Jung, W., and Ghassemi, A. (2012b). Mechanical properties of intact rock and fracture in welded tuff from Newberry volcano. **Proceeding of Thirty-seventh Workshop on Geothermal Reservoir Engineering**. Stanford University, Stanford, California.
- LianYing, Z., XianBiao, and AiHong, L. (2009). Experimental study on the mechanical properties of rocks at high temperature. **Science in China Series E: Technological Sciences**. 52(3):641-646.

- Mahawat, C., Atherton, M.P., and Brotherton, M.S. (1990). The Tak Batholith, Thailand: the evolution of contrasting granite types and implications for tectonic setting. **Journal of Southeast Asian Earth Sciences**. 4: 11-27.
- Masri, M., Sibai, M., Shao, J.F., and Mainguy, M. (2014). Experimental investigation of the effect of temperature on the mechanical behavior of Tournemire shale. **International Journal of Rock Mechanics and Mining Sciences**. 70: 185-191.
- Mitchell, E. K., Fialko, Y., and Brown, K. M. (2013). Temperature dependence of frictional healing of Westerly granite: Experimental observations and numerical simulations. *Geochemistry, Geophysics, Geosystems* 14: 567-582.
- Morris, A.P. and Ferrill, D.A. (2009). The importance of the effective intermediate principal stress  $\sigma_2$  to fault slip patterns. **Journal of Structural Geology**. 31(9): 950-959.
- Mostafa, M. S., Gaber, N. A. A., and Abozid, E.F. (2003). Electrical Resistivity of some Basalt and Granite Samples From Egypt. **Egypt. J.Sol.** 26(1): 25-32.
- Muralha, J., Grasselli, G., Tatone, B., Blumel, M., Chryssanthakis, P., and Yujing, Y. (2013). ISRM Suggested Method for Laboratory Determination of the Shear Strength of Rock Joints: Revised Version. **Rock Mechanics and Rock Engineering**. DOI 10.1007/s00603-013-0519-z.
- Naphudsa, P. and Fuenkajorn, K. (2014). Thermal effects on shearing resistance of fractures in granite. **Proceeding of the Conference on Advances in Civil Engineering for Sustainable Development**, 27-29 August 2014, Thailand.
- Naphudsa, P., Tepnarong, P., and Fuenkajorn, K. (2013). Effect of elevated temperatures on shear strength of fractures in granite. **Proceeding of the EIT-JSCE Joint International Symposium on International Human Resource Development**

**for Disaster-Resilient Countries 2013**. September 12-13, Imperial Queen's Park Hotel, Bangkok, Thailand.

Nordeng, S. H. (2012). Basic geochemical evaluation of unconventional resource plays. Geo News Newsletter, Department of Mineral Resources, North Dakota.

**Geological Survey**. 39(1): 14-17.

Odedra, A., Ohnaka, M., Mochizuki, H., and Sammonds, P. (2001). Temperature and pore pressure effects on the shear strength of granite in the brittle-plastic transition regime. **Geophysical Research Letters**. 28(15): 3011-3014.

Ohnaka, M. (1995). A shear failure strength law of rock in the brittle-plastic transition regime. **Geophysical Research Letters**. 22 (1): 25-28.

Pongsapich, W. and Mahawat, C. (1977). Some aspects of Tak Granites, northern Thailand. **Geol.Soc. Malaysia, Bulletin**. pp. 175-186.

Rajaram, V. (1981). Mechanical Behavior of Granite Under Cyclic Compression. **International Conferences on Recent Advances in Geotechnical Earthquake Engineering and Soil Dynamics**. Apr 26<sup>th</sup> - May 3<sup>rd</sup>.

Ramamurthy, T. and Arora, V.K. (1994). Strength predictions for jointed rocks in confined and unconfined states. **International Journal of Mechanics and Mining Sciences and Geomechanics Abstracts**. 31(1): 9-22.

Rodklang, K., Khamrat, S., and Fuenkajorn, K. (2015). Effects of temperatures on strength and deformability of Tak granite. **KKU Research Journal**. 20(3): 272-284.

Rosso, R. S. (1976). A comparison of joint stiffness measurement in direct shear, triaxial compression, and in situ. **International Journal of Rock Mechanics and Mining Sciences and Geomechanics Abstracts**. 13(6): 167-172.

- Saithong, P. (2006). Characteristics of the Moei-Mae Ping Fault Zone, Changwat Tak, northwestern Thailand. **M.Sc. thesis**, Department of Geology, Chulalongkorn University, Thailand.
- Saithong, P., Kosuwan, S., Won-in, K., Takashima, I., and Charusiri, P. (2005). Late Quaternary paleoseismic history and surface rupture characteristics of the Moei-Mae Ping Fault Zone in Tak area, northwestern Thailand. **Proceeding International Conference Geology, Geotechnology and Mineral Resources of INDOCHINA**, November 28-30 Khon Kaen, Thailand, pp.511-516.
- Shao, S., Ranjith, P. G., Wasantha, P. L. P., and Chen, B. K. (2015). Experimental and numerical studies on the mechanical behavior of Australian Strathbogie granite at high temperatures: An application to geothermal energy. **Geothermics**. 54: 96-108.
- Shimada, M. and Liu, J. (2000). Temperature dependence of strength of rocks under high confining pressure. **Annals of Disaster Prevention Research Institute**. 43:75-84.
- Stesky, R. M. (1975). The mechanical behaviour of faulted rock at high temperature and pressure. **Thesis doctor of Massachusetts Institute of Technology**.
- Stesky, R. M. (1978). Rock friction-effect of confining pressure, temperature, and pore pressure. **Pure and Applied Geophysics**. 116 (4): 690-704.
- Stesky, R. M., Brace, W. F., Riley, D. K., and Robin, P. Y. F. (1974). Friction in faulted rock at high temperature and pressure. **Tectonophysics**. 23: 177-203.
- Tisa, Z. Y. and Kovari, K., (1984). Continuous failure state direct shear tests. **Rock Mechanics and Rock Engineering**. 17: 83-95.

- Wendai, L. (2000). Regression analysis, linear regression and probit regression. In 13 chapters. **SPSS for windows: statistical analysis**. Publishing House of Electronics Industry. Beijing.
- Xu, X., Kang, Z., Ming, j., Ge, W., and Jing, C. (2009). Research of microcosmic mechanism of brittle-plastic transition for granite under high temperature. **Procedia Earth and Planetary Science**. 1(1): 432-437.
- Zhao, J. (1997a). Joint surface matching and shear strength, Part A: joint matching coefficient (JMC). **International Journal of Rock Mechanics and Mining Sciences**. 34(2): 173-178.
- Zhao, J. (1997b). Joint surface matching and shear strength, Part B: JRC-JMC shear strength criterion. **International Journal of Rock Mechanics and Mining Sciences**. 34(2): 179-185.

## **BIOGRAPHY**

Miss. Pajeeraporn Weingchanda was born on September 27, 1984 in Khonkean province, Thailand. She received her Bachelor's Degree in Engineering (Geotechnology) from Suranaree University of Technology in 2009 and received her Master's Degree in Engineering (Geotechnology) from Suranaree University of Technology in 2011. For her post-graduate, she continued to study with Doctor of Philosophy Program in the Geological Engineering Program, Institute of Engineering, Suranaree university of Technology. During graduation, 2010-2014, she was a part time worker in position of research associate at the Geomechanics Research Unit, Institute of Engineering, Suranaree University of Technology.

